UNIVERSITY OF NOTTINGHAM

Non-linear electron dynamics in dilute nitride alloys

by

Spas Spasov, MSci

Thesis submitted to the University of Nottingham
for the degree of Doctor of Philosophy

in the
Faculty of Science
School of Physics and Astronomy

June 2009

Declaration of Authorship

I, SPAS SPASOV, declare that this thesis titled, "NON-LINEAR ELECTRON DYNAMICS IN DILUTE NITRIDE ALLOYS" and the work presented in it are my own. I confirm that:

- This work was done wholly or mainly while in candidature for a research degree at this University
- Where any part of this thesis has previously been submitted for a degree or any other qualification at this University or any other institution, this has been clearly stated
- Where I have consulted the published work of others, this is always clearly attributed
- Where I have quoted from the work of others, the source is always given. With the exception of such quotations, this thesis is entirely my own work
- I have acknowledged all main sources of help
- Where the thesis is based on work done by myself jointly with others, I have made clear exactly what was done by others and what I have contributed myself

Signed:

Date:

Contents

Appendices

UNIVERSITY OF NOTTINGHAM

Abstract

Faculty of Science

School of Physics and Astronomy

Doctor of Philosophy

by Spas Spasov, MSci

This thesis describes an experimental study of the electronic properties of the dilute nitride $GaAs_{1-x}N_x$ alloy. This is a semiconductor belonging to a class of highly mismatched III-N-V alloys. The incorporation of isoelectronic N on the pnictide (e.g. As) site of GaAs gives rise to a highly localised electronic state, whose energy level is resonant with the continuum of conduction band (CB) states of the host GaAs lattice. The interaction between these two sets of states causes the formation of a fully developed energy gap in the CB of the host crystal and makes possible the observation of a novel type of negative differential conductance (NDC) effect. The NDC in $GaAs_{1-x}N_x$ is qualitatively different from the NDC occurring in transferred electron devices (Gunn diodes) and semiconductor superlattices (SLs) and has potential for novel terahertz (THz) device applications.

The emphasis of the thesis is on the experimental study of the non-linear electron *dc* dynamics in $GaAs_{1-x}N_x$ that arises when electrons are accelerated in the non-parabolic CB of $GaAs_{1-x}N_x$. It also includes an investigation of the coupling of electrons to THz radiation by the measurement of harmonic generation of *ac* current and of changes in the *dc* conductivity in the presence of an applied

THz radiation. The rectification effects revealed in our experiments indicate that the mechanism giving rise to NDC is a fast (10^{-12} s) process. The fast response in time of the current is in agreement with previous calculations of the *ac* electron dynamics in $GaAs_{1-x}N_x$ predicting that the maximum response frequency associated with the NDC is governed by the time of ballistic acceleration of electrons to the N-level and that this lies in the THz frequency range.

The experimental results are discussed in terms of different theoretical models and mechanisms, including the band anticrossing model, space-charge-limited current instabilities, magnetophonon resonance and classical rectification theory.

Acknowledgements

There are many people I would like to acknowledge and thank for their help and support during my time on this project. I would like to begin by thanking my supervisors, Dr. Amalia Patanè and Prof. Laurence Eaves whose guidance, humour and frequent prodding kept me going in the right direction.

I would also like to thank Dr. Giles Allison for the time and energy he spent with me "teaching me the ropes" of cryostats, circuits, device processing and cricket rules. One big "Arigatou", my friend!

Many thanks to other members of our group, "Quantum Transport", Oleg and Lyuda, for their friendship, and my fellow PhD students Olly and Ricky who had to share an office with me and sometimes with my "dark Balkan subject" behaviour, thank you guys.

I am very grateful to Chris Pallender for providing my experiments with liquid helium, and to John Middleton, Dave Taylor and all the support staff for finely performed technical work on the equipment.

I am also indebted to our collaborators, many people at the EPSRC National Centre for III-V Technologies in Sheffield, especially to Dr. Mark Hopkinson and Dr. Robert Airey for making most of the dilute nitride samples studied in this work; Dr. Mikhail Tretyakov from the Institute of Applied Physics and Prof. Anatoliy Ignatov from the Institute for Physics of Microstructures of the Russian Academy of Sciences in Nizhny Novgorod, for their expert advices in setting up THz facilities and invaluable help in theoretical modelling and numerical analysis.

I am grateful to the Engineering and Physical Sciences Research Council for funding my research.

Lastly special thanks to my wife and my whole family. My darling Ivanka, for being the most supportive and tolerant person close to me and being the most wonderful distraction possible. Your belief in me has always been an inspiration.

List of Publications

S. Spasov, G. Allison, A. Patanè, L. Eaves, M. Yu. Tretyakov, A. Ignatov, M. Hopkinson, and G. Hill. High field electron dynamics in dilute nitride Ga(AsN). *Applied Physics Letters*, 93(2):022111, 2008.

G. Allison, S. Spasov, A. Patanè, L. Eaves, N. Kozlova, J. Freudenberger, M. Hopkinson, and G. Hill. Electron effective mass and Si-binding energy in $GaAs_{1-x}N_x$ probed by a high magnetic field. *Physical Review B*, 77(12):125210, 2008.

S. Spasov, G. Allison, A. Patanè, A. Ignatov, L. Eaves, D. K. Maude, M. Hopkinson, and R. Airey. Magnetic field tuning of hot electron resonant capture in a semiconductor device. *Applied Physics Letters*, 91(14):142104, 2007.

G. Allison, S. Spasov, A. Patanè, L. Eaves, A. Ignatov, D. K. Maude, M. Hopkinson, and R. Airey. Magnetophonon oscillations in the negative differential conductance of dilute nitride $GaAs_{1-x}N_x$ submicron diodes. *Physical Review B*, 75(11):115325, 2007.

S. Spasov, G. Allison, A. Patanè, L. Eaves, M. Hopkinson, and R. Airey. Modifying the electronic properties of GaAs/AlAs superlattices with low-density nitrogen doping. *Journal of Applied Physics*, 100(6):063718, 2006.

List of Figures

List of Tables

Abbreviations

BAC	**B**and **A**nti**c**rossing
BZ	**B**rillouin **z**one
CB	**C**onduction **B**and
IR	**I**nfra**r**ed
LCINS	**L**inear **c**ombination of **i**solated **n**itrogen resonant **s**tates
LED	**L**ight-**e**mitting **d**iode
LL	**L**andau **L**evel
LO	**L**ongitudinal **O**ptical
MBE	**M**olecular-**b**eam **E**pitaxy
MIT	**M**etal-**i**nsulator **t**ransition
MPR	**M**agneto**p**honon **r**esonace
MTS	**M**agneto-**t**unelling **s**pectroscopy
NDC	**N**egative **D**ifferential **C**onductance
NDR	**N**egative **D**ifferential **R**esistance
NDV	**N**egative **D**ifferential **V**elocity
RTD	**R**esonant **t**unelling **d**iode
SI	**S**emi-**i**nsulating
SL	**S**uper**l**attice
VB	**V**alence **B**and

Physical Constants

Quantity	Symbol	Value	Unit	Relative std. uncert. u_r
speed of light in vacuum	c	299 792 458	ms^{-1}	(exact)
permittivity of free space	ε_0	$8.854\ 187\ 817\ldots\times10^{-12}$	Fm^{-1}	(exact)
Planck constant	h	$6.626\ 068\ 76(52)\times10^{-34}$	Js	7.8×10^{-8}
$h/2\pi$	$\hbar$	$1.054\ 571\ 596(82)\times10^{-34}$	Js	7.8×10^{-8}
electronic charge	e	$1.602\ 176\ 462(63)\times10^{-19}$	C	3.9×10^{-8}
Rydberg constant	R_∞	13.605 691 72(53)	eV	3.9×10^{-8}
Bohr radius	a_0	$0.529\ 177\ 2083(19)\times10^{-10}$	m	3.7×10^{-9}
free-electron mass	m_e	$9.109\ 381\ 88(72)\times10^{-31}$	kg	7.9×10^{-8}
Boltzmann constant	k_B	$1.380\ 6503(24)\times10^{-23}$	JK^{-1}	1.7×10^{-6}

Number in brackets is the standard deviation in the last two digits of the given value [1].

Symbols

a	Bohr radius	m
a	lattice constant	m
A	amplitude of the beat note signal	dBm
A	cross sectional area	m^2
b	reciprocal lattice constant	m^{-1}
$\mathbf{B}$	magnetic induction	T
B	amplitude of the magnetic field	T
d	diameter	m
d	distance	m
d	spatial period of slow-wave structure	m
D	charge domain	
E	energy	J
$\mathbf{f}$	force	N
f	frequency	Hz
$\mathbf{F}$	electric field	Vm^{-1}
F	amplitude of the electric field	Vm^{-1}
$\mathbf{G}$	reciprocal lattice vector	m^{-1}
$\hat{\mathbf{H}}$	Hamiltonian	
I	electrical current	A
$\mathbf{j}$	current density	Am^{-2}
J	amplitude of the current density	Am^{-2}

$\mathbf{k}$	Bloch-wavevector	m^{-1}
$\mathbf{K}$	total wavevector	m^{-1}
l	hopping length	m
L	length	m
m	mass	kg
m^*	dynamical effective mass	kg
m_C^*	first derivative mass	kg
n	carrier density	m^{-3}
n	refractive index	
n_h	density of localised states	m^{-3}
$\tilde{n}$	space charge density	m^{-3}
n_s	density of injected carriers	m^{-3}
N	Landau level index	
$\mathbf{p}$	momentum	kgms^{-1}
P	power density	Wm^{-2}
$\mathbf{r}$	radius vector	m
r	average scattering rate	s^{-1}
r_i	inelastic scattering rate	s^{-1}
r_e	elastic scattering rate	s^{-1}
$\mathbf{R}$	lattice period	m
R	resistance	Ω
t	time	s
T	temperature	K
u	Bloch lattice function	
$\mathbf{v}$	velocity	ms^{-1}
V	crystal potential	eV
V	voltage	V
W	width	m
x	nitrogen content	

Γ	energy broadening of the Landau levels	eV
ε	energy	J
ε	permittivity	Fm^{-1}
ε_r	relative permittivity	
λ	wavelength	m
μ	electron mobility	$\mathrm{m}^2\mathrm{V}^{-1}\mathrm{s}^{-1}$
ρ	electrical resistivity	$\Omega\mathrm{m}$
σ	electrical conductivity	Sm^{-1}
τ	scattering time	s
ψ	Bloch wavefunction	
ω	angular frequency	s^{-1}
ω_C	cyclotron frequency	s^{-1}
ω_{LO}	longitudinal optical phonon frequency	s^{-1}
Ω	lattice volume	m^3

To Ivanka

Chapter 1

Electronic properties of GaAs and $GaAs_{1-x}N_x$

1.1 Introduction

Research into the intriguing and unique electronic properties of III-N-V semiconductor alloys, particularly of $GaAs_{1-x}N_x$ and $In_{1-y}Ga_yAs_{1-x}N_x$, has been increasing in recent years [2, 3]. The incorporation of the N-impurity into the host crystal leads to a major perturbation of the electronic band structure. The high electronegativity of N combined with its small size, stretches and compresses the neighbouring bonds, which leads to a large bandgap bowing with increasing N-content [4]. The large bowing enables the principal bandgaps of these alloys to access the near-infrared wavelength range of the electromagnetic spectrum, which is of great importance to modern fibre optic telecommunications [5], solar power conversion applications [6] and high-frequency (terahertz) electronics [7]. The mechanism by which the N-incorporation changes the bandgap of III-V compounds

is fundamentally different from that responsible for the change of the band gap in other III-V alloy systems such as $Al_xGa_{1-x}As$. This has led to the development of novel theoretical models in solid state physics. It has also created new opportunities for bandgap engineering and device structures [8], of interest to the microelectronic industry [9].

In this chapter we review the theoretical models used to describe the electronic properties in dilute nitrides and discuss the unique hot electron dynamics occurring in $GaAs_{1-x}N_x$. The chapter is organised as follows. Section 1.2 covers the band structure and electronic transport of semiconductor crystals. Section 1.3 presents a review of the crystal properties of GaAs relevant to the experiments presented in this thesis. It also describes the mechanism for negative differential conductance (NDC) in n-type GaAs (Gunn effect) that occurs under hot electron conditions. The final part of this chapter describes the electronic properties of dilute nitride $GaAs_{1-x}N_x$ and a novel mechanism of NDC in this alloy.

1.2 Band structure of semiconductors

The energy-eigenvalue problem of a semiconductor crystal yields solutions that form the band structure of the semiconductor. It is more commonly known as the energy-wavevector, or the "dispersion" curve of the material. The concept of formation and interpretation of the energy band structure is explained in great detail in Refs.[10], [11] and [12]. For a free-electron, the allowed energies take a continuous distribution from zero to infinity. The solution of the one-electron Schrödinger equation

$$\hat{\mathbf{H}}\psi(\mathbf{r}) = \varepsilon\psi(\mathbf{r}), \tag{1.1}$$

gives the relationship between the energy, ε, and wavevector, $\mathbf{k}$, where $\hat{\mathbf{H}} = -(\hbar^2/2m_e)\nabla^2$, m_e is the free-electron mass and $\hbar$ is the reduced Planck constant.

A starting point to explain the formation of energy bands in semiconductors is the nearly free-electron model, in which the positive ion cores in a semiconductor create a periodic potential, which acts to perturb the electron wavefunctions. Let us consider a periodic lattice in space of volume Ω with period $\mathbf{R}$. Bloch theorem states that the solution of Schrödinger equation (1.1) for the periodic lattice is of the type

$$\psi(\mathbf{k},\mathbf{r}) = \mathrm{e}^{i\mathbf{k}\cdot\mathbf{r}}u(\mathbf{k},\mathbf{r}), \tag{1.2}$$

where $u(\mathbf{k},\mathbf{r})$ is the Bloch lattice function, and $\psi(\mathbf{k},\mathbf{r})$ is the Bloch wavefunction. The Bloch lattice function has the same translational symmetry as the lattice.

If an electron is present in the above lattice with no potential ($V(\mathbf{r}) = 0$)[1], the Bloch wavefunctions are of the form

$$\psi(\mathbf{k},\mathbf{r}) = \frac{1}{\sqrt{\Omega}}\mathrm{e}^{i\mathbf{K}\cdot\mathbf{r}}, \tag{1.3}$$

where the total electron wavevector $\mathbf{K}$=$\mathbf{k}$+$\mathbf{G}$ can be split into a wavevector $\mathbf{k}$ in the first Brillouin zone (BZ) in the k-space representation of the crystal, and $\mathbf{G}$ is a reciprocal lattice vector, defined by $\mathbf{G}\cdot\mathbf{R} = 2\pi m$, m being an integer. Thus, the reciprocal lattice vector $\mathbf{G}$ brings the total wavevector back into the BZ. Then, we can rewrite the Bloch wavefunction as

$$\psi(\mathbf{k},\mathbf{r}) = \mathrm{e}^{i\mathbf{k}\cdot\mathbf{r}}\frac{1}{\sqrt{\Omega}}\mathrm{e}^{i\mathbf{G}\cdot\mathbf{r}}, \tag{1.4}$$

[1]The nearly free-electron model or the empty-lattice model, as distinct from the free-electron model, which has no potential and no lattice.

where the Bloch lattice function $u(\mathbf{k}, \mathbf{r})$ is clearly periodic with the lattice periodicity. Within the nearly free-electron model, knowing $\mathbf{G}$, we actually know the Bloch lattice function. When the lattice symmetry is known, the dispersion relation can then be obtained. The dispersion is nothing but the free-electron dispersion with the symmetries (translational, rotational, compound symmetries) built into it. We can now look at the "reduced zone" representation of the dispersion, since we are interested in looking at the energy as a function of the "reduced" wavevector $\mathbf{k}$, rather than the total wavevector $\mathbf{K}$. The reduced wavevector $\mathbf{k}$ is known as the Bloch-wavevector, distinct from the total wavevector $\mathbf{K}$ by a reciprocal lattice vector. The respective energies are given by

$$\varepsilon(\mathbf{k}) = \frac{\hbar^2(\mathbf{k}+\mathbf{G})^2}{2m_e}, \tag{1.5}$$

which becomes

$$\varepsilon(k) = \frac{\hbar^2\left(k+\frac{2\pi}{a}n\right)^2}{2m_e} \tag{1.6}$$

for the 1-Dimensional (1D) case with n=0, $\pm$1, $\pm$2,... and a is the lattice constant. This leads to many parabolic energy-dispersions repeated periodically along the k-axis (see Fig. 1.1(a)). The points in energy where the parabolae from different $\mathbf{G}$s intersect are the points of degeneracy. In the case of 1D lattice of spacing a, the energy degeneracies are at the zone centre ($\mathbf{k}$=0) and at the BZ edges (Fig. 1.1(a)). The reciprocal lattice vector $G = 2\pi/a$ is used to translate all wavevectors to the first BZ, thus leading to multiple energies for the same $\mathbf{k}$. The different sets of $\varepsilon(\mathbf{k})$ represent the different bands.

In the presence of the crystal potential the degeneracies can be split[2]. If all three degeneracies are split by the crystal potential, the bands are now separated

[2]The degeneracy will be split if the perturbation potential (here the crystal potential $V(\mathbf{r})$) has non-zero matrix elements with the states that are degenerate.

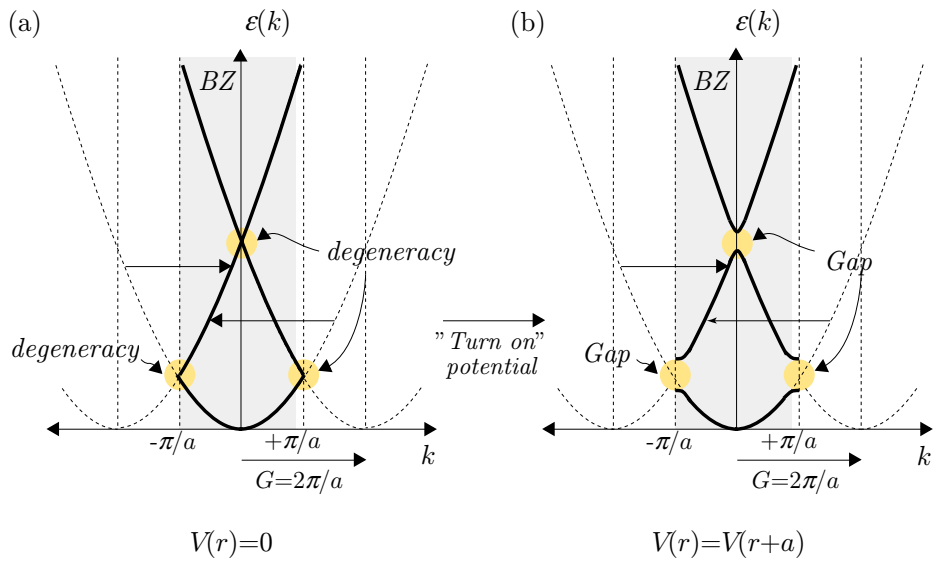

FIGURE 1.1: 1D band structure in free-electron (a) and in nearly free-electron (b) model. The dashed lines represent different parabolic dispersions corresponding to different Gs. The shadowed vertical stripes represent the first Brillouin zone. The points of energy degeneracy in part (a), highlighted by yellow circles evolve into energy gaps in part (b).

by energy gaps (see Fig. 1.1(b)). The magnitudes of the gaps are determined by the magnitude of the crystal potential[3]. Thus, the periodic crystal potential splits the allowed energies into bands, separated by forbidden gaps. The number of states (in $-\pi/a \leq k \leq +\pi/a$) in each band in the first BZ is equal to the number of atoms in the whole crystal. Most physical phenomena (electronic, optical, magnetic) in semiconductors can be understood by looking at a small portion of the bandstructure. These points are the lowest points in the CB and the highest points in the valence band (VB). In GaAs, these points occur at the same **k**-vector, **k**=0, also called **Γ**-point.

[3]Gap magnitudes are determined by the Fourier components of the crystal potential at the particular reciprocal lattice vector determining the particular band.

1.2.1 Effective mass approximation

The energy-wavevector curves in a crystal periodic potential deviate from the free-electron parabola close to the zone boundaries (see Fig. 1.1). This is an immediate result of the interaction between the electrons and the atoms in the crystal and can be understood in terms of the scattering of electron wavefunctions.

When the Bragg condition,

$$2\mathbf{k} \cdot \mathbf{G} = G^2 \tag{1.7}$$

(G being the reciprocal lattice vector), for the wavevector of electrons scattered from atoms in the crystal, is satisfied, the electron waves are coherently reflected at the zone boundaries. The interference of these Bragg reflected waves leads to standing waves, with group velocity,

$$v(k) = \frac{1}{\hbar}\frac{\partial \varepsilon(k)}{\partial k}, \tag{1.8}$$

equal to zero. This condition explains the flattening of the $\varepsilon(k)$ dispersion at the zone boundaries (at $k = n\pi/a$, n being an integer), see Fig. 1.1(b).

The concept of electron effective mass states that when an electron with mass m_e moves inside a crystal, it responds to an external force as if its mass were m^*. The expression for m^* can be derived from differentiating with respect to time Eq.1.8,

$$\dot{\mathbf{v}} = \hbar^{-1}\frac{\partial^2 \varepsilon}{\partial k^2}\dot{\mathbf{k}} \tag{1.9}$$

and using the fact that when the electron in the crystal is subject to an external force $\mathbf{f}$ its motion satisfies

$$\hbar\dot{\mathbf{k}} = \mathbf{f}. \tag{1.10}$$

Combining Eqs.1.9 and 1.10 we obtain

$$\mathbf{f} = \frac{\hbar^2}{\partial^2\varepsilon/\partial k^2}\dot{\mathbf{v}}. \tag{1.11}$$

If we now identify $\hbar^2/(\partial^2\varepsilon/\partial k^2)$ as a mass, then Eq.1.11 takes the form of the Newton's second law. The effective mass m^* is now defined as

$$\frac{1}{m^*} = \frac{1}{\hbar^2}\frac{\partial^2\varepsilon}{\partial k^2}. \tag{1.12}$$

The mass defined by Eq.1.12 is known as the dynamical effective mass and is usually quoted numerically as a ratio of the free-electron mass, m_e.

In many semiconductors for which the energy-wavevector relation is parabolic at small k, the electron effective mass can be determined by cyclotron resonance experiments. In this case the mass is derived from the cyclotron frequency, ω_C, when electrons are accelerated in helical orbits about the axis of a static magnetic field, B. The electron mass in this case, known as a first derivative mass, is defined as

$$\frac{1}{m_C^*} = \frac{1}{\hbar^2 k}\frac{\partial\varepsilon}{\partial k} = \frac{\omega_C}{eB}, \tag{1.13}$$

where e is the electronic charge. For parabolic energy dispersions $m^* = m_C^*$.

1.2.2 Semiclassical model of electronic transport in semiconductors

The momentum of a free-electron is related to the wavevector by $\mathbf{p} = \hbar\mathbf{k}$. In the presence of an electric field, $\mathbf{F}$, and magnetic field, $\mathbf{B}$, the force, $\mathbf{f}$, acting on an electron of charge $-e$ is given by Newton's second law of motion

$$\mathbf{f} = \hbar\dot{\mathbf{k}} = -e(\mathbf{F} + \mathbf{v} \times \mathbf{B}). \tag{1.14}$$

In the absence of collisions and integrating Eq.1.14 with $\mathbf{B}$=0, the equation of motion predicts that a *dc* electric field will cause a constant acceleration of the electrons, resulting in a steadily increasing electric current. But in practice this does not happen as the electrons suffer collisions with thermal vibrations (phonons), lattice imperfections and impurity atoms. This effect can be taken into account by modifying the equation of motion in the form

$$\hbar(\dot{\mathbf{k}} + \mathbf{k}/\tau) = -e(\mathbf{F} + \mathbf{v} \times \mathbf{B}). \tag{1.15}$$

Here we introduce the effect of collisions causing $\mathbf{k}$ to decay exponentially to zero with time constant τ, when the applied field is switched off. The physical interpretation of τ is that of a mean time between collisions, in which an electron loses its momentum.

In the presence of a constant electric field only, the steady state solution of Eq.1.15 is

$$\mathbf{k} = -\frac{e\tau}{\hbar}\mathbf{F}. \tag{1.16}$$

If the number of electrons per unit volume is n, the current density is given by

$$\mathbf{j} = -ne\mathbf{v} = \sigma\mathbf{F} = \frac{1}{\rho}\mathbf{F}, \tag{1.17}$$

which is Ohm's law with electrical conductivity, σ, and electrical resistivity, ρ.

1.3 Band structure properties of GaAs

Like most III-V compounds, GaAs crystalises in a zinc-blende structure. The primitive cell consists of two atoms, Ga and As, repeating in space in such a way that each species forms a face-centred cubic (fcc) sub-lattice. The two sub-lattices of Ga and As, each with lattice constant a, are mutually penetrating and shifted relative to each other by a quarter of the body diagonal. The lattice constant is $a = 5.65325$ Å at $T = 300$ K and its temperature dependence is given by $a = 5.65325 + 3.88 \times 10^{-5}(T - 300)$ Å, where T is the temperature in Kelvin [13]. The reciprocal lattice is body-centred cubic (bcc) with a conventional unit cell of size $b = 4\pi/a$. As the inset in Fig. 1.2 shows, the first BZ is a truncated octahedron. The calculated band structure of GaAs is shown in Fig. 1.2. It can be seen that the lowest point of the CB occurs at the point $\mathbf{\Gamma}$ for which $k = 0$. Therefore, for n-type doped GaAs, the conduction electrons lie in the $\mathbf{\Gamma}$-valley. The dispersion relation, $E(k)$, can be approximated by an isotropic parabola for states within a few meV above the CB minimum, i.e.:

$$E(k) \approx E(0) + \frac{\hbar^2 k^2}{2m^*}, \tag{1.18}$$

where the effective mass $m^* = 0.067m_e$ is taken at the $\mathbf{\Gamma}$-point and at low temperature (T=4.2 K). At higher energies, the effective mass depends on the magnitude

and direction of k. The band gap, E_G, between the bottom of the CB and the top of the VB varies from 1.42 eV at room temperature to 1.52 eV at T=4.2 K and its temperature dependence is given by $E_G(T) = E_G(0) - \alpha T^2/(T+\beta)$, where $E_G(0)$=1.519 eV, $\alpha = 5.405 \times 10^{-4}$ eV/K, and β=204 K [14].

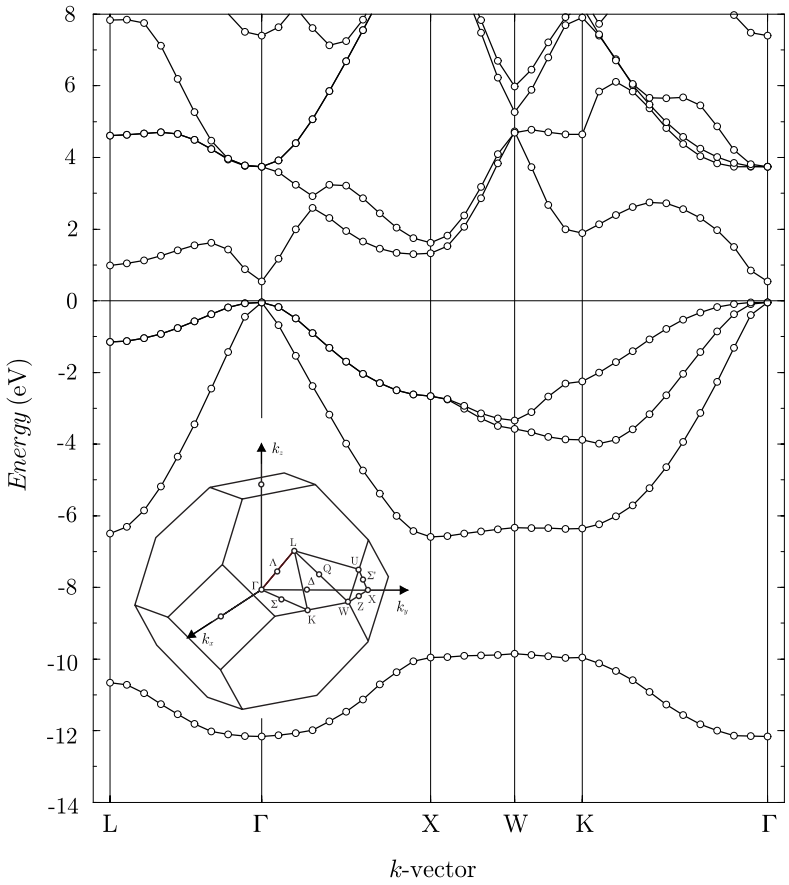

FIGURE 1.2: Calculated bulk band structure of GaAs. Inset: BZ for bcc reciprocal lattice. The labels indicate the high-symmetry points. The top of the VB is at E=0 and k=0. Picture reproduced from Ref. [15].

An interesting feature of the band structure of GaAs is the presence and position of the satellite **X**- and **L**-valleys. They lie about 480 and 290 meV above the bottom of the **Γ**-valley, respectively. Under high applied electric fields the electrons in **Γ**-valley can be elastically scattered into adjacent valleys, where they

become less mobile, thus producing a negative differential velocity (NDV) effect, commonly referred to as the Gunn effect [16, 17]. The following section gives an overview of this hot electron effect.

1.4 Transferred electron (Gunn) diode

In the early 1960s B. K. Ridley and T. B. Watkins [18] and C. Hilsum [19] showed theoretically that the highly mobile electrons in the **Γ**-CB minimum in GaAs could transfer to higher energy CB minima (at the **X**- and/or **L**-points) where they would be less mobile (Fig. 1.3). This would then lead to a negative differential mobility and a negative differential bulk conductivity. Soon after their theoretical predictions, this idea was experimentally proved.

In 1963 J. B. Gunn [16, 17] discovered a negative differential velocity (NDV) effect. This occurs when a high voltage, such that the electric field exceeds a critical field $F_C \sim 10^3$ Vcm^{-1}, is applied to a thin n-type GaAs sample (thickness of the order of 10 μm). The NDV is accompanied by negative differential conduction (NDC) and oscillations of the current at microwave frequencies. The frequency of oscillation is inversely proportional to the length of the sample across which the field is applied. From the experiment, the frequency of oscillation turns out to be equal to the saturation velocity, v_s, divided by the sample length. For sample lengths of the order of 10 μm and $v_s = 10^5$ ms^{-1}, the oscillation frequency is of the order of 10 GHz. Hence the obvious application of the Gunn effect is the fabrication of microwave generators known as Gunn diodes. The Gunn effect is one example of how NDV can lead to high-frequency oscillations.

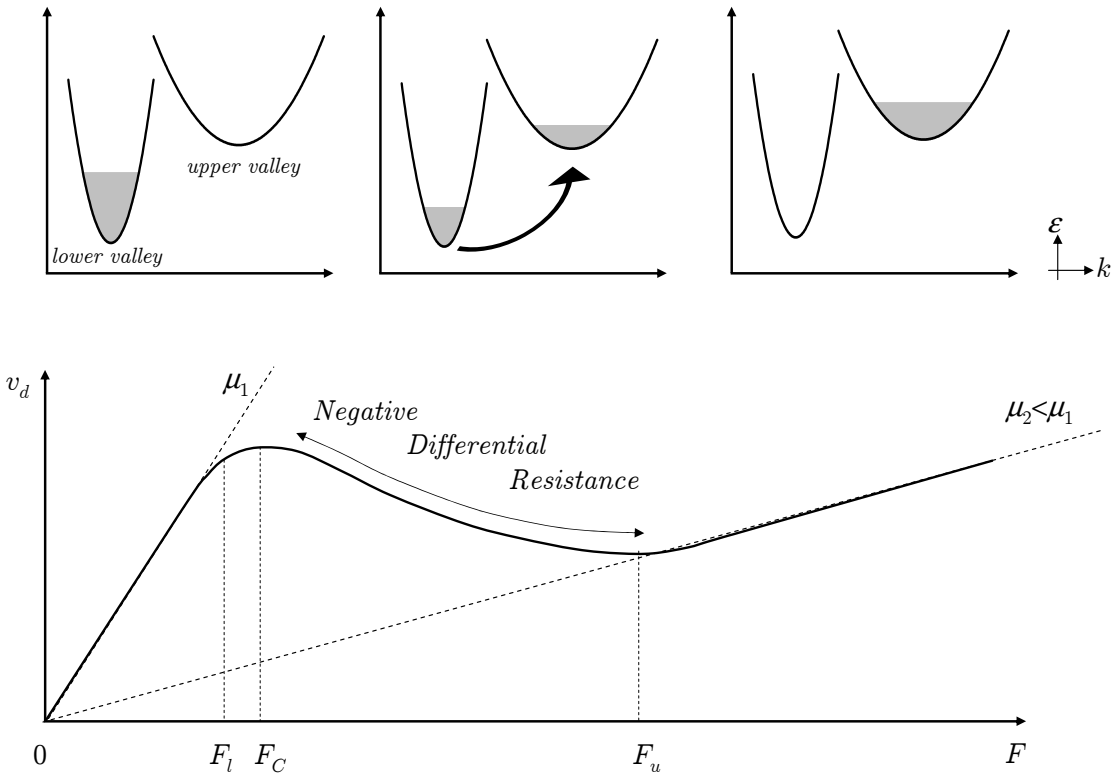

FIGURE 1.3: Mechanism for Gunn effect in GaAs. Top: intervalley electron transfer from lower ($\mathbf{\Gamma}$) valley to upper ($\mathbf{X}$ and/or $\mathbf{L}$) valley. Grey areas represent occupied electron states. Bottom: Sketch of the dependence of the drift velocity, v_d, in GaAs on electric field, F. At low field, F_l, highly mobile (μ_1) $\mathbf{\Gamma}$-CB electrons contribute to the ohmic resistance. As the field is increased to a critical value, F_C, electrons elastically scattered into the upper CB valley become less mobile ($\mu_2 < \mu_1$) and produce a region of negative differential resistance. As the field is increased even further, above F_u, more electrons are in the upper band due to the larger density of states.

This effect can be qualitatively understood by assuming that the field dependence of the drift velocity, v_d, in n-GaAs has the simple form shown schematically in Fig. 1.4(a). Let us suppose that a constant high voltage is applied across the sample so that carriers drift from left to right (see Fig. 1.4(b)). We also assume that the electric field is slightly below the threshold field, F_C, for NDV. Due to fluctuations in the electric field at finite temperatures, a small region labeled D in Fig. 1.4(b) acquires a field slightly above F_C at time t=0. Now the carriers on both sides of D have higher drift velocities than those inside D. This results in carriers

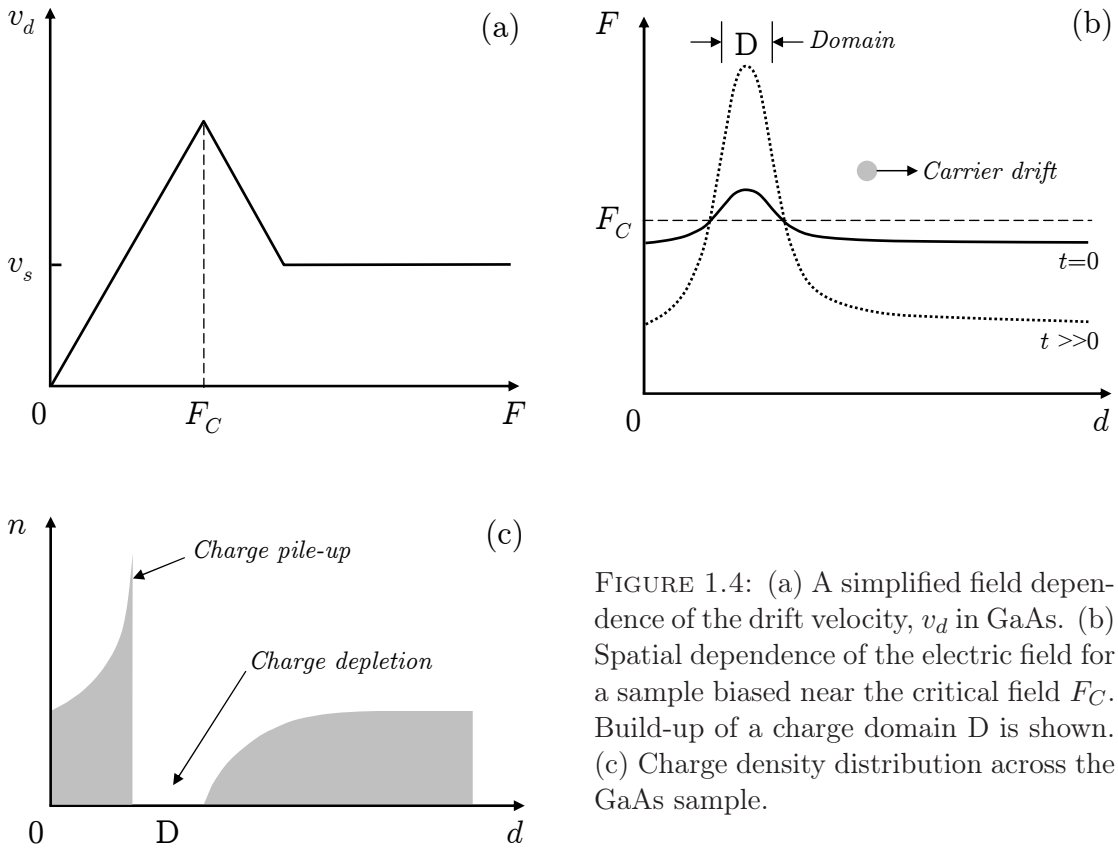

FIGURE 1.4: (a) A simplified field dependence of the drift velocity, v_d in GaAs. (b) Spatial dependence of the electric field for a sample biased near the critical field F_C. Build-up of a charge domain D is shown. (c) Charge density distribution across the GaAs sample.

piling-up on the left hand side in D while the carrier density on the right side will drop (Fig. 1.4(c)). The charge pile-up in D at time $t > 0$ leads to an increase in electric field inside D and decreasing field outside. Because of the NDV, for fields larger than F_C, the increase in the field inside D leads to further slowing down of electrons inside D and hence more charge pile-up. Once started, this process will continue until most of the applied field is across D at $t \gg 0$. The region D where the electric field is high is known as a domain. The domains are usually formed near the cathode, since the field fluctuations are largest there. Under the influence of the applied voltage, this domain drifts across the sample with speed equal to the saturation velocity until it reaches the anode, thus giving rise to a periodic oscillation of the current. This oscillatory current results in emission of high-frequency electromagnetic waves.

The Gunn diode is one example of how the particular band structure of GaAs can produce a bulk NDC effect. In the following section we describe the electronic band structure of dilute nitride $GaAs_{1-x}N_x$ and show that its unusual CB can also lead to a bulk NDC effect, which is fundamentally different from the Gunn effect.

1.5 Dilute nitride $GaAs_{1-x}N_x$

In dilute nitride $GaAs_{1-x}N_x$ alloy, the perturbation of the host GaAs lattice by N is so large that results in a fundamentally new type of band structure. This arises from the amalgamation of extended Bloch and highly localised N-related states. To understand the properties of dilute nitrides, a detailed description of the band structure is required. However, methods used to describe conventional alloys, such as the virtual crystal approximation, are unable to describe this material system. An alternative empirical two-level band anticrossing (BAC) model [20, 21] and microscopic models [22, 23, 24, 25] have been developed in recent years and provide a useful tool to understand the electronic properties of this new class of materials.

In this thesis it is shown that, despite its relative simplicity, the BAC model is able to successfully describe the electron dynamics occurring in bulk $GaAs_{1-x}N_x$ at low x ($\lesssim$0.1%). In this dilute regime the two-level BAC model describes well the band structure of $GaAs_{1-x}N_x$ and predicts a splitting of the CB into two highly non-parabolic hybridised subbands. Our studies show that this non-parabolicity can be exploited to achieve a new type of negative differential velocity (NDV) effect when electrons are accelerated by an electric field in the CB of $GaAs_{1-x}N_x$. This effect is not observed at high N-content.

As the N-content increases, N-aggregates, such as impurity N-N pairs and higher order clusters form. These have strongly localised energy levels, which break up the CB [22, 26]. At these high levels of N doping ($> 0.1\%$), the disorder in the system profoundly modifies the electronic properties of the alloy. To describe the CB of $GaAs_{1-x}N_x$ in this regime, the BAC model is extended in the form of the linear combination of isolated nitrogen resonant states (LCINS) model [26]. This includes the interaction between the GaAs host $\mathbf{\Gamma}$-states and the full range of N-related levels present in the alloy.

This section reviews these two models and describes the unique electronic band structure of $GaAs_{1-x}N_x$ and the origin of NDC observed in this material system.

1.5.1 Electronic properties

A remarkable effect of N-incorporation in GaAs is the significant decrease of the direct energy gap, E_G, between the VB and CB (see Fig. 1.5), accompanied by a considerable variation in the electron effective mass m^* [20, 27]. At low nitrogen content ($\lesssim 0.1\%$) a band anticrossing (BAC) model [20] is typically used to describe the unusual band structure of dilute nitride alloys. Figure 1.5 illustrates how successful is this model in describing data for the energy gap of $GaAs_{1-x}N_x$ from different experimental groups. The admixing and hybridisation of the extended GaAs CB states with the localised single N-impurity levels splits the CB into two subbands E_- and E_+ [28]. According to a two-level BAC model [20] the dispersion relations of the two subbands are calculated as roots of the characteristic

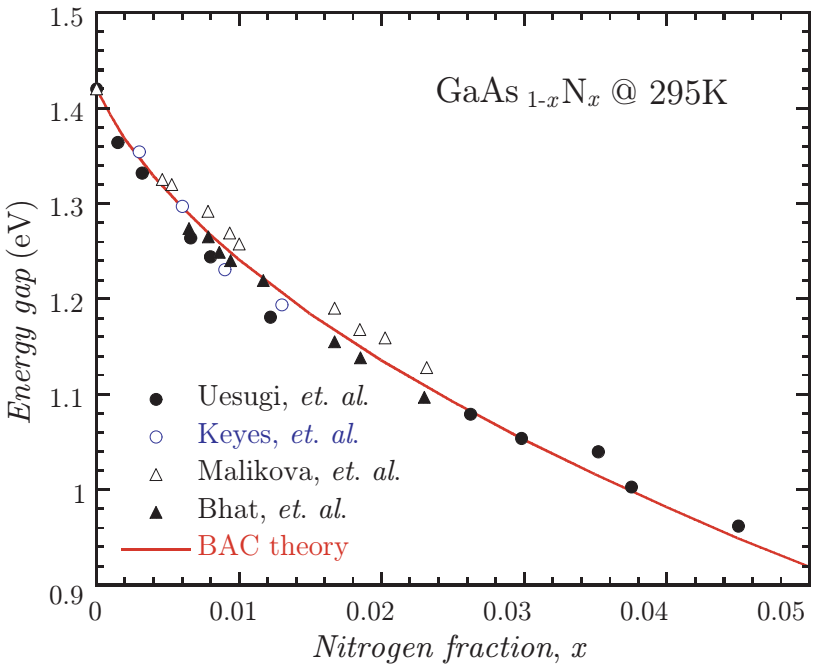

FIGURE 1.5: Energy gap, E_G, of $GaAs_{1-x}N_x$ as a function of nitrogen content, x, from various reports. The solid curve is the result of fitting using the BAC model. Picture reproduced from Ref. [4].

polynomial of the matrix

$$\hat{\mathbf{A}} = \begin{pmatrix} E_N & V_{MN} \\ V_{MN} & E_M(k) \end{pmatrix}. \tag{1.19}$$

Here $E_M(k)$ is the energy dispersion of pure GaAs, E_N is the energy of the single N-impurity level (E_N 1.65 eV above the GaAs VB edge at T=4.2 K) and $V_{MN} = C_{MN}\sqrt{x}$ (C_{MN}=2.7 eV [29]) is the N-content dependent matrix element describing the strength of the interaction between the two sets of states. By solving the secular equation

$$\det(\hat{\mathbf{A}} - E\hat{\mathbf{I}}) = 0, \tag{1.20}$$

where E is the energy dispersion of $GaAs_{1-x}N_x$ and $\hat{\mathbf{I}}$ is the identity matrix, we derive the dispersion relation for subbands E_- and E_+, i.e.:

$$E_{\pm}(k) = \frac{1}{2}\left\{[E_M(k) + E_N] \pm \sqrt{[E_M(k) - E_N]^2 + 4V_{MN}^2}\right\}. \tag{1.21}$$

Figure 1.6 shows the CB of $GaAs_{1-x}N_x$ calculated using the BAC model with a nitrogen concentration of 0.1% and $T = 4.2$ K. In addition to the reduction of the CB minimum of $GaAs_{1-x}N_x$ with respect to that of GaAs, this model predicts the splitting of the CB into two subbands E_- and E_+ separated by a well defined energy gap.

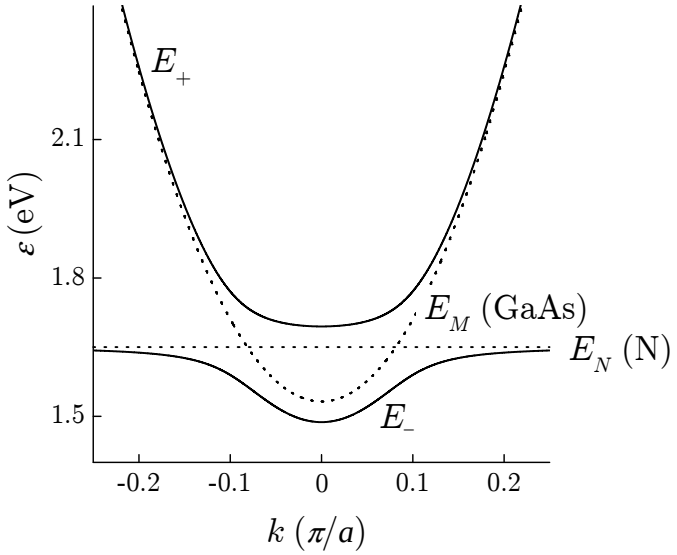

FIGURE 1.6: Energy-wavevector relation for subbands E_- and E_+ of $GaAs_{1-x}N_x$ calculated according to a two-level BAC model for N-content of 0.1% and $T = 4.2$ K. The normalised horizontal axes shows k as a fraction of the size of the first Brillouin zone of GaAs (a is the lattice constant of GaAs).

To probe the energy dispersion of $GaAs_{1-x}N_x$ and the validity of BAC model, the magneto-tunelling spectroscopy (MTS) technique [30] was used with resonant tunelling diodes (RTDs) containing a $GaAs_{1-x}N_x$ layer in the intrinsic region [31]. In addition to the splitting of the CB and reduction of the CB minimum, these

measurements also revealed the fragmentation of the band and a strong impurity-like character of the states in the proximity of the N-level. Figure 1.7 shows the energy dispersion of $GaAs_{1-x}N_x$ with a nitrogen content of 0.1% as derived using the MTS technique. The lighter areas correspond to the stronger band-like character of the state. Thus, the states in the region of N-level are localised in nature, whereas those with energies well above and below N-level possess **Γ**-like character.

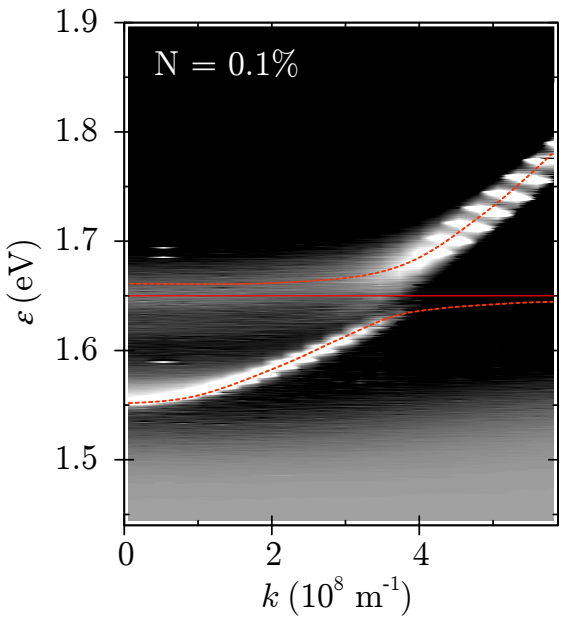

FIGURE 1.7: Energy-wavevector relation in $GaAs_{1-x}N_x$ extracted from MTS measurements in RTDs with $GaAs_{1-x}N_x$, reproduced from Ref. [31]. The solid and dashed red lines are guides to the eye showing the position of N-level and the E_- and E_+ subbands, respectively.

Despite of its simplicity, the BAC model is able to describe successfully a range of dilute nitride materials and fundamental properties such as the band gap variation with N-content, pressure and temperature [32, 33, 34]. However, at high N-concentrations, it fails in describing the N-content dependence of the conduction band edge (CBE) electron effective mass [27]. The BAC model predicts a monotonic enhancement of the CBE mass with increasing N. It provides a good

estimate of the measured mass at very low N-compositions ($x < 0.05\%$), but significantly underestimates the mass in $GaAs_{1-x}N_x$ for $x > 0.1$ %, and fails to describe its non-monotonic dependence on N-content (see Fig. 1.8).

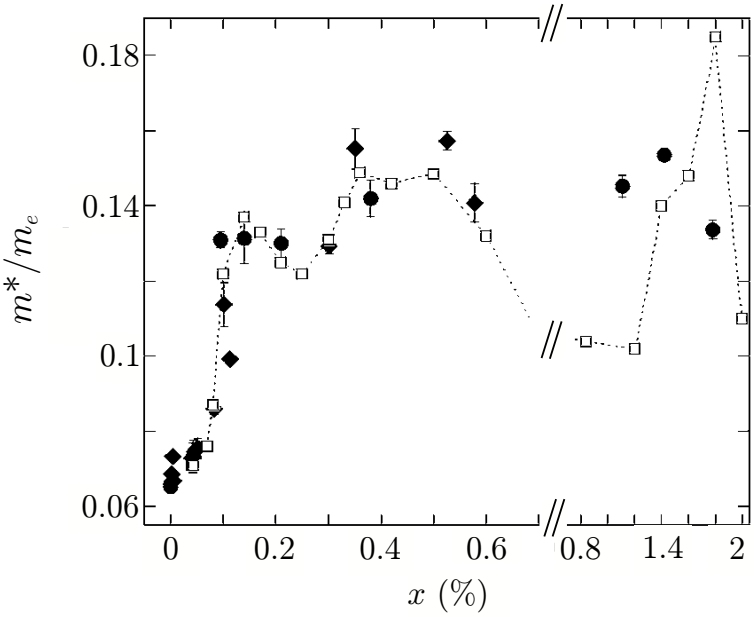

FIGURE 1.8: Measured values of the electron effective mass as a function of the N-concentration, x. Several untreated (full circles) and H-irradiated (full diamonds) samples are considered. Error bars indicate the uncertainty on the mass values (in some case the uncertainty is within the symbol size). Open squares are the calculated effective mass values, the dotted line is a guide to the eye. An abscissa axis break at $x = 0.7$ % is introduced for ease of comparison. Picture reproduced from Ref. [27].

The weak point in the BAC model is that it does not explicitly consider the admixing of the **L**-, **X**- and **Γ**-valleys caused by N-incorporation; nor does it account for the formation of other N-related defects such as N-N pairs and higher order clusters, whose energy levels lie above and below the CB minimum. These states can act not only as efficient radiative recombination centres for excitons [35] but also as free-carrier traps, thus profoundly affecting fundamental electronic properties of the material, such as electron mobility and carrier concentration. There are different approaches developed to describe the formation and effect of

N-related defects and also to explain the duality, **Γ**-like and impurity-like, of the N-induced states.

In the empirical pseudopotential model by Kent and Zunger, it is shown that nearest-neighbour N-clusters produce bound states inside the band gap [22]. These are also observed by photoluminescence measurements [36, 37, 38]. In particular, a family of [1,1,0] N-chains produces bound states that become increasingly deep as each additional N-atom is added to the chain. In contrast, the non-nearest-neighbour N-pairs usually give resonant states above the CB minimum (see Fig. 1.9). In addition to the calculated energy levels of the isolated N-atom and 1^{st} to 6^{th} order N-N pairs, Kent and Zunger give the fraction of **Γ**, **L** and **X** character for each state.

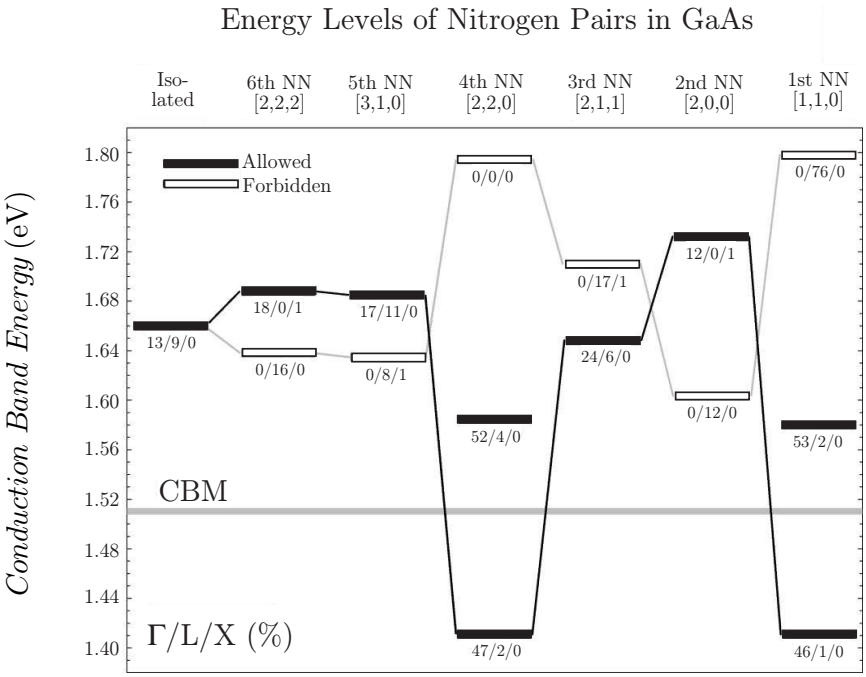

FIGURE 1.9: The energy levels of isolated N-atom and N-N pairs in GaAs. The legend indicates the orientation (e.g. [1,1,0]) of the pairs. The allowed (solid bar) or forbidden (hollow bar) nature of transitions to the valence band is indicated and the **Γ**, **L** and **X** character of each state is shown. Picture reproduced from Ref. [22].

Although the pseudopotential model developed by Kent and Zunger provides a good understanding of the unique type of alloy disorder induced by N and of the nature (localised or delocalised) of the N-related states, this model does not explicitly describe the $\varepsilon(k)$ relation. The sharp N-related resonances of bound states within the band continua break up the Bloch symmetry in the crystal making impossible defining an energy-wevevector relation [39]. However, the definition of $\varepsilon(k)$ is an essential element for describing the electrical and optical properties of devices based on dilute nitrides.

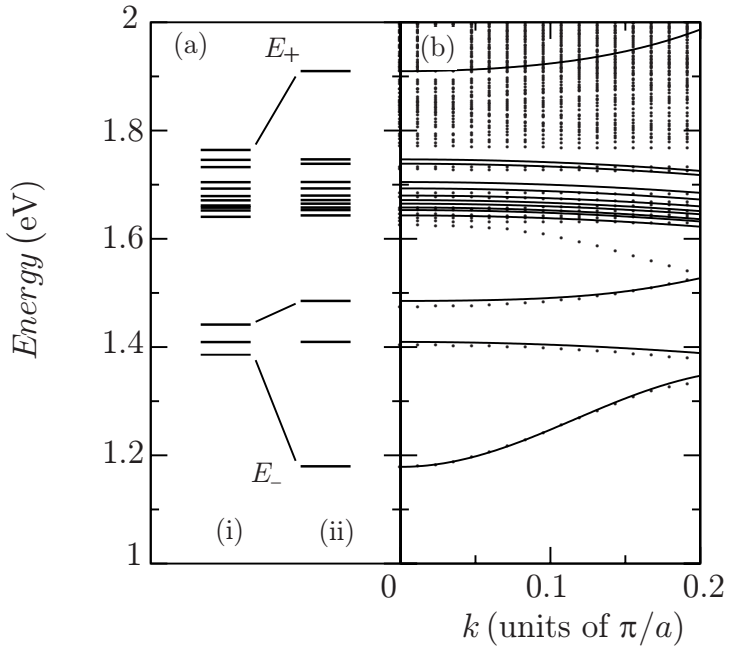

FIGURE 1.10: (a) Calculated N-cluster-state energies and the CBE energy (thin line) in a $Ga_{500}As_{478}N_{13}$ supercell (i) before and (ii) after inclusion of interaction with CBE. (b) Supercell band dispersion obtained by tight-binding (dots) and LCINS (solid lines) methods. Picture reproduced from Ref. [26].

In the linear combination of isolated nitrogen resonant states (LCINS) model [26], Lindsay and O'Reilly propose an alternative approach to the description of $GaAs_{1-x}N_x$. They extend the BAC model to include the interaction between the GaAs $\mathbf{\Gamma}$-states and the full range of N-related levels present in the alloy. This

model describes the energy levels of isolated N-impurities, N-N pairs and N-clusters and the strength of their interaction with the host **Γ**-states. It gives a detailed picture of how the electronic properties of $GaAs_{1-x}N_x$ are affected at different N-concentrations and present a useful description of the CB minimum. Figure 1.10(a) shows the calculated N-cluster energy states and the CBE energy before and after inclusion of interaction of the N-related states with the Bloch states of GaAs. Also, Fig. 1.10(b) shows that the energy dispersions obtained by the LCINS model are in good agreement with those obtained by a tight-binding method.

The N-concentrations considered in this thesis are relatively low ($< 0.4\%$). This allows us to use a simple two-level BAC model in our analysis of the electron dynamics. The BAC model gives a convenient definition of the energy-wavevector dispersion, which is of particular importance when transport properties and hot electron phenomena are investigated.

1.5.2 Hot electron dynamics and negative differential conductance

The BAC model predicts highly non-parabolic $\varepsilon(k)$ dispersions for the E_- and E_+ subbands, see Fig. 1.11(a). Of particular interest is the presence of an energy gap between E_- and E_+ and the unusual form of the lower energy subband E_-. This electronic band structure affects the electron dynamics. The k-dependence of the group velocity $v_g{=}\hbar^{-1}(\partial\varepsilon/\partial k)$ is shown in Fig. 1.11(b). At a k-value, k_i, corresponding to the inflection point in the E_- subband, ε_{th}, there is a peak in the group velocity. The second derivative electron effective mass is positive and increases with k for $\varepsilon < \varepsilon_{th}$. However, at the inflection point it changes its sign resulting in negative effective mass (Fig. 1.11(c)).

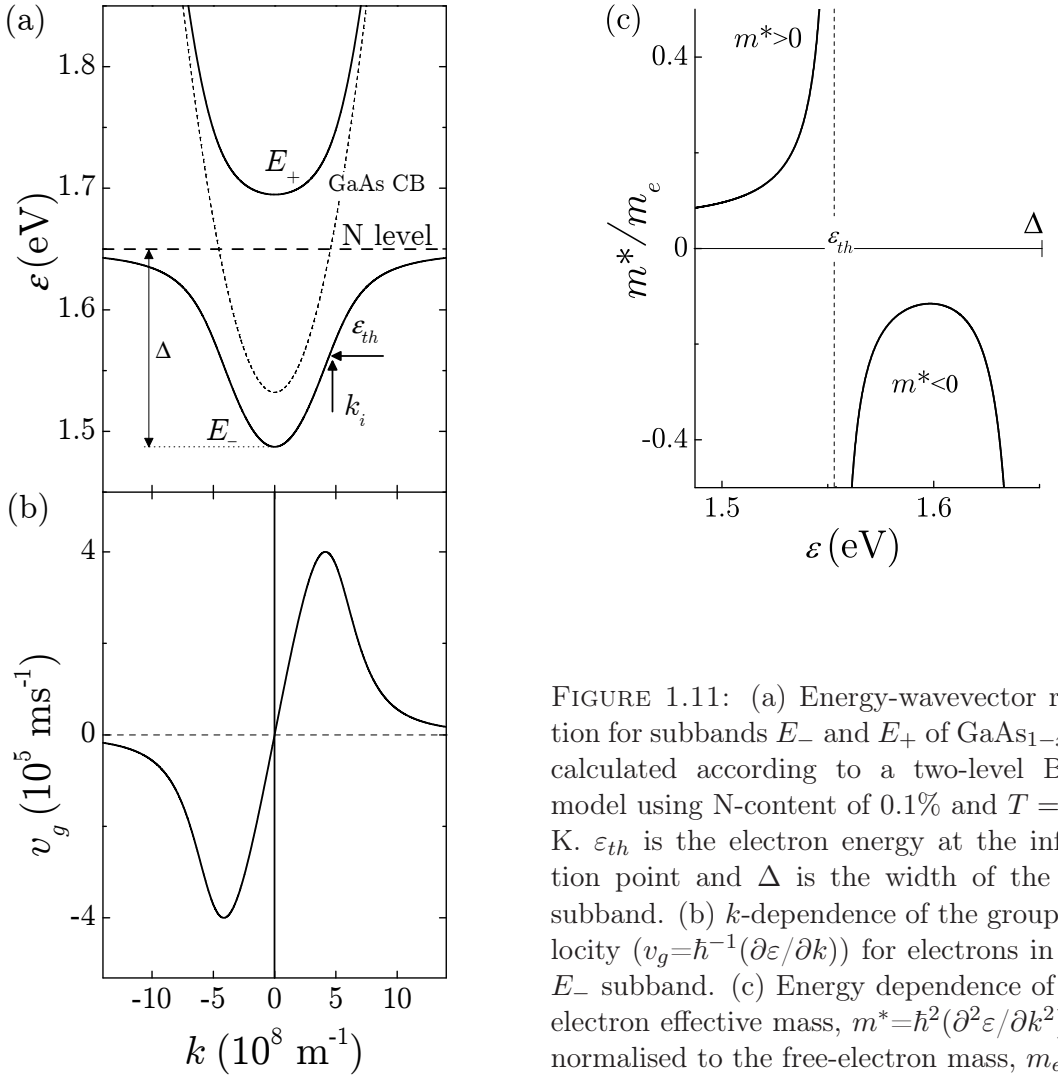

FIGURE 1.11: (a) Energy-wavevector relation for subbands E_- and E_+ of $GaAs_{1-x}N_x$ calculated according to a two-level BAC model using N-content of 0.1% and $T = 4.2$ K. ε_{th} is the electron energy at the inflection point and Δ is the width of the E_- subband. (b) k-dependence of the group velocity (v_g=$\hbar^{-1}(\partial\varepsilon/\partial k)$) for electrons in the E_- subband. (c) Energy dependence of the electron effective mass, m^*=$\hbar^2(\partial^2\varepsilon/\partial k^2)^{-1}$, normalised to the free-electron mass, m_e.

Under an applied electric field, F, electrons can gain sufficient energy to approach the energy of the N-level, thus causing a strong NDC effect [40]. The motion of the conduction electrons in $GaAs_{1-x}N_x$ can be described by a semiclassical model [11, 40, 41]. The time evolution of the average electron energy, $\overline{\varepsilon}$, and electron drift velocity, v_d, is derived from the dynamical balance equations:

$$\frac{dv_d}{dt} = \frac{qF}{m^*(\overline{\varepsilon})} - r_v v_d \tag{1.22}$$

$$\frac{d\overline{\varepsilon}}{dt} = qFv_d - r_i\overline{\varepsilon}, \tag{1.23}$$

where $q(=\text{-}e)$ is the electronic charge, $r_v = r_i + r_e$ is the relaxation rate of the velocity, which includes the energy relaxation rate, r_i, and the elastic scattering rate, r_e. The energy-dependent electron effective mass, $m^*(\overline{\varepsilon})$, is derived from the form of the $E_-(k)$ dispersion given by the BAC model [20]. The steady state solution of Eqs.1.22 and 1.23 leads to

$$v_d = r_i\overline{\varepsilon}/qF \tag{1.24}$$

and

$$\overline{\varepsilon} = (qF)^2/m^*(\overline{\varepsilon})r_v r_i, \tag{1.25}$$

from which the $v_d(F)$ dependence can be numerically obtained.

As shown in Fig. 1.11(c), the average electron energy $\overline{\varepsilon}$ is always smaller than ε_{th}. For $\overline{\varepsilon} < \varepsilon_{th}$ the effective mass can be approximated by

$$m^*(\varepsilon) = m^*(0)/(1 - \overline{\varepsilon}/\varepsilon_{th}), \tag{1.26}$$

which leads to the analytical form of $v_d(F)$,

$$v_d(F) = \frac{\mu F}{1 + (F/F_C)^2}. \tag{1.27}$$

Here $\mu = em^*(0)^{-1}r_v^{-1}$ is the low-field mobility, and

$$F_C = p_N(r_v r_i)^{1/2}(1+D)^{1/4}/2e, \tag{1.28}$$

is the critical field for NDV corresponding to a peak in the drift velocity

$$v_d^M = p_N(r_i/r_v)^{1/2}(1+\sqrt{1+D})/8m(1+D)^{1/4}. \tag{1.29}$$

Here p_N=$\sqrt{2m\Delta_N}$, where Δ_N is the energy position of the N-level relative to the conduction band minimum of GaAs (Δ_N=0.13 eV), m is the electron effective mass of GaAs at k=0, D=$4V_{MN}^2/\Delta_N^2$ and $V_{MN} = C_{MN}\sqrt{x}$ (C_{MN}=2.7 eV) is the coupling matrix element between the N-level and the conduction band states of GaAs within the BAC model.

In contrast to the NDC observed in Gunn diodes, which involves intervalley transfer of electrons, the NDC in $GaAs_{1-x}N_x$ has a different physical origin. It is a result of the formation of a fully developed energy gap in the CB of the host GaAs crystal and involves electrons being accelerated in the highly non-parabolic E_- subband of $GaAs_{1-x}N_x$.

Chapter 2

Samples and experimental setup

This chapter describes the samples, experimental techniques and test equipment used to obtain the results presented in this thesis. It starts with a description of the sample design and the device processing; it continues with a discussion of electrical measurements at different temperatures and in the presence of an applied *dc* and/or *ac* electromagnetic field. Finally, along with the magneto-cryostat facilities and related equipment, a detailed description is given to facilities for experiments with high-frequency (terahertz) electromagnetic radiation. During my PhD course I have contributed to the installation and development of these facilities.

2.1 Sample growth and processing

We used three different series of samples based on $GaAs_{1-x}N_x$, all grown by molecular-beam epitaxy (MBE). For the magneto-transport *dc* studies and for high-frequency *ac* measurements, we studied a series of "vertical" diodes based on

GaAs/GaAs$_{1-x}$N$_x$/GaAs heterostructures. For electron mobility and carrier concentration measurements by the Hall effect, we used modulation-doped GaAs$_{1-x}$N$_x$ quantum well heterostructures and n-doped GaAs$_{1-x}$N$_x$ epilayers. The following sections give details of each type of structure.

2.1.1 Vertical GaAs/GaAs$_{1-x}$N$_x$/GaAs diodes

The first series of samples (Series A) consists of an n^+-n-n^+ silicon (Si)-doped GaAs/GaAs$_{1-x}$N$_x$/GaAs heterostructure, grown on an n^+ (100)-oriented GaAs substrate (Fig. 2.1). The layer structure is as follows: 0.2-μm-thick n^+ GaAs layer, an n-type GaAs$_{1-x}$N$_x$ layer (x=0.1%) of thickness L and a 0.5-μm-thick n^+ GaAs cap layer. The length L and the Si doping of the GaAs$_{1-x}$N$_x$ layer are summarised in Table 2.1.

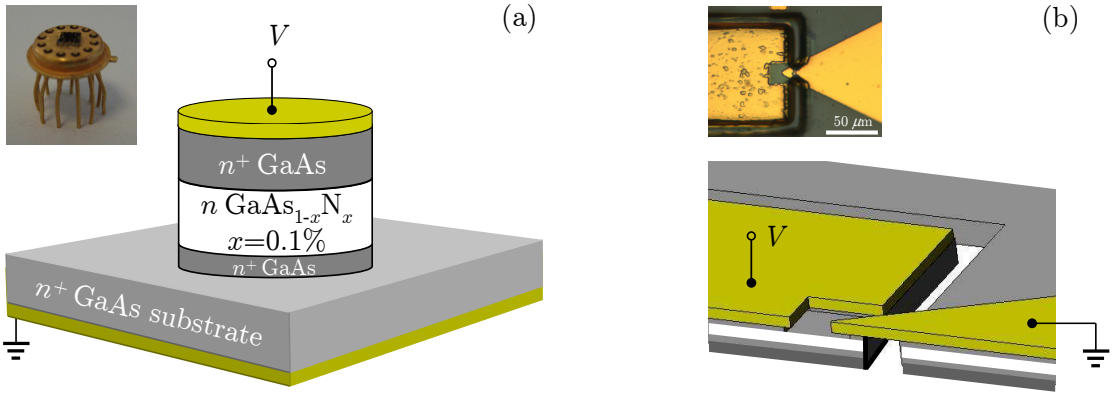

FIGURE 2.1: Schematic of the vertical devices. Two types of devices are shown - vertical (a) and thin planar diodes (b). The insets show photographs of the devices.

All devices were fabricated from semiconductor wafers grown at the EPSRC National Centre for III-V Technologies in Sheffield. Two types of processing were used. For electrical measurements, the samples were processed into circular mesas

TABLE 2.1: Details of samples A

Sample Number	L (μm)	Si doping (m^{-3})
VN456	0.6	1×10^{23}
VN680	1	1×10^{24}
VN681	1	1×10^{23}
VN682	0.1	1×10^{24}
VN683	0.1	1×10^{23}

of diameter 5-100 μm with top and bottom electrical contacts (see Fig. 2.1(a)). In this work, we define the positive bias as applied to the top contact. To make ohmic contacts on both the substrate and surface sides, an InGe/Au alloy was deposited in a thermal evaporator and annealed at 420 °C. For high-frequency detection experiments, we fabricated thin planar diodes (Fig. 2.1(b)). While the electrical mesa device fabrication is a rather conventional process, the fabrication of thin planar diodes for high-frequency operation requires a different approach [42, 43]. These devices were fabricated by Yuriy Blyashko at the Institute of Electronic Measurements "Kvarz" in Nizhny Novgorod, Russia under the Royal Society (UK) International Joint Project between The University of Nottingham and The Institute of Applied Physics of the Russian Academy of Sciences in Nizhny Novgorod.

2.1.2 *n*-doped $GaAs_{1-x}N_x$ epilayers

The second series of samples (Series B) is based on n-doped $GaAs_{1-x}N_x$ epilayers. These samples consist of a thick (1 μm) Si-doped (Si: 1×10^{23} m^{-3}) $GaAs_{1-x}N_x$ epilayer grown on a semi-insulating (SI) GaAs substrate with a thin (50 nm) buffer GaAs layer between them (see Fig. 2.2(a)). The N-content in $GaAs_{1-x}N_x$ epilayer varies from 0 to 1%. Table 2.2 summarises the properties of these layers. The

samples were processed into Hall bars (Fig. 2.2(b)) and into small planar diodes (Fig. 2.2(c)) using a standard wet etch technique. As shown in Fig. 2.2(c), in the planar diodes the $GaAs_{1-x}N_x$ channel between the two electrodes has length, L, and width, W, both less than 100 μm.

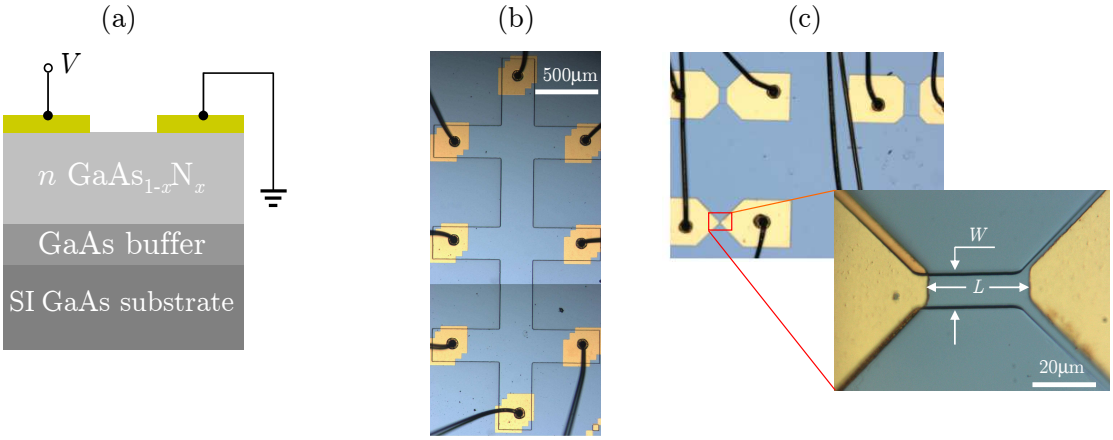

FIGURE 2.2: (a) Sketch of the growth sequence of $GaAs_{1-x}N_x$ epilayers. The $GaAs_{1-x}N_x$ epilayer has a Si-concentration of 1×10^{23} m^{-3} and N-content x=0, 0.1, 0.2, 0.4 and 1 %. Photograph of the chip surface showing processing into Hall bars (b) and into rectangular mesas (c) with length, L, and width, W.

TABLE 2.2: Details of samples B

Sample Number	x (%)	Si doping (m^{-3})
VN459	0.1	1×10^{23}
VN460	0.2	1×10^{23}
VN461	0.4	1×10^{23}
VN462	1	1×10^{23}
VN463	0	1×10^{23}

To investigate how the electron mobility is affected by the N-content in other III-N-V compounds, a set of $InP_{1-x}N_x$ and $InAs_{1-x}N_x$ epilayers was also grown. The $InP_{1-x}N_x$ samples consist of a thick (1 μm) Si-doped (Si=1×10^{23} m^{-3}) $InP_{1-x}N_x$ epilayer grown on a SI Fe-doped InP substrate and a 50-nm-thick

undoped InP buffer layer in between, see Table 2.3. The samples were processed into Hall bars to carry out Hall mobility measurements. All the $GaAs_{1-x}N_x$ and $InP_{1-x}N_x$ epilayers were fabricated from semiconductor wafers grown at the EPSRC National Centre for III-V Technologies in Sheffield.

TABLE 2.3: Details of the $InP_{1-x}N_x$ epilayers

Sample Number	x (%)	Si doping (m^{-3})
VN1222	0.1	1×10^{23}
VN1223	0	1×10^{23}

The $InAs_{1-x}N_x$ samples consist of an $InAs_{1-x}N_x$ epilayer grown on a SI GaAs substrate. Table 2.4 summarises the growth details of these samples. The samples were processed into Hall bars. All devices were fabricated at the Mid-Infrared Optoelectronics Research Group at Lancaster University.

TABLE 2.4: Details of the $InAs_{1-x}N_x$ epilayers

Sample Number	$InAs_{1-x}N_x$ layer thickness (μm)	x (%)
A0276	1.5	0
A0285	0.9	0.4
A0282	0.8	0.6

2.1.3 Modulation-doped $GaAs_{1-x}N_x$ heterostructures

The third series of samples (Series C) consists of a set of modulation-doped samples based on $GaAs_{1-x}N_x$ quantum wells. These samples were grown on a SI (100)-oriented GaAs substrate with N-content of 0, 0.1 and 0.4 %. Table 2.5 describes the layer structure of these samples.

TABLE 2.5: Details of samples C

Layer material	Thickness (Å)	Si doping (m^{-3})	N-content, x (%)		
			VN475	VN476	VN477
GaAs	100	undoped			
$Al_{0.33}Ga_{0.67}As$	300	2×10^{24}			
$Al_{0.33}Ga_{0.67}As$	50	undoped			
GaAs	10	undoped			
$GaAs_{1-x}N_x$	100	undoped	0.1	0.4	0
GaAs	10	undoped			
$Al_{0.33}Ga_{0.67}As$	500	undoped			
GaAs	20000	undoped			

In the modulation-doped heterostructures, the Si dopant is physically separated from the active $GaAs_{1-x}N_x$ layer, thus allowing high values of electron mobility to be achieved. To carry out transport measurements, the modulation-doped samples were processed into Hall bars using a standard wet etch technique. All devices were fabricated from semiconductor wafers grown at the EPSRC National Centre for III-V Technologies in Sheffield.

2.1.4 GaAs/AlAs superlattices

For the comparison studies of the THz response in different systems with NDC (see Chapter 6), we used a series of devices based on GaAs/AlAs superlattice (SL). They were grown by MBE on (100)-oriented Si-doped n-type (10^{24} m^{-3}) GaAs substrate. The samples contain 15 SL periods, which are separated from two heavily n-doped GaAs contacts by Si-doped $Al_{0.03}Ga_{0.97}As$ layers of width 30 nm and doping concentration of 2×10^{22} m^{-3}. A SL unit cell is formed by 2.5 nm of $Al_{0.3}Ga_{0.7}As$ and 10 nm of GaAs doped with Si at 1.8×10^{22} m^{-3}. The samples were processed into circular mesa devices of diameter 10 μm, with Ohmic contacts to the substrate and top capping layer.

2.2 Electrical measurements

Figure 2.3 shows 4-terminal circuit diagram for the current-voltage $I(V)$ measurements. The device was mounted on a sample probe and connected to a voltage source by coaxial cables. The voltage drop on the sample was measured by a voltmeter. The whole measuring process was controlled by a PC with a software program written in *LabVIEW*.

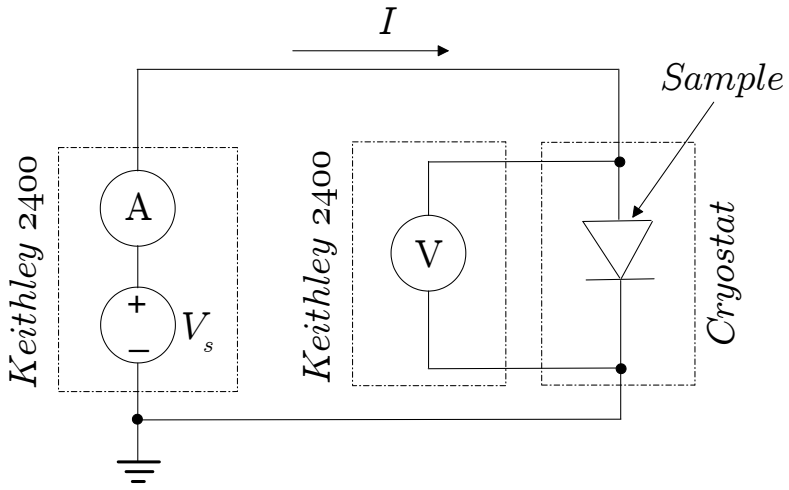

FIGURE 2.3: Standard 4-terminal circuit for measuring $I(V)$ characteristics.

2.3 High-frequency facilities and experiments

When a sample with non-linear $I(V)$ characteristic is subject to an high-frequency electromagnetic field, a variety of *ac* phenomena can be observed. These include photo-induced change in *dc* conductivity and harmonic generation of *ac* current. To analyse these effects, different types of high-frequency experiments were carried out. The setup consists of Backward Wave Oscillators (BWOs) as sources of THz radiation, a detector of high-frequency signals (Ge bolometer) and additional

electronics specially designed to work at THz frequencies. To analyse sub-THz current signals, a frequency down conversion (heterodyning) technique [44] was used.

2.3.1 Heterodyning and harmonic generation of an *ac* signal

In telecommunications, physics, and radio astronomy, heterodyning is a process of generation of new frequencies by mixing two or more signals in a non-linear device such as a vacuum tube, transistor, diode mixer, Josephson junction or bolometer. The mixing of two frequencies, f_1 and f_2, results in the generation of new frequencies, $f_{\pm}{=}nf_1{\pm}mf_2$ (n, m-number of harmonic). The lower frequency, f_-, is sometimes referred to as a beat note or intermediate frequency [45, 46]. The beat note signal can be much lower than the frequencies mixed and could be easily analysed by means of conventional radioelectronics.

Two generators of high-frequency signals (Hewlett Packard model number, HP83711B) covering the frequency range 1 to 20 GHz with resolution of 1 kHz and a Maximum Leveled Output Power of +11 dBm with ±1.0 dB accuracy, were used as highly stable narrow spectrum signal sources in the heterodyne measurement setup. Additional electronic devices such as a Spectrum analyser, High-frequency amplifiers, $I(V)$ curve tracer, lock-in amplifiers, diplexers and filters were also used in the experiments.

Figure 2.4 sketches the experimental setup for measuring harmonic generation of *ac* current when using a $GaAs_{1-x}N_x$ diode as a mixer of high-frequency signals.

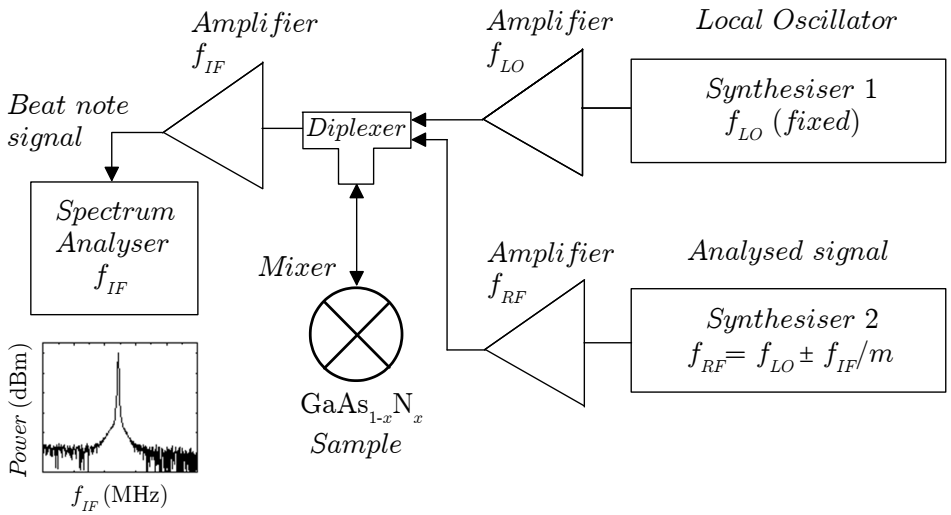

FIGURE 2.4: Schematic of the heterodyne method in which a $GaAs_{1-x}N_x$ diode is used as a mixer of high-frequency signals.

2.3.2 High-frequency detection experiments

For the high-frequency detection experiments, we used three BWOs operating at different frequencies in the range of 0.1 to 0.7 THz and powers in the range 1 to 50 mW.

A BWO is a tunable source of coherent sub-mm radiation. This microwave device is based on the interaction of an electron beam and an electromagnetic field and exploits the so-called Cherenkov effect [47, 48]. Cherenkov radiation occurs when electrons move in a medium with a refractive index $n>1$, and the electron velocity, v, is greater than the phase velocity of the electromagnetic waves, $v_{ph}=c/n$, where c is the speed of light in vacuum. This radiation process can occur only when the refractive index is large enough, i.e. $n>c/v$.

Slow waves, i.e., waves with $v_{ph}<c$, may also exist in periodic structures, where, in accordance with the Floquet theorem, an electromagnetic wave can be represented as the superposition of spatial harmonics $E=\mathrm{e}^{-i\omega t}\sum_{l=-\infty}^{+\infty}A_l\mathrm{e}^{ik_{zl}z}$

with axial wave numbers k_{zl}=k_{z0}+$2\pi l/d$. Here ω is the angular frequency of the radiation, d is the spatial period, l is the harmonic number, k_{z0} is the wave number of the zeroth-order spatial harmonic (-π/d<k_{z0}<π/d), and the coefficients A_l are determined by the shape of the structure. Electromagnetic radiation from electrons in a periodic slow-wave structure is known as Smith-Purcell radiation and it can be considered as a type of Cherenkov radiation.

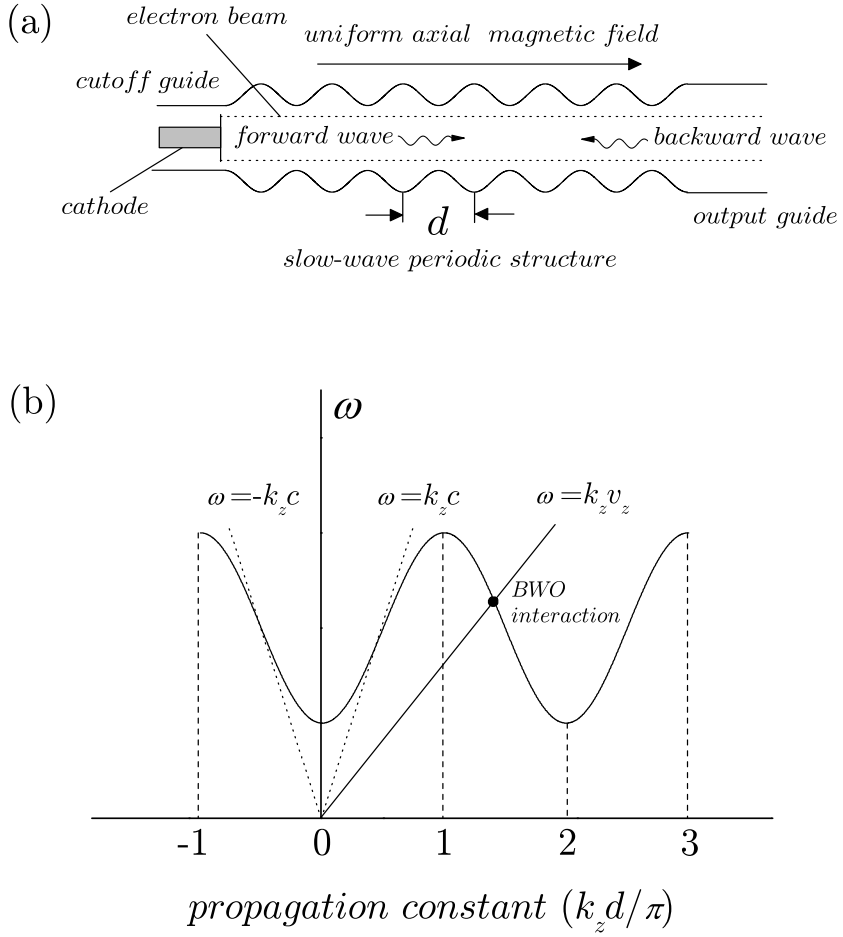

FIGURE 2.5: (a) Schematic of a BWO. (b) Dispersion curve for slow-wave structure [49].

The principle of operation of the BWO is illustrated in Fig. 2.5. The schematic of the device (Fig. 2.5(a)) shows the electron beam, guided by an external magnetic field, passing through a periodic rippled-wall structure. Figure 2.5(b)

represents the corresponding dispersion diagrams, i.e., the dependence of the wave frequency on its axial wave number, in a slow-wave structure with period d. The dashed line, $\omega{=}k_z c$, represents the boundary between regions of fast ($v_{ph}{=}\omega/k_z{>}c$) and slow ($v_{ph}{<}c$) waves. The passband is the frequency band ranging from the lower frequency (the cutoff frequency at points $k_z{=}0,\ 2\pi/d,...$) and the upper frequency (at the points $k_z{=}\pi/d,\ 3\pi/d,...$).

The operating frequency of the BWO is determined by the intersection of the dispersion curve with the beam line $\omega{=}k_z v_z$ (see Fig. 2.5(b)), corresponding to the Cherenkov synchronism condition, $v_{ph}{=}v_z$. The BWO operates in regions where the group velocity, $d\omega/dk$, is negative ($\pi/d{<}k_z{<}2\pi/d$, etc.) and amplifies backward waves which propagate in the opposite direction as the electron beam, thus providing an internal feedback mechanism.

An essential characteristic of the BWO as a microwave source is its electrical tunability over a wide frequency range. By changing the operating voltage (electron velocity) and/or the periodic length d, one can move the point of intersection of the electron dispersion with the dispersion of the electromagnetic field (Fig. 2.5), thus providing a means of frequency tuning.

The schematic of the high-frequency detection experiment with BWOs is shown in Fig. 2.6. The measurements were performed in an Oxford Instruments continuous gas flow optical cryostat. To cool the system, helium (He) gas is drawn from a Dewar vessel of liquid He through a transfer tube by a pump. A heater and a rhodium-iron (RhFe) thermistor, mounted inside the cryostat on the path of the He gas, are used to control the temperature with an Oxford Instruments temperature controller. This enables the temperature to be varied between 4-300 K with a 50 mK accuracy. The optical access to the sample is provided by a quartz window, sealed with indium (In) to maintain the vacuum shield insulation between

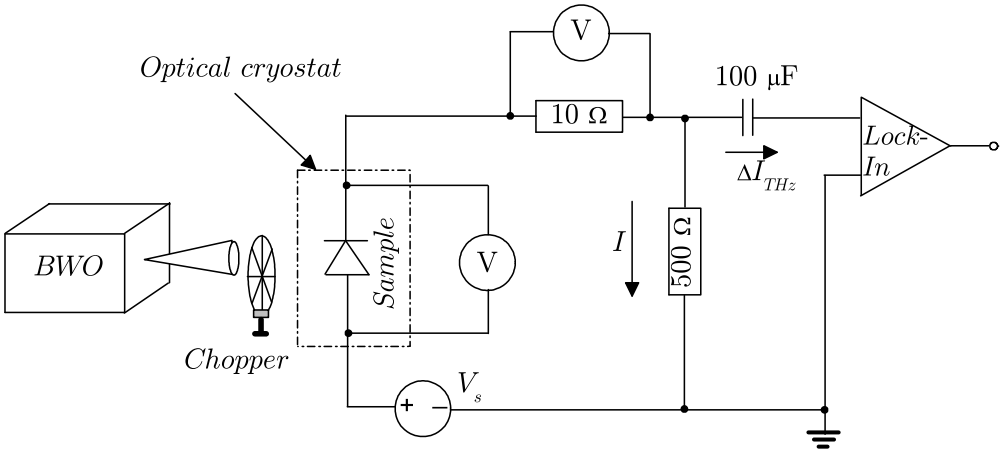

FIGURE 2.6: Schematic of the measuring setup used to detect the "photocurrent" induced by excitation of the sample with THz radiation from a BWO source.

the sample space and outer casing. The sample was mounted on a sample probe with electrical plug to connect to auxiliary test equipment. When the sample, kept at low temperature in the optical cryostat, is excited with sub-THz electromagnetic waves from the BWO, a *dc* current is induced in the circuit. To extract and record the "photo"-induced component of the current, ΔI_{THz}, a standard lock-in technique with chopping frequency of the order of 100 Hz and *dc* decoupling capacitor were used.

2.4 Low-temperature magneto-transport measurements

The low-temperature transport measurements in high magnetic field were performed in magneto-cryostats. A ^{4}He Cryogenic Ltd cryostat with a superconducting magnet (Fig. 2.7), capable of providing a field up to 14 T and a stable temperature from 2 to 300 K, was used. The system uses a superconducting

high-field solenoid immersed in a bath of liquid He. A continuous He-flow variable temperature insert allows stable temperatures to be achieved in the 2-300 K range.

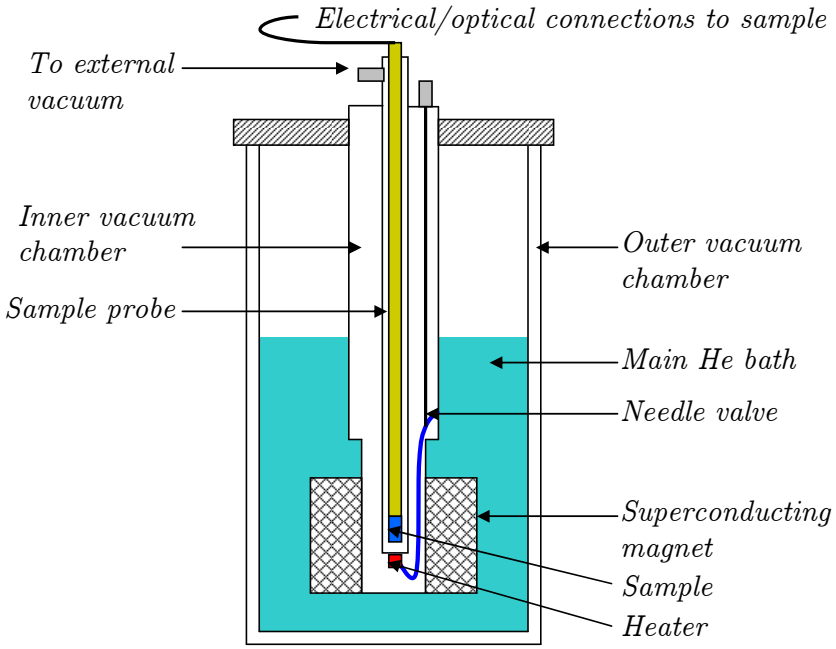

FIGURE 2.7: Sketch of Cryogenic magneto-cryostat.

Similar to the optical cryostat described in the previous section, an external vacuum pump is used to draw liquid He from the main bath into the sample space via a needle valve and a heat exchanger. The actual temperature is controlled using a RhFe thermometer mounted in the sample space and a resistive heater, adjacent to the sample space, providing electronic feedback. The sample was inserted into the bore of the cryostat on a specially designed sample probe, allowing accurate positioning of the sample within the volume of an homogenous magnetic field and also providing rotational freedom for different sample orientations in relation to the magnetic field axis.

In order to obtain higher magnetic fields up to 23 T, we used a water cooled resistive magnet at the Grenoble High Magnetic Field Laboratory (France). For even higher magnetic fields up to 50 T, we carried out experiments using a non-destructive pulsed ($\sim$ 40 ms) magnet at the Leibniz Institute for Solid State and Materials Research Dresden (Germany).

Chapter 3

Hall mobility in III-N-V compounds

In this chapter we examine the electron mobility in dilute nitride alloys. Transport measurements on a series of devices based on $GaAs_{1-x}N_x$, $InP_{1-x}N_x$ and $InAs_{1-x}N_x$ Hall bars, reveal a strong dependence of the Hall mobility and free-electron density on N-content. The observed strong reduction of these parameters at high N-concentrations ($x > 0.2\%$) suggests trapping of electrons onto defect states, whilst in the ultra-dilute regime ($x \sim 0.1\%$) the electronic transport is mainly via extended states. Sections 3.1 and 3.2 review the basic theory of magneto-transport in semiconductors and describe the origin of classical Hall effect. In the last section we present our experimental results of Hall mobility measurements on $GaAs_{1-x}N_x$, $InP_{1-x}N_x$ and $InAs_{1-x}N_x$ based Hall bars.

3.1 Magnetoconductivity tensor

The simple representation of electrical conductivity (1.17) as a constant of proportionality between the current density, $\mathbf{j}$, and the electric field, $\mathbf{F}$, is a special case

of a more general description of the second-rank conductivity tensor $\hat{\boldsymbol{\sigma}}$ defined as

$$\mathbf{j} = \hat{\boldsymbol{\sigma}} \cdot \mathbf{F}. \tag{3.1}$$

For the case of an isotropic CB, $\hat{\boldsymbol{\sigma}}$ is a diagonal tensor with all diagonal elements given by

$$\sigma = en\mu = ne^2\tau/m^*, \tag{3.2}$$

where n is the electron density, $\mu = e\tau/m^*$ is the electron mobility, τ is the scattering time and m^* is the effective mass of the electron. However, if the magnetic field is present, the conductivity tensor contains off-diagonal elements that are linearly dependent on the magnetic field and can be used to study an important phenomenon known as the Hall effect.

We consider an infinite, cubic and nonmagnetic crystal with a magnetic field, $\mathbf{B}$, applied along the z axis and an electric field, $\mathbf{F}$, applied in the xy plane. Within the quasi-classical approach, the equation of motion for the electrons is given by Eq.1.15. Under steady-state conditions $\dot{\mathbf{k}} = 0$ and Eq.1.15 can be written as

$$\frac{m^*}{\tau}\mathbf{v}_d = -e(\mathbf{F} + \mathbf{v}_d \times \mathbf{B}), \tag{3.3}$$

where $\mathbf{v}_d$ is the electron drift velocity. By using the Eqs.1.13 and 1.16 we can write the components of the current density as

$$j_x = \frac{1}{1 + (\omega_C\tau)^2}\sigma(F_x - \omega_C\tau F_y), \tag{3.4}$$

$$j_y = \frac{1}{1 + (\omega_C\tau)^2}\sigma(F_y + \omega_C\tau F_x), \tag{3.5}$$

$$j_z = \sigma F_x, \tag{3.6}$$

and the magnetoconductivity tensor $\hat{\boldsymbol{\sigma}}(B)$ as

$$\hat{\boldsymbol{\sigma}} = \frac{\sigma}{1+(\omega_C\tau)^2}\begin{pmatrix} 1 & -\omega_C\tau & 0 \\ \omega_C\tau & 1 & 0 \\ 0 & 0 & 1+(\omega_C\tau)^2 \end{pmatrix}$$

$$= \frac{en\mu}{1+(\mu B)^2}\begin{pmatrix} 1 & -\mu B & 0 \\ \mu B & 1 & 0 \\ 0 & 0 & 1+(\mu B)^2 \end{pmatrix}. \tag{3.7}$$

Eq.3.7 reveals that the effect of the magnetic field on the charge transport is twofold. First, the transverse conductivity, σ_{xx}, is decreased by a factor $[1 + (\mu B)^2]$. The corresponding increase in the resistance induced by a magnetic field, known as magnetoresistance, is proportional to B^2 for small values of B. Second, the magnetic field induces a current perpendicular to the applied electric field, resulting in non-zero off-diagonal elements in the conductivity tensor. These are linearly proportional to the magnetic field and give rise to the Hall effect, which is a useful phenomenon to investigate fundamental transport properties, including electron mobility and carrier concentration [10, 50].

3.2 Hall effect

Figure 3.1 demonstrates the geometry of a typical Hall effect. A magnetic field directed along the z-axis causes the electrons to drift in the y direction due to the action of the Lorentz force. As a result, electrons tend to pile up on one side of the sample and create a transverse electric field F_y, which cancels the effect of the

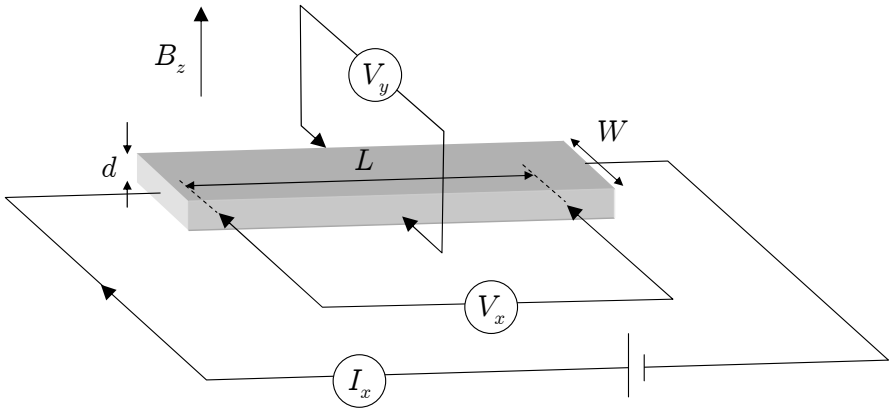

FIGURE 3.1: Geometry for Hall effect measurement in 3-Dimensional electron sysytem.

Lorentz force. By introducing electrical resistivity as

$$\hat{\boldsymbol{\rho}} = \hat{\boldsymbol{\sigma}}^{-1} \tag{3.8}$$

and using Eq. 3.7, for the geometry shown in Fig. 3.1, we note that

$$\rho_{xx} = \frac{\sigma_{xx}}{\sigma_{xx}^2 + \sigma_{xy}^2} = \frac{1}{\sigma} \tag{3.9}$$

is independent of B. In a typical Hall effect experiment (Fig. 3.1), ρ_{xx} is determined as

$$\rho_{xx} = \frac{V_x}{I_x}. \tag{3.10}$$

Under steady-state condition $j_y = 0$ and Eqs.3.4 and 3.5 take the form

$$j_x = \sigma F_x \tag{3.11}$$

and

$$F_y = -\mu B_z F_x. \tag{3.12}$$

The measured quantity in this experiment is F_y while j_x and B_z are externally controlled parameters. The Hall coefficient is defined as

$$R_H = \frac{F_y}{j_x B_z}, \tag{3.13}$$

and combining Eqs.3.11 and 3.12, it is possible to determine the electron density and the electron mobility using

$$R_H = -\frac{1}{ne} \tag{3.14}$$

and

$$\mu = |R_H|\sigma. \tag{3.15}$$

3.3 Hall mobility in dilute nitrides

To assess the feasibility of using III-N-V compounds in electronic devices, we investigated the electronic transport properties of a series of heterostructure devices based on $GaAs_{1-x}N_x$, $InP_{1-x}N_x$ and $InAs_{1-x}N_x$. Transport measurements on Hall bars revealed a strong dependence of the electron mobility on N-concentration. As the mobility is a parameter that depends on elastic and inelastic scattering processes, these measurements provide a means of assessing the disorder induced by N into the host crystal.

Figure 3.2(a) shows the dependence of the measured Hall mobility and carrier concentration on x in n-doped $GaAs_{1-x}N_x$ epilayers (samples B). In the ultra-dilute regime ($x \sim 0.1$ %) the free-carriers concentration is almost independent of x and is close to the nominal value of $1{\times}10^{23}$ m^{-3}. However, for $x > 0.2\%$, the free-electron concentration rapidly drops to a value of $n \sim 4{\times}10^{21}$ m^{-3} which is

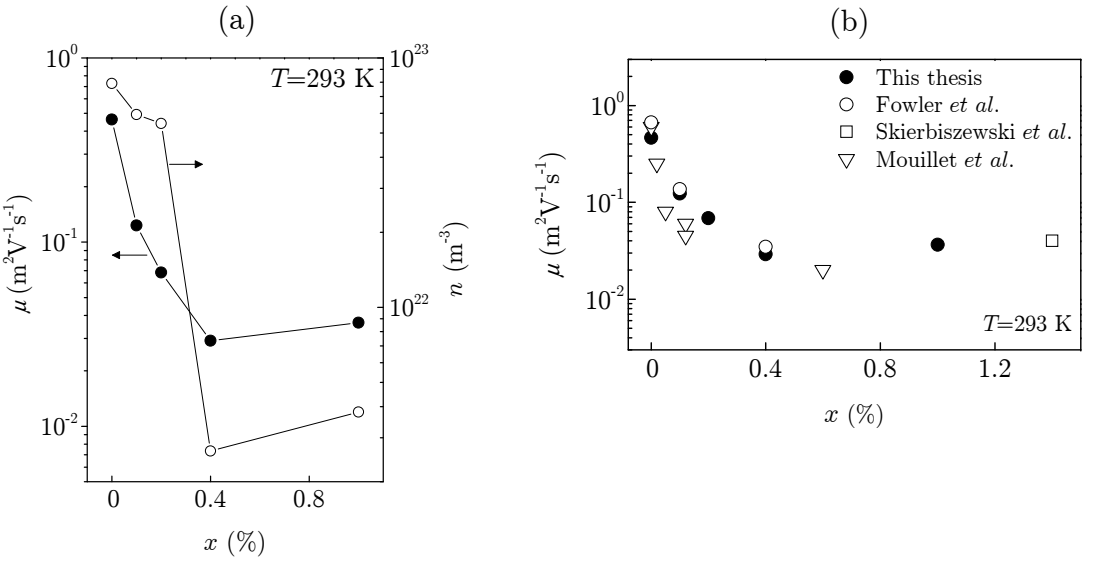

FIGURE 3.2: (a) x-dependence of the measured Hall mobility (left scale) and carrier concentration (right scale) for n-doped $GaAs_{1-x}N_x$ epilayers at T=293 K (samples B). The solid lines are guides to the eye. (b) x-dependence of Hall mobility. Full dot symbols refer to n-doped $GaAs_{1-x}N_x$ epilayers from this work. Circles, squares and triangles are taken from Refs.[51], [52] and [53], respectively.

considerably smaller than the nominal value. The carrier concentration becomes even smaller as the temperature is decreased. For x=1 %, n=1.5×10^{18} m^{-3} at T=77 K and n=4×10^{21} m^{-3} at T=293 K. This suggests trap densities as high as 1×10^{23} m^{-3}. The strong reduction of the free-electron density, observed in our samples at $x > 0.2\%$ and at room temperature suggests that at high N-content the electronic transport is largely governed by trapping of electrons onto deep localised states. In the ultra-dilute regime these deep localised states play a minor role in the electronic conduction.

The strong reduction of the free-electron density is a clear manifestation of the degradation of the crystal quality and electrical properties of $GaAs_{1-x}N_x$ due to the emergence of crystal defects. However, this effect does not entirely correlate with the measured decrease of the Hall mobility. The N-induced quenching of the Hall mobility is observed even in the ultra-dilute regime and tends to saturate to

a value of 0.03 $m^2V^{-1}s^{-1}$ at $x > 0.2\%$. The decrease of mobility with increasing N-content was also reported by other groups (see Fig. 3.2(b)) [51, 52, 53] and is caused by the strong alloy disorder induced by N. A similar effect was also observed in other alloys.

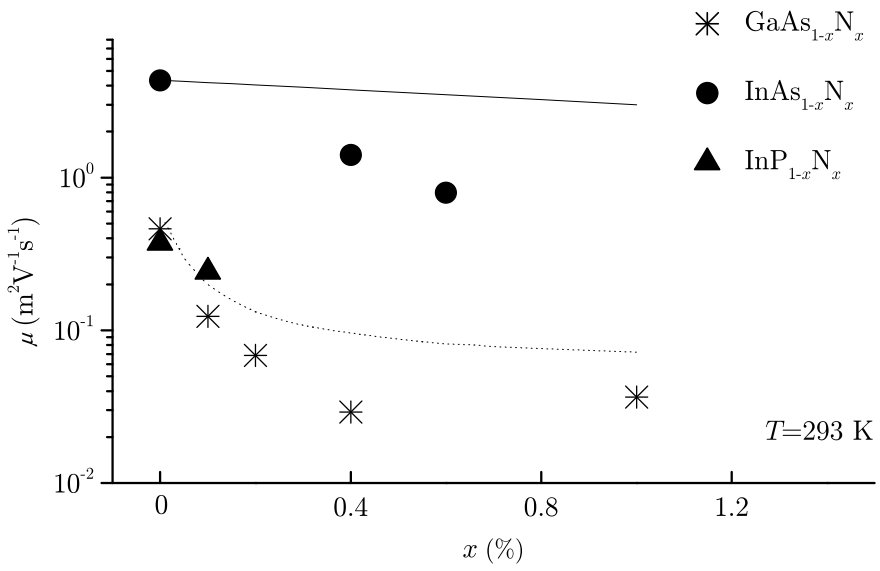

FIGURE 3.3: N-content dependence of measured (symbols) room temperature Hall mobility for n-doped $GaAs_{1-x}N_x$, $InAs_{1-x}N_x$ and $InP_{1-x}N_x$ epilayers. The solid and dotted lines are the calculated N-content mobility dependencies for $InAs_{1-x}N_x$ and $GaAs_{1-x}N_x$, respectively, according to the two-level BAC model [54].

Figure 3.3 shows the dependence of the Hall mobility on N-content at room temperature for three different III-N-V systems, $GaAs_{1-x}N_x$ (samples B), $InP_{1-x}N_x$ (n-doped $InP_{1-x}N_x$ epilayers) and $InAs_{1-x}N_x$ (n-doped $InAs_{1-x}N_x$ epilayers). The symbols in the graph are the measured Hall mobility values. The lines are the calculated N-content dependencies of the electron mobility according to a two-level BAC model. According to this model, the electron mobility is limited by electron

scattering by a random distribution of N-atoms [54] and is given by:

$$\mu^{-1} = \frac{\sqrt{3m^* k_B T}}{e} \pi \left(\frac{m^*}{2\pi\hbar^2}\right)^2 \left(\frac{dE_c}{dx}\right)^2 a^3 x, \tag{3.16}$$

where x is the fractional N-content, k_B is the Boltzmann constant, m^* is the electron effective mass in the alloy at k=0, a is the host material lattice constant and E_c is the energy of the conduction band edge (CBE). By using the two-level BAC model to calculate dE_c/dx and m^* and BAC model parameters for $GaAs_{1-x}N_x$ and $InAs_{1-x}N_x$ from Ref.[32], we find that Eq.3.16 gives qualitatively similar (for $x \sim 0.1$ %) theoretical x-dependencies for μ to those obtained from our experimental data. Additional scattering mechanisms, such as electron scattering by long-range potential fluctuations of the $GaAs_{1-x}N_x$ due to alloy disorder and/or N-related defects, not considered in the model given by Eq.3.16, could account for the discrepancy between the data and the theoretical curve at higher N-content. Increasing the amount of N increases the probability of alloy fluctuations and formation of N-clusters with strongly localised levels. These can trap carriers and act as ionised impurity scattering centres [51]. An improved description of the mobility is obtained by considering electron scattering by the resonant energy levels of N-N pairs [55]. This resonant scattering model predicts μ=0.06 $m^2V^{-1}s^{-1}$ for x= 1% in good agreement with the experimental value (μ=0.04 $m^2V^{-1}s^{-1}$ at T=293 K) [56].

Figure 3.3 also reveals a significant difference between the mobility values for $GaAs_{1-x}N_x$, $InP_{1-x}N_x$ and $InAs_{1-x}N_x$. The $InAs_{1-x}N_x$ samples show a weaker dependence of μ on x: the mobility remains relatively high, 0.62 $m^2V^{-1}s^{-1}$, even at x=0.6 % (T=293 K). In this small gap material, N-impurities and N-N pairs are located at higher energies in the CB than in $GaAs_{1-x}N_x$ and $InP_{1-x}N_x$. As

a result, the perturbation of the InAs CB by N and the strength of resonant scattering is weaker.

The rapid decrease of the Hall mobility in $GaAs_{1-x}N_x$ at N-contents higher than 0.2 % is a clear manifestation of the degradation of the crystal quality due to the emergence of N-related defects. This results in a strong suppression of the electronic conduction due to freezing of electrons onto deep crystal defects levels. At low x (< 0.2 %) these defects does not affect the transport properties. This can be seen from the good agreement between measured Hall mobilities and the two-level BAC model calculated values (see Fig. 3.3). In the next chapter, we will focus on the ultra-dilute ($x \sim 0.1$ %) regime and on the high-field transport.

Chapter 4

Negative differential conductance in bulk $GaAs_{1-x}N_x$

As discussed in Section 1.5, the unique energy dispersion of $GaAs_{1-x}N_x$ gives rise to a novel type of negative differential velocity (NDV) effect and a region of negative differential conductance (NDC) in the current-voltage characteristics, $I(V)$. The NDC in $GaAs_{1-x}N_x$ is a bulk effect and is different from the NDC observed in Gunn structures. In this chapter we investigate this phenomenon in detail. We show how the NDC in $GaAs_{1-x}N_x$ is affected by temperature, light illumination, carrier concentration, N-content and length of the conducting channel.

4.1 $I(V)$ characteristics and negative differential conductance

4.1.1 Modelling current-voltage characteristics

Figure 4.1 shows the $I(V)$ characteristic at T=4.2 K for an n^+-n-n^+ $GaAs_{1-x}N_x$ diode (sample VN456). The current increases monotonically with increasing V up to a critical value, V_C, corresponding to the maximum in the current (see inset in Fig. 4.1). Beyond V_C, the current decreases as V is increased, resulting in NDC. Also, in the bias region of NDC the current exhibits an oscillatory V-dependence.

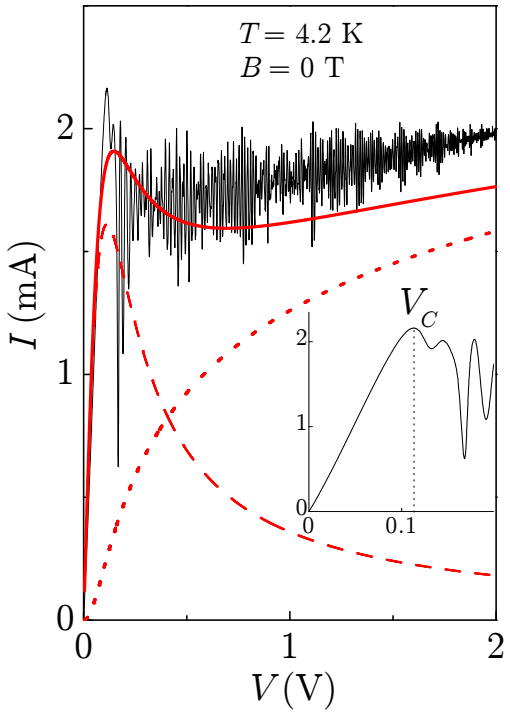

FIGURE 4.1: $I(V)$ characteristic of device VN456 at T=4.2 K and B=0 T. The continuous red line is the calculated $I(V)$ curve, given by the sum of two contributions to the current, i.e. the current due to free-carriers (dashed line) and space charge injected from the electron emitter layer (dotted line). Inset: $I(V)$ curve around V_C.

The NDC is due to a NDV effect, i.e. the decrease of the electron drift velocity, v_d, with increasing electric field, F, above the threshold electric field F_C. Here F_C is defined as F_C=V_C/L, where L=0.6 μm is the thickness of the $GaAs_{1-x}N_x$ layer.

At low F, the average scattering time, τ, is smaller than the time, $\widetilde{\tau}$=$\hbar k_i/eF$, required for a ballistic electron to reach the inflection point, k_i≈4×10^8 m^{-1} of the $\varepsilon(k)$ curve at which the group velocity, v_g=$\hbar^{-1}(\partial\varepsilon/\partial k)$, has a maximum (see Fig. 1.6(b)). Hence, the conduction electrons remain within a range of k-values in which the velocity increases with increasing k. Therefore, an increase of F leads to an increase of v_d. In contrast, for electric fields larger than F_C, $\widetilde{\tau} < \tau$ and electrons can reach the region of k>k_i for which an increase of k decreases the drift velocity. The NDV arises from the dynamical balance between the acceleration of electrons towards the energy of the N-level and the relaxation of electron energy and momentum by scattering processes.

In a previous work [40], it was shown that the $v_d(F)$ curve in $GaAs_{1-x}N_x$ can be described by the simple relation,

$$v_d(F) = \frac{\mu F}{1 + (F/F_C)^2}, \tag{4.1}$$

where μ is the low-field mobility and

$$F_C \approx \hbar k_i r/e. \tag{4.2}$$

Here

$$r = \sqrt{r_i(r_e + r_i)} \tag{4.3}$$

is an average scattering rate, which includes the inelastic scattering rate, r_i, and

the elastic scattering rate, r_e. For a detailed derivation of the $v_d(F)$ dependence in $GaAs_{1-x}N_x$, using a semiclassical model, see Section 1.5.2.

Here we use the form of the $v_d(F)$ curve to describe the measured $I(V)$. As shown in Fig. 4.1, the $I(V)$ data are well described by the sum (continuous line) of two contributions to the current, $I_1(V)$ and $I_2(V)$: $I_1(V)$ (dashed line), which dominates at low bias, is due to the "background" free-electron density, n_0, in the $GaAs_{1-x}N_x$ layer; $I_2(V)$ (dotted line) is due to the space charge current arising from the additional electrons, with density n_s, injected into the $GaAs_{1-x}N_x$ from the negatively biased n^+ GaAs-emitter layer.

The $I_1(V)$ curve is derived from the relations

$$V = FL \tag{4.4}$$

and

$$J = n_0 e v_d, \tag{4.5}$$

where J is the current density. $I_2(V)$ curve is calculated by solving the continuity equation, $J{=}n_s e v_d$, and Poisson's equation using the functional form of $v_d(F)$. The explicit forms of the two current contributions are derived in Appendix A. We obtain the best fit to the data by setting $\mu{=}0.17$ $m^2V^{-1}s^{-1}$ and $n_0{=}2{\times}10^{21}$ m^{-3}. This value of μ is fully consistent with that obtained from independent Hall measurements on modulation-doped $GaAs_{1-x}N_x$ quantum wells with the same N-content as in our sample ($\mu{=}0.20$ $m^2V^{-1}s^{-1}$ at $T{=}2$ K) [51]. The value of μ is small compared to that for pure GaAs due to the strong elastic scattering by the randomly distributed and highly electronegative N-atoms [55, 57].

4.1.2 Effect of channel length

As shown in Fig. 4.2(a), the $I(V)$ characteristics depend on the length of the $GaAs_{1-x}N_x$ channel. The NDC is observed in samples VN456 and VN681 with L=0.6 and 1 μm, respectively, but is quenched in VN683 with L=0.1 μm. This result can be explained by noticing that space charge effects become stronger with decreasing L.

We estimate the density of injected carriers, n_s, by describing the $GaAs_{1-x}N_x$ diode as a parallel-plate capacitor. The value of n_s at the threshold voltage, V_C, for NDC is given by

$$n_s = \frac{\varepsilon V_C}{eL^2}, \tag{4.6}$$

where ε is the permittivity of GaAs. We find that n_s=7×10^{15}, 0.2×10^{15} and 0.1×10^{21} m^{-3} for L=0.1, 0.6 and 1 μm, respectively. Since the background free-electron density is n_0=2×10^{21} m^{-3} (determined from the analysis of the $I(V)$ characteristic of sample VN456, see Section 4.1.1), for the device with L=0.1 μm, n_s>n_0 and therefore the current is governed mainly by the space charge. Increasing the length of the $GaAs_{1-x}N_x$ channel results in a smaller contribution of space charge to the current thus making the NDC more pronounced.

Figure 4.2(b) shows the $I(V)$ characteristics for a series of samples with different channel lengths, L, from 0.1 μm to 1 μm, calculated using the semiclassical model described in Section 4.1.1. A good agreement between the experimental data and the theoretical curves is found.

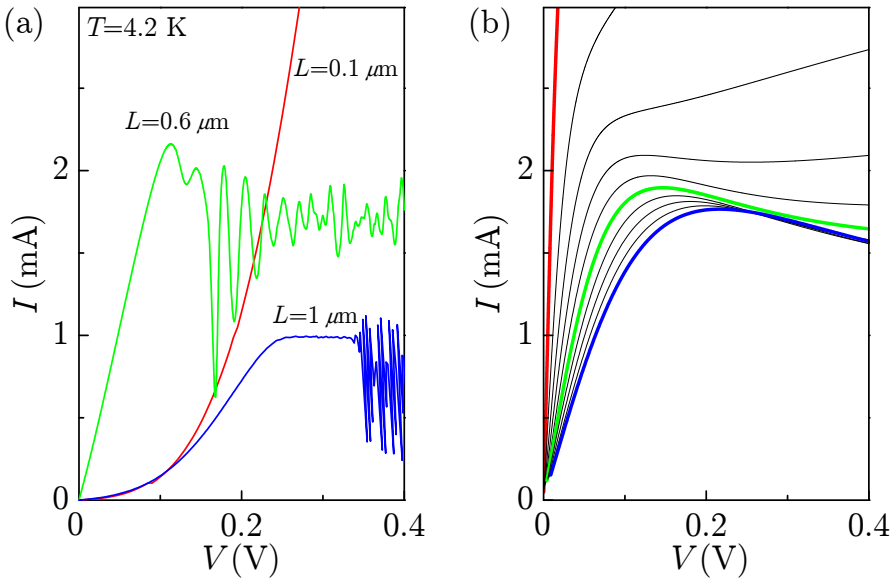

FIGURE 4.2: (a) Measured low-temperature (T=4.2 K) $I(V)$ characteristics of samples VN683, VN456 and VN681 with L=0.1 μm (red line), L=0.6 μm (green line) and L=1 μm (blue line), respectively. All samples consist of circular electrical mesa with diameter d= 20 μm. (b) Calculated $I(V)$ curves for $GaAs_{1-x}N_x$ with L=0.1-1 μm in steps of 0.1 μm. The curves for L=0.1 μm (red line), L=0.6 μm (green line) and L=1 μm (blue line) are highlighted.

4.1.3 NDC and Si doping

As part of the device characterisation, $I(V)$ characteristics of samples with different Si doping in the $GaAs_{1-x}N_x$ layer (Si=1×10^{23} m^{-3} and Si=1×10^{24} m^{-3}) were studied, i.e., VN456 (L=0.6 μm, Si=1×10^{23} m^{-3}), VN680 (L=1 μm, Si=1×10^{24} m^{-3}) and VN682 (L=0.1 μm, Si=1×10^{24} m^{-3}). We observed NDC effects only in samples with Si-concentration of 1×10^{23} m^{-3}. The absence of NDC for high Si doping is likely to be due to the degradation of the crystal quality and electron mobility by strong electron scattering by Si donors and formation of Si-N complexes that are known to form in Si-doped $GaAs_{1-x}N_x$ [50].

4.1.4 Temperature dependence of the NDC

Figure 4.3(a) shows the $I(V)$ curves of device VN456 at different temperatures. The $I(V)$ curves are Ohmic at low bias, followed by a sublinear V dependence of the current or a region of NDC. At low T (4 - 30 K) and high bias, the current is almost independent of V over a wide range of applied biases[1] (see inset in Fig. 4.3(a)). It is also observed that the low-bias conductance for all the $I(V)$ curves is independent of temperature, indicating that the mobility and carrier concentration are independent of T at low electric fields.

Figures 4.3(b) and 4.3(c) show the existence of a thermally activated increase of the high-bias current and of the critical bias V_C for NDC. The value of V_C increases by more than a factor of 5 for T in the range 30 - 80 K. From the Arrhenius plot of the current versus $(k_BT)^{-1}$ at constant bias V=1.5 V (Fig. 4.3(b)), we find that the current follows an exponential dependence on T, i.e.

$$I(T)/I(0) \sim \mathrm{e}^{-\varepsilon_I/k_BT}, \tag{4.7}$$

where ε_I is an activation energy equal to (8±2) meV. This strong T-dependence differs from that observed in other systems with NDC such as Gunn diodes [58] and superlattices [59] in which the temperature effects are much weaker. The thermal smearing of the NDC (see Fig. 4.3) at high temperatures can be explained by the broadening of the energy distribution of the conduction electrons. At these high temperatures an increasing number of electrons are thermally excited out of the N-induced localised states, thus leading to an increase of the *dc* current and a shift of the critical voltage for NDC.

[1]For the $I(V)$ measurements at $T \leq$30 K, the diode was excited with 633 nm laser light and power density $P <$50 Wm^{-2}. For the effect of light on the electrical characteristics of $GaAs_{1-x}N_x$ see Section 4.1.5

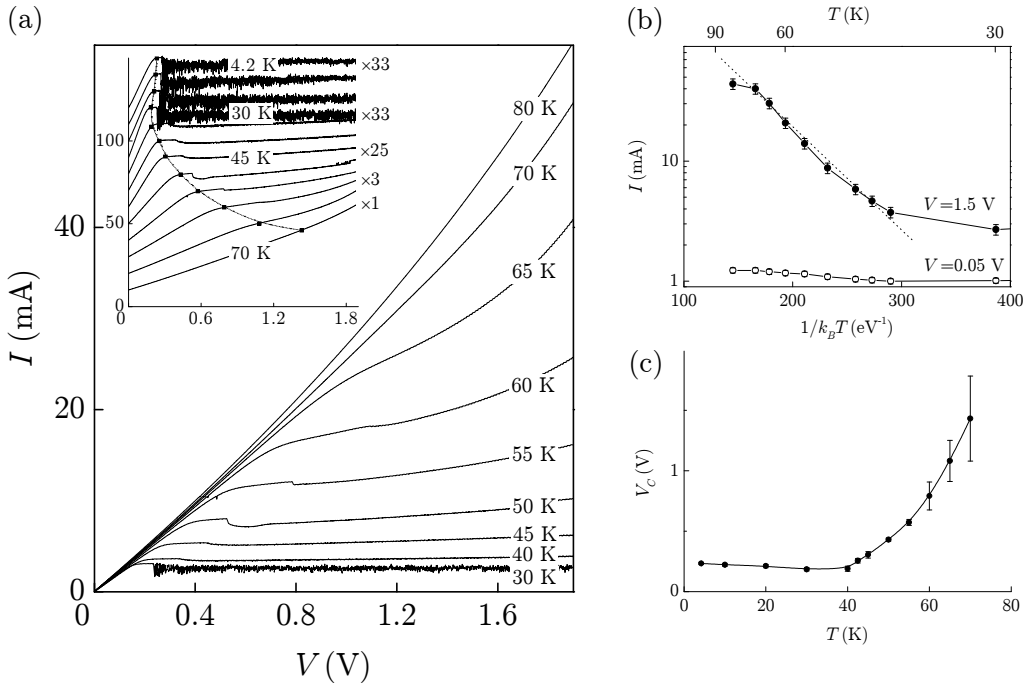

FIGURE 4.3: (a) $I(V)$ curves at different T for a 20 μm diameter mesa diode (VN456). The inset shows the same $I(V)$ curves but normalised to the maximum current value and displaced along the vertical axis. The dotted line is a guide to the eye, showing the temperature shift of the threshold voltage for NDC. (b) Arrhenius plot of current at two constant voltages, showing the existence of a characteristic activation energy at high applied biases (see dotted line). (c) Temperature dependence of the critical field for NDC. The solid line is a guide to the eye, showing thermally activated increase of V_C at T=40 K.

4.1.5 Effect of light and low-frequency oscillations (LFOs)

Figure 4.4(a) shows the low-temperature (T= 4.2 K) $I(V)$ characteristics of device VN456 under different intensities of light illumination. For all measurements, the sample was illuminated with an He-Ne laser (λ_{exc} = 633 nm) and power density, P, less than 100 Wm^{-2}. For clarity the curves in Fig. 4.4(a) are normalised to the maximum current value and displaced along the vertical axis. Each $I(V)$ curve, apart from that with no illumination, exhibits ohmic behaviour up to a threshold voltage, V_C, beyond which it enters a regime of current instabilities.

Excitation of the diode by light (λ_{exc} < 1400 nm) induces low-frequency

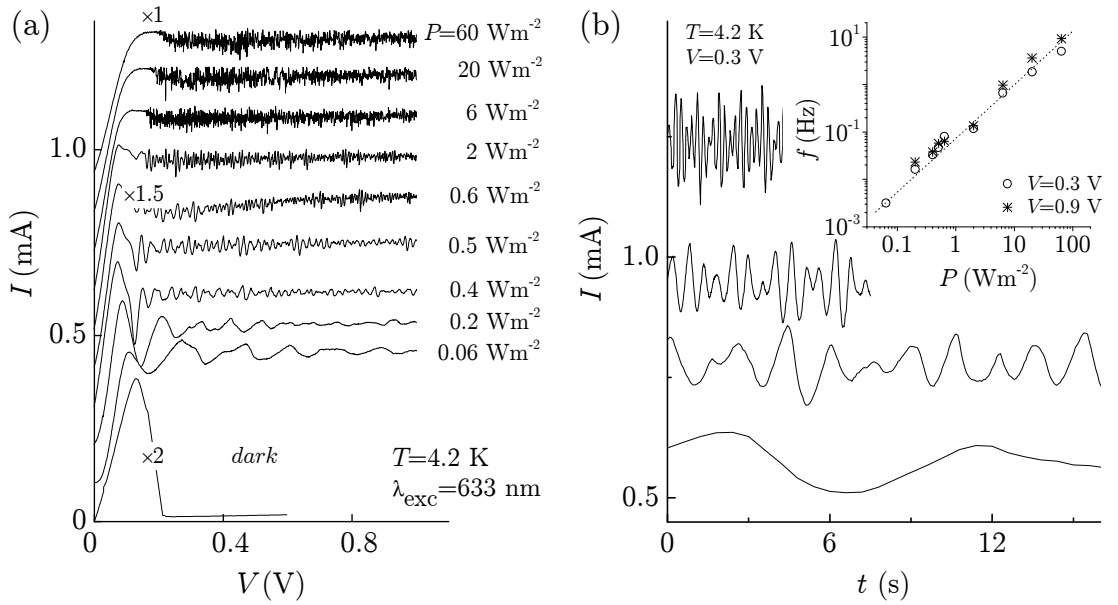

FIGURE 4.4: (a) Low-temperature (T=4.2 K) $I(V)$ under light illumination showing the NDC region and low-frequency current oscillations (LFOs). For photoexcitation, an He-Ne laser was used with $\lambda_{exc} = 633$ nm and $P \leq 60$ Wm^{-2}. (b) Time (t) dependence of I at T =4.2 K and V =0.3 V for a 20 μm diameter mesa diode. For these measurements, the diode was excited with 633 nm laser light. From the bottom to the top, different curves correspond to increasing excitation power densities (P=2, 6, 20, and 60 Wm^{-2}). The inset shows the P dependence of the frequency f of the current oscillations at V =0.3 V and V =0.9 V (T =4.2 K).

oscillations (LFOs) in the low-T current at high *dc* bias ($V > 0.1$ V). The frequency f (< 1 Hz) of these LFOs increases with increasing excitation power P, but is only weakly affected by the applied bias, see inset in Fig. 4.4(b).

The NDC is also observed in the absence of light. When the applied bias is increased from zero without light illumination, the conductivity suddenly drops at a critical voltage $V \sim 0.1$ V and remains very low as the bias is increased further. When the bias is then returned to a low value ($V < 0.1$ V), the low-bias conductivity recovers only very slowly, i.e., the current increases slowly with time until it saturates to a steady value I_0 according to the relation

$$I(t) = I_0(1 - \mathrm{e}^{-t/\tau}), \tag{4.8}$$

where τ is a characteristic T-dependent recovery time, see Fig. 4.5. Alternatively, the conductivity can be restored quickly by light of wavelength $\lambda_{exc} < 1400$ nm.

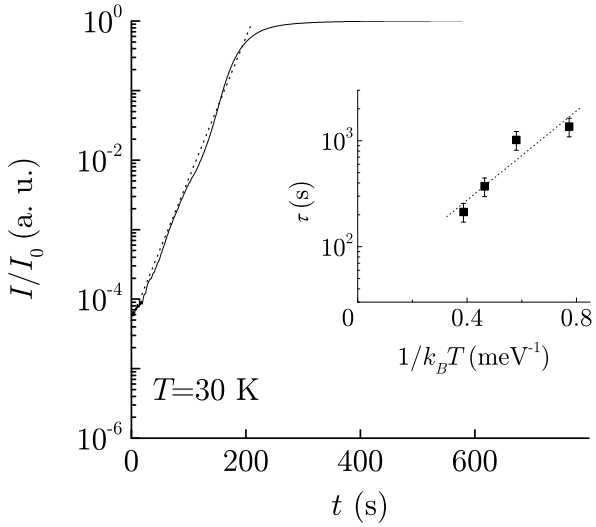

FIGURE 4.5: Time (t) dependence of I at T =30 K and V =0.05 V for a 20 μm diameter mesa diode. For these measurements, we first applied a bias voltage ($V > 0.2$ V) to the diode, then we removed it and measured the t-dependence of I at V =0.05 V and in the dark. The inset shows Arrhenius plot of the recovery time τ. The dotted line is a linear fit to the data.

The slow transients and LFOs observed at low T are similar to those reported previously for SI GaAs. These phenomena have been attributed to electric field-enhanced trapping of electrons at localised states associated with EL2-type native defects [60]. Although the precise microscopic nature of this defect is still unclear, there is consensus that an EL2 defect involves an As-antisite (As_{Ga}). In SI GaAs, hot electrons are captured by the EL2 defect through a multiphonon emission process after which the electron remains "frozen" onto a metastable excited state EL2*. This capture process is accompanied by a pronounced local distortion of the crystal lattice. Spatial variations in the density of trapped electrons also lead to slow high-electric-field domains and LFOs of the current with frequency that increases linearly with the intensity of laser power [61, 62], as observed in

our experiment (Fig. 4.4(b)). We propose that a similar field-enhanced electron trapping can also take place in n-type $GaAs_{1-x}N_x$ at low T (< 40 K), although the nature of the trapping center and/or trapping mechanism could be different in this case and may also involve the N-atoms.

As shown in Fig. 4.5, in the temperature range 4−40 K, the recovery time of the current, τ, has an exponential dependence on T, i.e.,

$$\tau(t)/\tau(0) = \mathrm{e}^{\varepsilon_\tau/k_B T}, \tag{4.9}$$

where $\varepsilon_\tau = 4 \pm 1$ meV. This indicates that electrons frozen onto localised states are slowly released by thermal excitation into the CB with a small activation energy ε_τ.

These data indicate that the electron dynamics at low temperature (4 - 40 K) is slow due to a field-enhanced trapping of carriers at localised states, possibly associated with EL2 defects. This leads to very slow (f <1 Hz) frequency current oscillations above a critical electric field. In Chapter 6 we show that this slow dynamics is replaced at higher temperatures (T >40 K) by a fast response of the current in the sub-terahertz frequency range.

Chapter 5

Magneto-transport studies of $GaAs_{1-x}N_x$

In this chapter we examine the effect of a magnetic field (B) on the electron dynamics in $GaAs_{1-x}N_x$. We observe a modulation of the threshold electric field, F_C, for the NDC as a function of B: F_C is enhanced by B when electrons can relax energy by inter-Landau level transitions involving the emission of longitudinal optical (LO) phonons. This magnetophonon resonance (MPR) effect provides a means of measuring the N-induced enhancement of the electron effective mass and of probing the electron dynamics. Also, we show that, in the geometry in which B is perpendicular to the direction of current, the trajectory of conduction electrons becomes fully localised in real space when the ratio of applied electric and magnetic fields reaches a critical value. This provides a novel means of tuning the NDC.

5.1 Electron effective mass and Si-donor binding energy in $GaAs_{1-x}N_x$

In this section we study the magnetoresistance of the dilute nitride alloy $GaAs_{1-x}N_x$ in magnetic fields up to 47 T. We observe a strong magnetophonon resonance effect and a large transverse magnetoresistance, which provide a means of measuring the N-induced enhancement of the electron effective mass and of investigating the magnetic freeze-out of conduction electrons onto Si donors in $GaAs_{1-x}N_x$.

5.1.1 Longitudinal and transverse magnetoresistance

The $I(V)$ characteristics and NDC observed in our $GaAs_{1-x}N_x$ structures are strongly affected by a magnetic field applied parallel or perpendicular to the direction of current.

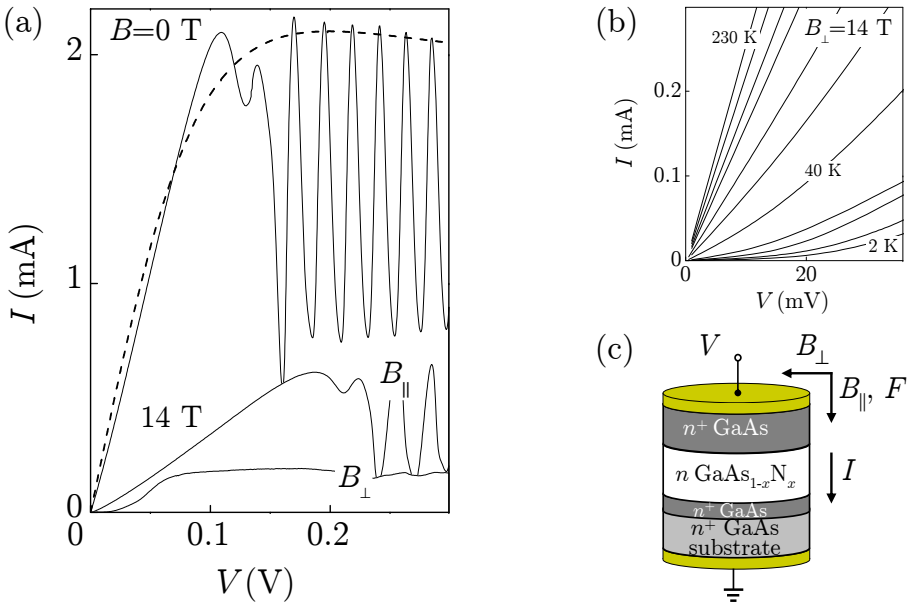

FIGURE 5.1: (a) Low-temperature (T=4.2 K) $I(V)$ curves for sample VN456 at B=0 T and in $B_\perp$ and $B_\parallel$ with B=14 T. The dashed line is a fit to the data at B=0 T using the semiclassical model described in Section 4.1.1. (b) T-dependence of the $I(V)$ curve at $B_\perp$=14 T (T =2, 10, 20, 30, 40, 50, 60, 80, 100, 150 and 230 K). (c) Schematic diagram of the diode and orientation of electric (F) and magnetic (B) field.

Figure 5.1(a) shows the low-temperature (T=4.2 K) $I(V)$ characteristics of an n^+-n-n^+ $GaAs_{1-x}N_x$ heterostructure (VN456) at B=0 T and in a magnetic field B=14 T applied parallel ($B_\parallel$) or perpendicular ($B_\perp$) to the electric field, F. At B=0 T, the $I(V)$ curve exhibits ohmic behaviour up to a threshold voltage beyond which it enters a regime of NDC and of instability in the current. The $I(V)$ curve is strongly modified in $B_\perp$. In this configuration, the magnetic field suppresses the current at low-bias voltages below a threshold value $V \sim 0.05$ V. Note that in the $B_\parallel$ configuration the effect of B on the current and NDC is weaker. The B-dependence of the magnetoresistance, $R = V/I$, in the $B_\perp$ configuration is shown in Fig. 5.2 for different temperatures and low applied bias (V=0.01 V). In this geometry and at low temperature, the value of R can increase by more than a factor of 10^2 in a field of 14 T. This effect becomes weaker at higher T (Figs. 5.1(b) and 5.2).

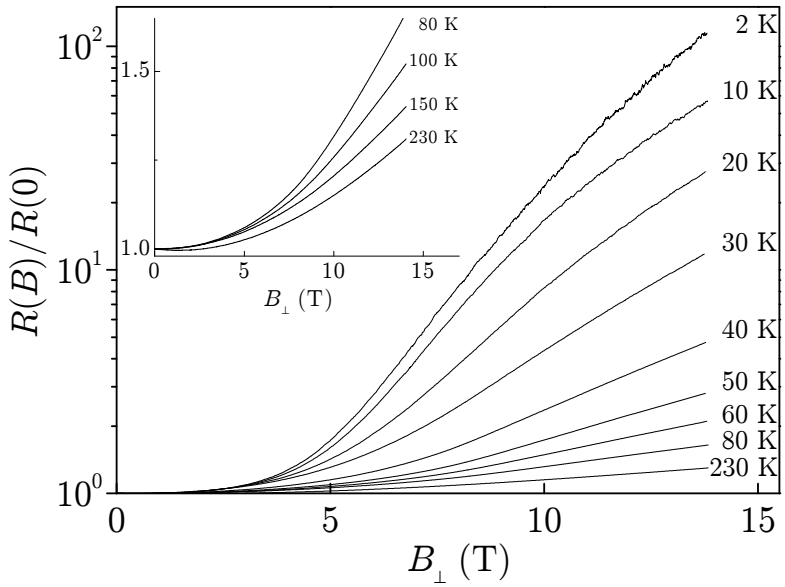

FIGURE 5.2: B-dependence of the transverse magnetoresistance at V =0.01 V and different T. The inset shows the transverse magnetoresistance at high T.

We also observe an oscillatory effect in the magnetoresistance at higher magnetic fields and $V > 0.03$ V, see Fig. 5.3(a). Data shown in this figure were obtained using a nondestructive pulsed (∼40 ms) magnetic field system up to 47 T and the measurements were taken during the down sweep of B. To reveal the oscillatory component of $R(B)$, in Fig. 5.3(a) we also plot the second derivative $-d^2R/dB^2$. The maxima in this quantity correspond to the resonant peaks in the oscillatory component of $R(B)$.

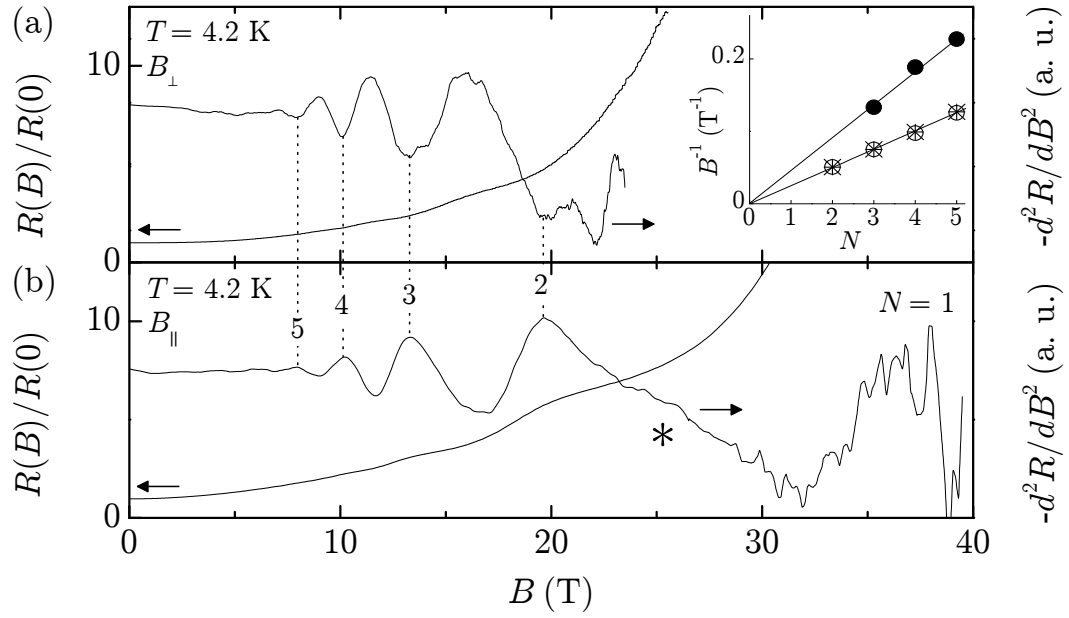

FIGURE 5.3: B-dependence of R and $-d^2R/dB^2$ at T=4.2 K and V= 0.09 V in (a) $B_\perp$ and (b) $B_\parallel$. The asterisk (∗) in part (b) marks a region of two phonons assisted inter-LL transitions. The inset in part (a) shows positions in $1/B$ of the minima and maxima in $-d^2R/dB^2$ as a function of N (N integer) at T=4.2 K. Circles and stars correspond to $B_\parallel$ and $B_\perp$, respectively. The dot symbols are for all-GaAs diodes from Ref. [63]. The lines are linear fit to the data.

By comparing the traces for $B_\parallel$ and $B_\perp$, it can be seen that maxima in $R(B_\parallel)$ correspond closely to minima in $R(B_\perp)$ (Figs. 5.3(a) and 5.3(b)). Note that in the $B_\perp$ geometry the magneto-oscillations cannot be observed at high $B_\perp$

(> 25 T) and/or low bias ($V < 0.03$ V). Under these conditions, the transverse magnetoresistance shows a large increase with $B_\perp$, making impossible reliable low-noise measurements of the relatively weak magneto-oscillations. The magneto-oscillations in $R(B)$ are observed in $B_\parallel$ and $B_\perp$ up to a temperature $T \sim 100$ K, above which both the oscillatory and monotonic magnetoresistance effects become very weak (Figs. 5.4 and 5.5).

5.1.2 Magnetophonon resonance and electron cyclotron mass

The magneto-oscillations in $R(B)$ shown in Fig. 5.3 arise from a magnetophonon resonance (MPR) effect. In the $B_\perp$ orientation, we observed that the minima in $-d^2R/dB^2$ (maxima in the current) occur when a multiple of the Landau level spacing, $\hbar\omega_C$, matches the energy of an LO phonon, $\hbar\omega_{LO}$, i.e., when the condition

$$\omega_{LO} = N\omega_C, \tag{5.1}$$

is satisfied. Here $\omega_C{=}eB/m^*$ is the cyclotron frequency, N is an integer and represents the LL index, and m^* is the electron cyclotron mass. Equation 5.1 is sometimes referred to as the MPR condition and corresponds to the condition at which the rate of inelastic scattering by LO phonons is resonantly enhanced, enabling current flow along the electric field direction [64]. The LLs are only resolved for $\mu B > 1$. Using our estimate of $\mu = 0.17$ m^{2}V^{-1}s^{-1} (see Section 4.1.1), we estimate a value of $B > 6$ T for magnetophonon oscillations to be resolved. We note that the measured MPR at $T < 60$ K is a hot electron effect: At these temperatures ($T < 60$ K) there are very few thermally activated LO phonons and under the large applied electric fields (> 0.1 kVcm^{-1}) used in our experiment, electrons acquire sufficient energy to emit an LO phonon [64].

Also we note that the behaviour of the magnetoconductivity in these n^+-n-n^+ $GaAs_{1-x}N_x$ samples is different from that of conventional Hall bar. Since the diameter (20 μm) of the mesa is considerably larger than the thickness (0.6 μm) of the $GaAs_{1-x}N_x$ layer, the Hall electric field is effectively short circuited by the highly conducting n^+ GaAs cladding layers (the n^+ GaAs/$GaAs_{1-x}N_x$ interfaces are equipotential surfaces to a good approximation) and in the $B_\perp$ configuration, no significant Hall voltage is generated in the thin $GaAs_{1-x}N_x$. Therefore, the measured transverse magnetoresistance is proportional to the inverse of the longitudinal conductivity, i.e., $R \sim \sigma_{xx}^{-1}$, rather than $R \sim \sigma_{xx}/\sigma_{xy}^2$ as is the case for Hall bars in the high-magnetic-field limit [65].

For the $B_\parallel$ geometry, we observe maxima rather than minima in the plot of $-d^2R/dB^2$ vs $B_\parallel$ (Fig. 5.3(b)). In this configuration, the cooling of hot electrons by LO phonon emission reduces the current flow along the direction of F thus enhancing R. The extended shoulder in $R(B)$ at around 27 T (marked by an asterisk in Fig. 5.3(b)) can be attributed to a subtle MPR process involving competition between different types of inter-LL scattering transitions with two phonons [64].

As shown in the inset of Fig. 5.3(a), the positions in $1/B$ of the maxima or minima of $-d^2R/dB^2$ plotted as a function of the integer N fall on a straight line which extrapolates to $N = 0$ at $1/B = 0$. From the linear fit to the data, we obtain the fundamental field B_f=40±3 T at which the cyclotron energy is equal to $\hbar\omega_{LO}$. Using the period $B_f^{-1} = P(1/B) = 0.025 \pm 0.002$ T^{-1} in the maxima and/or minima of $-d^2R/dB^2$, we derive an electron cyclotron mass

$$m^* = e/\omega_{LO}P = (0.13 \pm 0.01)m_e, \tag{5.2}$$

where m_e is the free-electron mass. Our measured value of m^* in $GaAs_{1-x}N_x$ is

larger than those derived (m^*=0.08m_e) from a two-level BAC model[1] for x=0.1 %. Our value of m^* agrees with that obtained from independent optical experiments on other $GaAs_{1-x}N_x$ samples (m^*=0.11-0.13m_e) [27] and with that predicted by a modified BAC model that takes into account the effect of N-clusters on the electron effective mass (m^*=0.12m_e) [26]. The values of m^* are also significantly larger than those measured (m^*=0.070m_e) in our control sample, an all-GaAs n^+-n-n^+ diode, see dots in the inset in Fig. 5.3(a) [63, 65]. The estimated values of m^* provide direct evidence of the strong effect of low concentrations of resonant N-atoms on the electronic properties of GaAs.

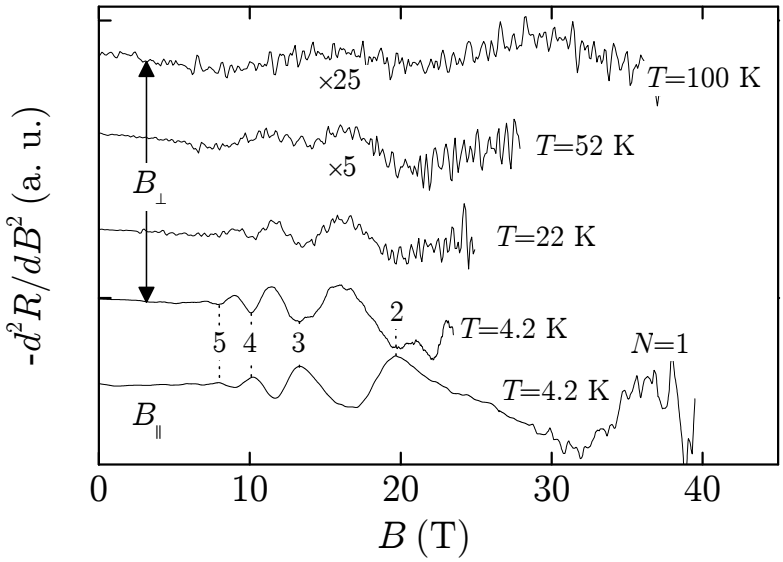

FIGURE 5.4: B-dependence of $-d^2R/dB^2$ in $B_\perp$ (T=4.2, 22, 52 and 100 K) and $B_\parallel$ (T=4.2 K).

As shown in Fig. 5.4, the amplitude of the magnetophonon resonances decreases with increasing T. The width of the MPR resonances is weakly affected by temperature up to $T \sim 20$ K above which it tends to increase due to the increasing

[1]The cyclotron mass is $m^*=\hbar^2 k/(\partial\varepsilon/\partial k)$ and is derived from the $\varepsilon(k)$ dispersion of $GaAs_{1-x}N_x$, i.e., $\varepsilon(k)=\frac{1}{2}\left\{[E_M(k)+E_N]-\sqrt{[E_M(k)-E_N]^2+4V_{MN}^2}\right\}$ (see Section 1.5.1). At the MPR condition, the hot electrons have a cyclotron mass larger than that at k=0. In the range of magnetic fields considered here, we estimate that the enhancement of m^* is $\leq$15%.

broadening of the LLs. We find that the oscillatory part of R is well described by the empirical formula of Stradling and Wood [66],

$$\Delta R(B) = \pm R(0) \mathrm{e}^{\frac{-2\pi\Gamma}{\hbar\omega_C}} \cos\left(\frac{2\pi\omega_{LO}}{\omega_C}\right), \tag{5.3}$$

where the positive (negative) sign refers to the perpendicular (parallel) orientation and $\Gamma = 12 \pm 1$ meV is the energy broadening of the LLs at T=4.2 K. This value of Γ is larger than that measured for MPR in the Ohmic regime of high-mobility n-GaAs ($\Gamma < 4$ meV) [67] and is consistent with the strong electron scattering by the single N-atoms and N-clusters in the $GaAs_{1-x}N_x$ alloy [51, 55, 68, 69].

In the $B_\parallel$ orientation, the amplitude of the MPR oscillations are weakly affected by the applied bias and the oscillations are clearly observed at high $B_\parallel$ (Fig. 5.3(b)). In contrast, in the $B_\perp$ geometry, the oscillations dampen out and disappear completely at low voltages or high $B_\perp$ (> 25 T). In the following section we consider how, under these conditions, the magnetic field induces freeze-out of electrons onto localised states and leads to a transition from extended state band-like to hopping-like conduction. MPR oscillations can only be observed when free electrons dominate the conductivity, a condition which is not satisfied at low-bias voltages and/or high $B_\perp$ and low T.

5.1.3 Magnetic field induced "freeze-out" of electrons and Si-donor binding energy in $GaAs_{1-x}N_x$

The large magnetoresistance observed in the $B_\perp$ geometry at low bias ($V \sim 0.01$ V) and at $T < 100$ K (Fig.5.2) suggests that under these conditions, the magnetoresistance is largely governed by the presence of localised electron states close to

the conduction band edge. The localised energy levels associated with N and the Si-donor dopant atoms in the $GaAs_{1-x}N_x$ layer can bind electrons at low temperatures ($T < 20$ K), resulting in charge transport via thermally activated hopping between localised states. Hopping conduction is highly sensitive to magnetic field, which tends to compress the bound electronic wave function and increase the magnetoresistance due to a smaller overlap of the wave function tails between adjacent localised states below the band edge. Since electrons hop preferentially along the direction of B in which the magneto-compression of the electron wavefunction is weaker, the hopping magnetoresistance in the $B_{\parallel}$ orientation is smaller than that in $B_{\perp}$ [70]. For the $B_{\perp}$ configuration, we find that

$$R(B)/R(0) \sim \mathrm{e}^{B/B_0}, \tag{5.4}$$

with $B_0 = 3 \pm 1$ T at low bias ($V < 0.05$ V) and T=4.2 K. According to a simple model of hopping conduction,

$$B_0 = 4n_h^{2/3}\hbar/e, \tag{5.5}$$

where n_h is the density of localised states corresponding to a characteristic hopping length $l = n_h^{-1/3}$ [70]. The value of $B_0 = 3 \pm 1$ T gives $l = 31 \pm 5$ nm corresponding to $n_h = (4 \pm 2) \times 10^{22}$ m^{-3}, which is close to the nominal doping density of Si donors (10^{23} m^{-3}) in the $GaAs_{1-x}N_x$ layer. This suggests that the localised states between which the electrons are hopping at low temperatures are associated with shallow hydrogenic Si donors rather than minima in the disorder potential due to the high concentration of N-atoms ($\sim 2 \times 10^{25}$ m^{-3} for x=0.1%).

At low temperatures (T=4.2 K), increasing the applied bias above a threshold

value (∼20 mV) leads to a rapid increase of current and decrease of magnetoresistance, which we attribute to ionization of electrons out of the localised states (see Fig. 5.1(b)). Here we consider the low-bias magnetoresistance ($V < 0.05$ V) and its T-dependence. Whereas at low T (2 - 30 K) and $B_\perp > 8$ T, the transverse magnetoresistance has an exponential-like dependence on B, characteristic of hopping conduction, for high T (> 100 K), it has a quadratic B-dependence (Fig. 5.2), which is consistent with a regime of conduction through extended band states. We therefore focus on an intermediate temperature range, i.e., T=30 - 100 K, in which the temperature dependence of the magnetoresistance is mainly determined by the rapid increase in free-electron concentration due to thermal excitation into the conduction band of electrons "frozen" onto the Si donors in the presence of a high $B_\perp$.

As shown in Figs. 5.5(a) and 5.5(b), in the temperature range T=30 - 100 K, the magnetoresistance at high $B_\perp$ (> 8 T) approximates to an exponential T-dependence, i.e.

$$R(T)/R(0) \sim \mathrm{e}^{\Delta\varepsilon/k_B T}, \tag{5.6}$$

where $\Delta\varepsilon$ is a characteristic activation energy into the conduction band. In the low-temperature range ($T < 30$ K), the T-dependence of R is weaker, consistent with thermally activated hopping between localised states [70]. We find that the value of $\Delta\varepsilon$ increases from 7 to 12 meV for $B_\perp$ increasing from 9 to 14 T (Fig. 5.5(c)). An increase in the activation energy with $B_\perp$ has been observed previously in other semiconductor materials and attributed to magnetic freeze-out of conduction electrons onto donor impurity states due to the B-induced increase of the donor binding energy [70, 71, 72, 73].

For our n-doped $GaAs_{1-x}N_x$, at low $B_\perp$, $\Delta\varepsilon$ tends to approach a value of about 5 meV, which is consistent with thermal activation of electrons out of

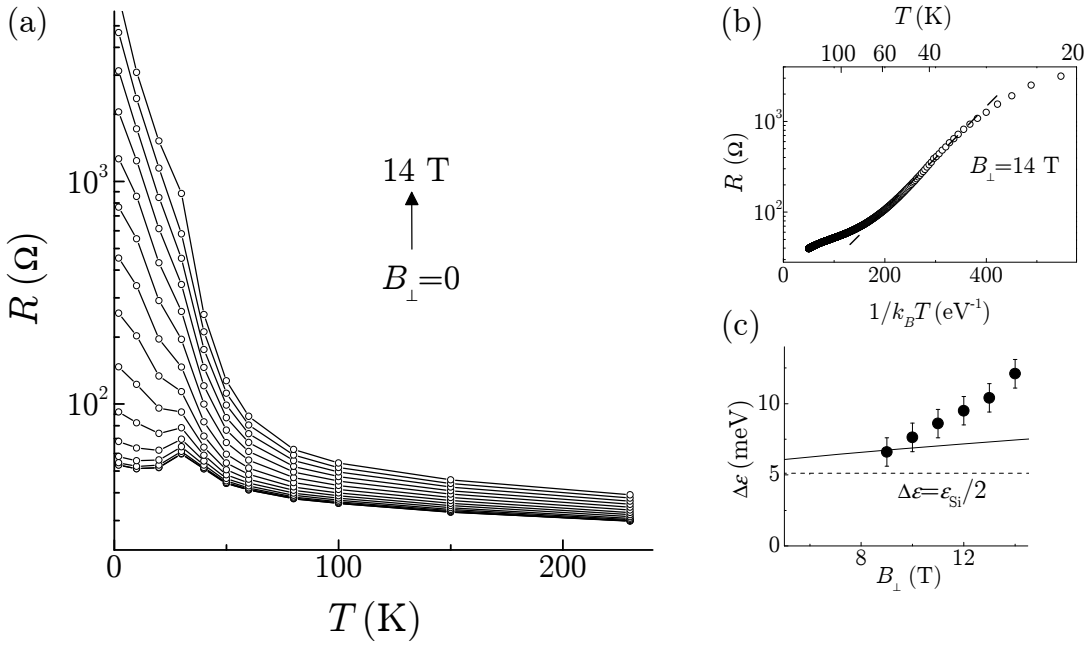

FIGURE 5.5: (a) T-dependence of R in $B_\perp$ up to 14 T (V=0.01 V). (b) Arrhenius plot of R at $B_\perp$=14 T. The line is an exponential fit to the data. (c) Measured B-dependence of the activation energy $\Delta\varepsilon$. The continuous line is the calculated B-dependence of $\Delta\varepsilon$ according to an hydrogenic model, using the electron effective mass and the binding energy of a Si donor in $GaAs_{1-x}N_x$ as input parameters. The dashed line is the calculated value of $\Delta\varepsilon$ at B=0 T.

Si-donor states into the conduction band, as the following argument shows. To estimate the value of $\Delta\varepsilon$, we use a hydrogenic model for Si donors in $GaAs_{1-x}N_x$. For our measured value of $m^* = (0.13 \pm 0.01)m_e$ in $GaAs_{1-x}N_x$, this gives a donor binding energy

$$\varepsilon_{\mathrm{Si}} = R_\infty (m^*/m_e)\varepsilon_r^{-2} = (10.2 \pm 0.8)\ \mathrm{meV} \tag{5.7}$$

and a Bohr radius

$$a = \varepsilon_r (m_e/m^*)a_0 = (54 \pm 4)\ \text{Å}, \tag{5.8}$$

where ε_r=13.2 is the relative permittivity, R_∞ = 13.6 eV≡1 Ry is the Rydberg constant and a_0=0.53 Å is the Bohr radius of the hydrogen atom. Note that our

estimated value of $\varepsilon_{\rm Si} = 10.2$ meV is significantly larger than that obtained for GaAs ($m^* = 0.07m_0$, $\varepsilon_{\rm Si} = 5.5$ meV). Due to the high Si doping, we can assume that our $GaAs_{1-x}N_x$ layer is uncompensated and that the chemical potential is midway between the donor level and the band edge. Thus $\Delta\varepsilon = \varepsilon_{\rm Si}/2 = 5.1$ meV, which is close to the measured values of $\Delta\varepsilon$ at low $B_\perp$ (Fig. 5.5(c)). Our measurements of the N-induced enhancement of m^* and of $\varepsilon_{\rm Si}$ and the corresponding decrease of the electron Bohr radius a are clear manifestations of the strong effect of N on the electronic properties of GaAs. Although a N-induced increase of $\varepsilon_{\rm Si}$ was predicted in previous work [74], to our knowledge, it has not been observed previously in experiments.

As shown in Fig. 5.5(c), the B-dependence of $\Delta\varepsilon$ ($= \varepsilon_{\rm Si}/2$) deduced from our analysis is different from that calculated using a simple hydrogenic-effective mass model [75] that uses as input parameters the electron effective mass ($m^* = 0.13m_e$) and the zero field binding energy ($\varepsilon_{\rm Si} = 10.2$ meV) of a Si donor in $GaAs_{1-x}N_x$. Our measured value of $\Delta\varepsilon$ increases with $B_\perp$ more strongly than the calculated one. This discrepancy may be due to the strong effect of $B_\perp$ on the nature, band-like or impurity-like, of the Si-related states. In our highly Si-doped $GaAs_{1-x}N_x$ layer, at B=0 T, the donor wavefunctions tend to overlap. The value of a=54 Å at B=0 T gives a critical value of the Si-concentration $n \approx 1.3 \times 10^{23}$ m^{-3} for the metal-insulator transition (MIT) ($na^3 \approx 0.02$), which is close to the nominal Si doping of our sample (1×10^{23} m^{-3}). An increasing magnetic field increases the binding energy $\varepsilon_{\rm Si}$ of isolated Si donors and also compresses the electronic wavefunction, thus increasing the magnetoresistance due to the decreasing overlap of the wavefunction tails between adjacent localised states [71, 72, 73]. According to the hydrogenic model [75], when $B_\perp$ is increased from 0 to 14 T, the compression of the donor wavefunction reduces the effective Bohr radius from 54 to 37 Å,

which corresponds to $na^3 = 0.005$, somewhat below the critical value $na^3 = 0.02$ for the MIT. It therefore seems likely that at high $B_\perp$, the T-dependence of the magnetoresistance is also influenced by the B-dependence of the overlap donor wavefunctions.

The effect of high magnetic fields on the activation energy into the conduction band and the spatial overlap between the localised states are clearly quite complex, especially for the case when the doping concentration is close to the MIT and when the effect of the N-induced disorder also needs to be considered. Further experiments involving a range of doping concentrations above and below the MIT coupled with a quantitative theoretical model are probably needed to provide a complete picture of the interplay of temperature, magnetic field, and applied bias in the freeze-out regime of this material system.

5.2 Modulation of the NDC by magnetophonon resonance

The previous section focussed on the electronic conduction in $GaAs_{1-x}N_x$ at different temperatures and applied magnetic and electric fields. It was established that the magnetic field, applied both parallel and perpendicular to the direction of the current, affects strongly the electronic conduction. In this section we consider in detail the electron dynamics in the NDC region and in the $B_\parallel$ configuration. Figure 5.6(a) shows the $I(V)$ characteristics at T=4.2 K for VN456 and magnetic fields from 0 to 23 T. In the $B_\parallel$ configuration, along with a suppression of the current at all biases, we also observe a non-monotonic shift of the threshold voltage,

V_C, for NDC. For $B_\parallel$ up to about 9 T, V_C shifts steadily to higher values, followed by an oscillatory dependence at higher magnetic fields (see inset of Fig. 5.6(a)).

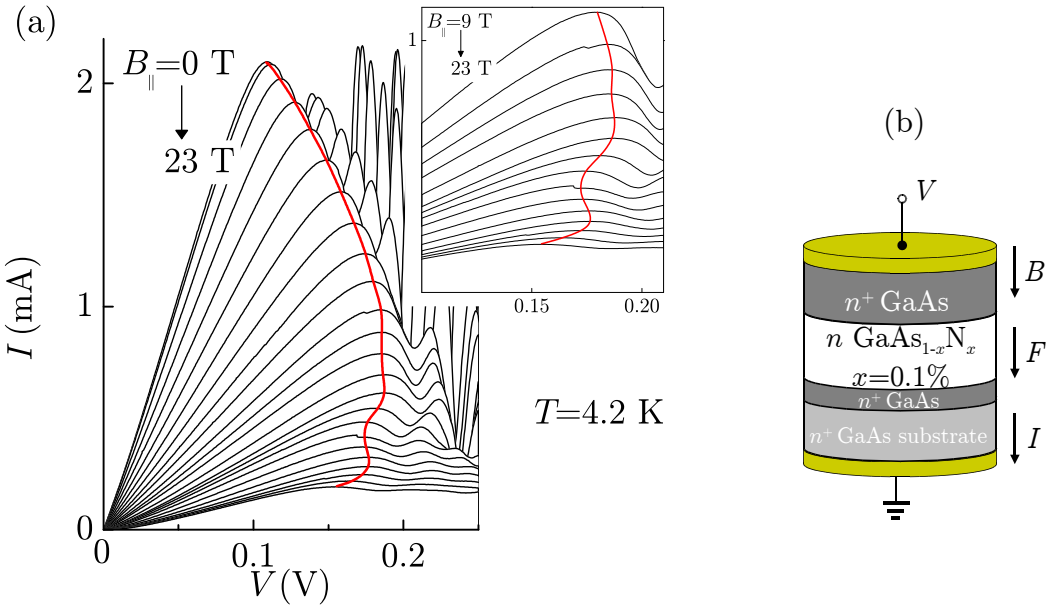

FIGURE 5.6: (a) $I(V)$ characteristic at T=4.2 K for magnetic fields from 0 to 23 T in steps of 1 T. The red line is a guide to the eye, highlighting the modulation of the threshold voltage V_C induced by $B_\parallel$. Inset: magnified $I(V)$ curves for $B_\parallel$ from 9 to 23 T. (b) Schematic of the device with arrows indicating the direction of the current (I), electric (F) and magnetic (B) fields.

The B-dependence of the threshold electric field for NDC, F_C, is shown in Fig. 5.7(c). The plot reveals shoulders/maxima in F_C at $B_\parallel$=10, 13 and 20 T. Magneto-oscillations in the longitudinal magnetoresistance, R, are also observed, see Fig. 5.7(a). At B=0, the resistance of our $GaAs_{1-x}N_x$ diode is R=50 Ω. This value of R and the amplitude of magneto-oscillations in $R(B)$ are much larger than those associated with the n^+ GaAs buffer and cap layers (<0.1 Ω), implying that in the experiment we probe the properties of the $GaAs_{1-x}N_x$ layer, rather than those of GaAs cap layers.

To reveal the oscillatory component of $R(B)$ more clearly, in Fig. 5.7(b) we plot the second derivative $-d^2R/dB^2$. Maxima in this quantity correspond to

the resonant peaks in the oscillatory component of $R(B)$ and coincide with the B-positions of the shoulders/maxima in F_C. In both cases the oscillations are damped at low magnetic field ($\mu B \leq 1$). Maxima in the longitudinal magnetoresistance are typically observed under hot electron conditions in which the electron gas is out of equilibrium with the lattice and arise from the cooling of the electron distribution by emission of LO phonons [64]. Our data clearly indicate that this process is also accompanied by magneto-oscillations in the critical field for NDC.

As discussed in Section 4.1.1, the form of the $v_d(F)$ curve provides a simple relation between F_C and the average scattering rate, r. The critical field for NDV is $F_C \approx \hbar k_i r/e$, which we can rewrite as $\widetilde{\tau} r \approx 1$, where $\widetilde{\tau}$ is the time taken by an electron to accelerate ballistically from rest to the inflection point k_i in $\varepsilon(k)$ at $F = F_C$. Therefore, by studying the B-dependence of F_C, the scattering rate and its effect on the electron dynamics and NDC can be probed.

As seen in Fig. 5.7(c) F_C increases monotonically with magnetic field up to 10 T. This behaviour is attributed to the enhanced electron elastic scattering associated with the high density of states of the LLs at k=0 [76]. Higher magnetic fields induce a resonant modulation of F_C: maxima in F_C as a function of $B_\parallel$ occur when a MPR condition (Eq. 5.1) is satisfied. The value of $B_\parallel = 9$ T at which the oscillations in F_C are well resolved in the experiment is close to the estimated value of $B_\parallel > 6$ T for magnetophonon oscillations in R (see Section 5.1.2).

Using our measured value of μ=0.17 $\mathrm{m^2V^{-1}s^{-1}}$ at B=0 T (see Section 4.1.1) and of m^*=0.13m_e, we derive a relaxation rate for the electron velocity

$$r_v = r_i + r_e = e/m^*\mu = 0.8 \times 10^{13}\ \mathrm{s^{-1}}. \tag{5.9}$$

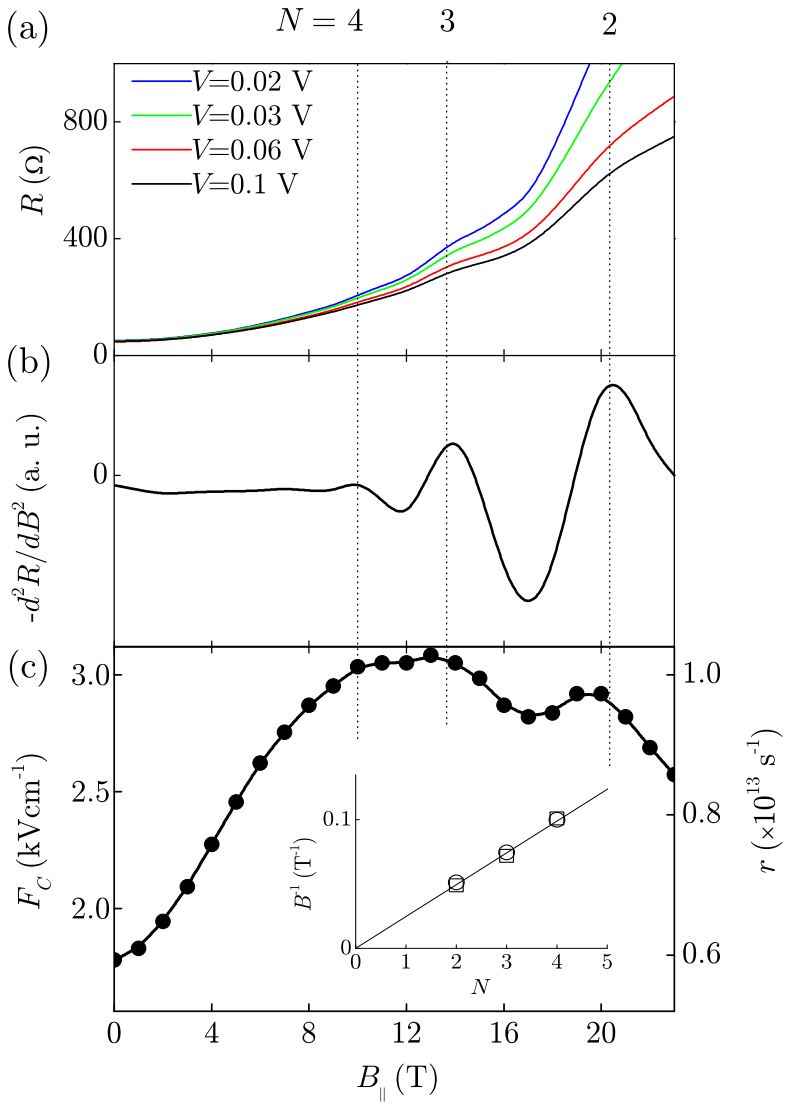

FIGURE 5.7: (a) Magnetic field dependence of the longitudinal magnetoresistance, measured under various applied biases, V and T=4.2 K. N is the LL index. (b) Plot of $-d^2R/dB^2$ versus B at V=0.1 V. (c) Magnetic field dependence of the critical electric field for NDC, F_C. The line is a guide to the eye. Inset: Plot of N versus $1/B$ for F_C (circles) and for the magnetoresistance in $GaAs_{1-x}N_x$ (x=0.1%) (squares). The line is a linear fit to the data.

Since the amplitude, ΔR, of the MPR oscillations in the magnetoresistance $R(B)$ can be as large as 10% of $R(B)$ at high $B_{\|}$, we deduce that the resonant magnetophonon scattering process can modulate the total scattering rate by an amount $\Delta r_i \sim 0.1 r_v \approx 0.1 \times 10^{13}$ s^{-1}, which is 25% of the typical LO phonon scattering rate $r_i = 0.4 \times 10^{13}$ s^{-1} measured in pure GaAs at B=0 T [77]. Using Eq. 4.3, the average scattering rate at $B = 0$ T is calculated, i.e. $r = 0.6 \times 10^{13}$ s^{-1}. Figure 5.7(c) shows the B-dependence of r derived from the B-dependence of F_C and the estimate of r at B=0 T. The data and analysis indicate that at B=0 T the characteristic time of ballistic acceleration of the electrons to the inflection point k_i in $\varepsilon(k)$ is $\widetilde{\tau} \approx r^{-1} = 0.2 \times 10^{-12}$ s, thus indicating that the mechanism giving rise to NDC in $GaAs_{1-x}N_x$ is a fast process corresponding to the THz frequency range. Chapter 6 provides experimental evidence for this estimate of τ.

5.3 Magnetic field tuning of hot electron capture

In this section we focus on the $B_{\perp}$ configuration. It is shown that when the ratio of electric and magnetic fields reaches a critical value, the trajectory of conduction electrons becomes fully localised in real space. This results in a NDC and current instabilities tuneable by magnetic field.

For this study, sample VN456 (see Table 2.1) was used and for all measurements the device was illuminated with near-infrared radiation from a light-emitting diode (LED) source and power density smaller than 100 Wm^{-2}. The illumination helps to photoionise deep levels [50], which otherwise can cause a resistive and unstable electrical behaviour (see Section 4.1.5).

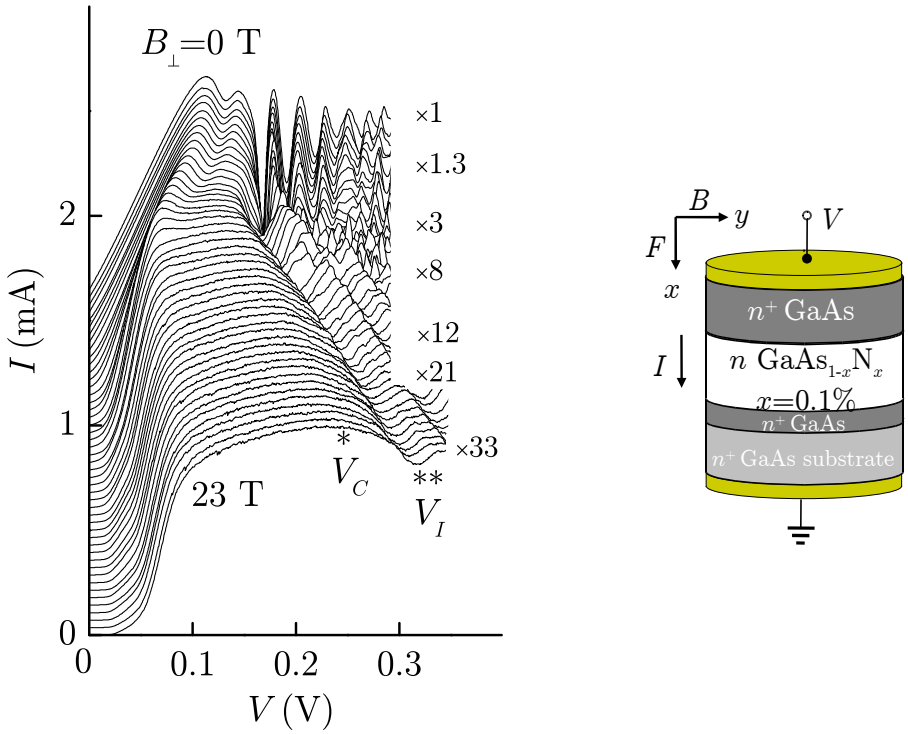

FIGURE 5.8: $I(V)$ characteristics at different B in crossed field configuration (**B** $\perp$ **F**) and at T=4.2 K. For clarity, the curves are displaced along the vertical axis and normalised to the maximum current. The asterisks mark the threshold voltage for NDC (V_C) and the onset of current instabilities (V_I). The inset on the right shows schematic of the $GaAs_{1-x}N_x$ diode and directions of applied **F** and **B**.

Figure 5.8 shows the low-temperature (T=4.2 K) $I(V)$ characteristics of the device at different $B_\perp$. The magnetic field tends to suppress the current at low-bias voltages below a critical threshold value. At higher bias, the quenching of the current by the magnetic field is weaker. We also observe that the NDC region broadens and shifts to higher bias with increasing $B_\perp$. The data points in Fig. 5.11(a) show the B-dependence of the critical field $F_C(B)$ for NDC. These observations differ from those made in the $B_\parallel$ geometry in which the effect of B on the current and NDC is much weaker (see Section 5.2 and Fig. 5.6).

The B-dependence of the NDC in $GaAs_{1-x}N_x$ also differs from that found in other material systems with NDC such as semiconductor superlattices [78, 79]. In a superlattice, a magnetic field applied in the crossed field geometry leads to

a crossing of the $I(V)$ curves, i.e., it induces a decrease of I (negative magnetoresistance) at low F and an increase of I (positive magnetoresistance) at high F. This crossing is absent in the $I(V)$ curves of $GaAs_{1-x}N_x$ in which a positive magnetoresistance is observed at all values of F and $B_\perp$.

The $I(V)$ curves are modeled using a semiclassical description of the electron dynamics and an energy-momentum $\varepsilon(\mathbf{p})$ dispersion relation for the conduction electrons given by the two-level BAC model (see the inset of Fig. 5.9(a)). The form of the $\varepsilon(\mathbf{p})$ curve shows an inflection point occurring at p_0 corresponding to a peak in the electron group velocity $\mathbf{v} = \nabla_p \varepsilon(\mathbf{p}) = (v_x, v_y, v_z)$. In the crossed field geometry, the electron momentum $\mathbf{p}$ obeys the relation $\dot{\mathbf{p}} = -e[\mathbf{F} + \nabla_p \varepsilon(\mathbf{p}) \times \mathbf{B}]$, where e is the electronic charge. Without loss of generality $\mathbf{F}$ and $\mathbf{B}$ are set parallel to x and y axis, respectively (see inset in Fig. 5.8).

The mean drift velocity $\bar{v}_x$ is derived from the solution of the Boltzmann kinetic equation using the relaxation time approximation for the collisional integral. This is equivalent to express $\bar{v}_x$ as the path integral $\bar{v}_x = \tau^{-1} \int_0^\infty v_x(t) \mathrm{e}^{-t/\tau}\, dt$, where τ is the average relaxation time of the electron distribution function[2]. For full derivation of time evolution of electron motion in real and phase space, see Appendix B.

Figure 5.9(a) shows the calculated dependence of the normalised drift velocity $\bar{v}_x/v_0$ on the dimensionless parameter $\omega_F\tau = e\tau F/p_0$ for different values of $\omega_C\tau$. Here, v_0 is the electron group velocity at $|\mathbf{p}| = p = p_0$, $\omega_C = eB/m^*$ is the cyclotron frequency, and $m^* = p/(\partial\varepsilon/\partial p)$ is the electron cyclotron mass at $p = 0$. For $B = 0$ T, the velocity increases monotonically with increasing electric field up to a critical value $F_C = 0.75p_0/(e\tau)$, which corresponds to $\omega_F\tau \approx 1$. For $\omega_F\tau > 1$,

[2]At low (T=4.2 K) temperature, at which our experiment is carried out, we neglect the thermal energy of electrons which is always smaller than the energy width Δ (=0.17 eV) of the CB of $GaAs_{1-x}N_x$ (x=0.1 %).

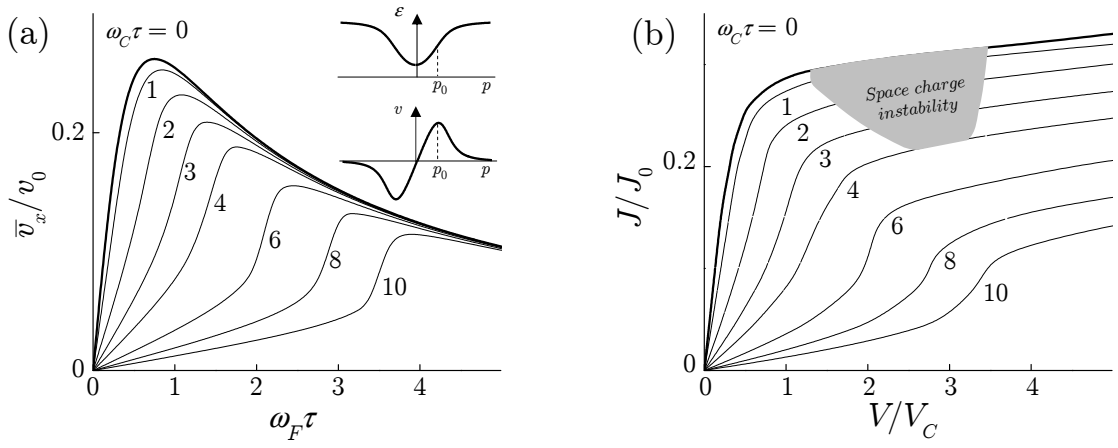

FIGURE 5.9: (a) Calculated dependence of the normalised drift velocity $\bar{v}_x/v_0$ on $\omega_F\tau$ for different values of $\omega_C\tau$. Inset: $\varepsilon(p)$ and $v(p)$ curves used in this model. (b) Calculated dependence of J/J_0 on V/V_C for different values of $\omega_C\tau$. The shadowed area indicates the bias region of current instability in the $I(V)$ characteristics.

τ is larger than the time required for a ballistic electron to reach the inflection point p_0 in $\varepsilon(p)$. Hence, the momentum of the conduction electrons approaches a range of values of $|\mathbf{p}|$ ($|\mathbf{p}| > p_0$), in which the group velocity v decreases with increasing p, thus leading to a negative differential velocity region in the $\bar{v}_x(\omega_F\tau)$ curve. An applied magnetic field reduces the drift velocity and shifts the peak in $\bar{v}_x(\omega_F\tau)$ to higher electric fields.

The striking change of the $\bar{v}_x(\omega_F\tau)$ curves in magnetic field can be understood by considering the electron trajectories in momentum space. As shown in Fig. 5.10(a), for small applied electric field, i.e., $\omega_F/\omega_C < 0.36$, the components of the electron momentum along x and z remain smaller than p_0 and the electron trajectories are closed orbits. For ballistic electrons, the time-averaged value of v_x is zero and electrons drift along z with velocity $v_z = F/B$ (Figs. 5.10(b) and 5.10(c)). A drift of electrons along x can only occur due to elastic and inelastic scattering processes in which the cyclotron orbit centre in the x direction changes as a result of scattering. In contrast, for large electric fields $\omega_F/\omega_C \geq 0.36$, an

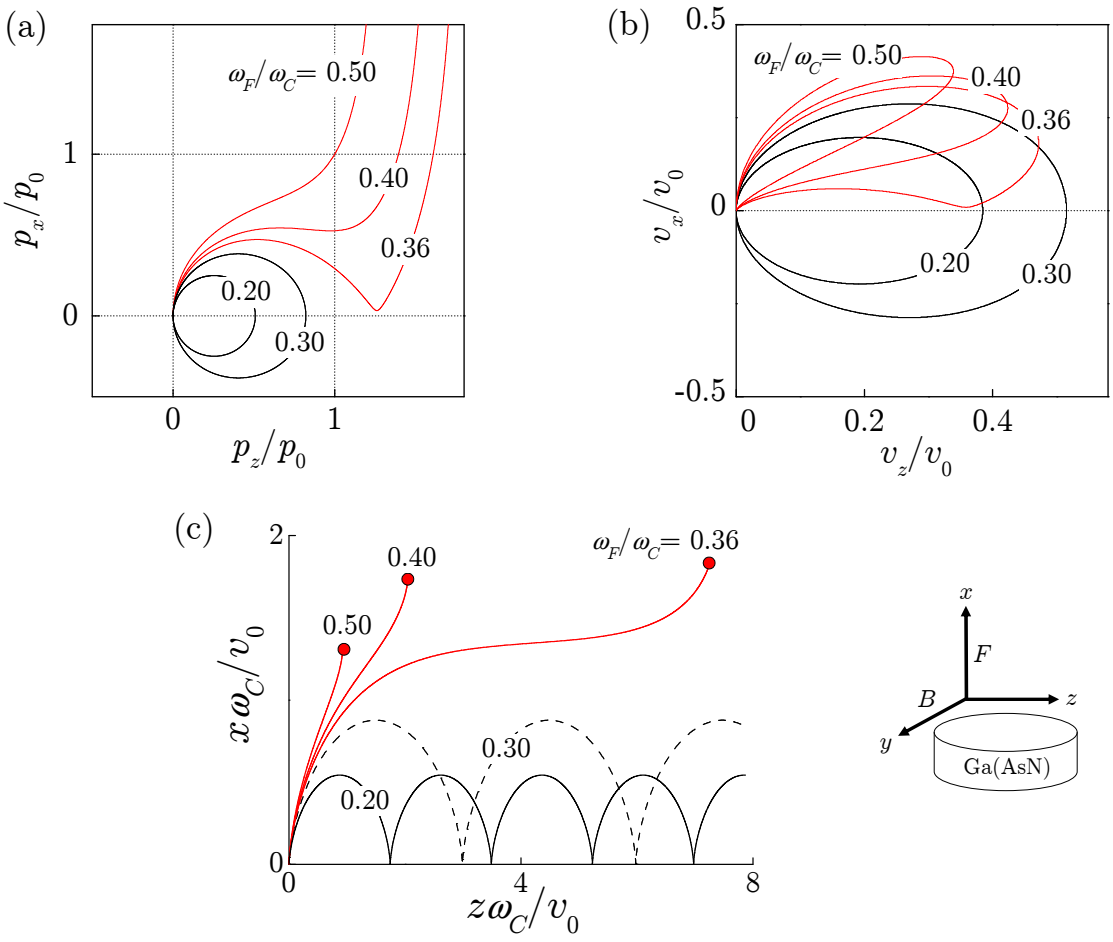

FIGURE 5.10: Electron trajectories in momentum (a), velocity (b) and real (c) space for different values of ω_F/ω_C. The dots in part (c) indicate the points in real space at which the electron comes to rest. Inset: Crossed field configuration.

electron can be accelerated to $|p_x| \geq p_0$. The semiclassical electron trajectory in momentum space is an open orbit (Fig. 5.10(a)), the time-averaged value of v_x is finite even in the absence of scattering (Fig. 5.10(b)) and the electron comes to rest in real space (Fig. 5.10(c)). Therefore, electric and magnetic fields applied in the crossed geometry lead to two distinct regimes of electron dynamics. For low electric fields, the electron dynamics is driven by magnetic field and the drift velocity is strongly quenched by $B_\perp$. For high electric field, the electron localisation by the N-atoms dominates over cyclotron motion and leads to a weaker

B-dependence of $\bar{v}_x$ (Fig. 5.9(a)).

The calculated shift of the $\bar{v}_x(\omega_F\tau)$ curve to higher F with increasing $B_\perp$ shown in Fig. 5.9(a) is in qualitative agreement with the shift of the measured $I(V)$ characteristics. The measured B-dependence of the threshold electric field $F_C(B)$ for NDC is compared in Fig. 5.11(a) with the calculated peak position of the $\bar{v}_x(\omega_F\tau)$ curve at various $B_\perp$. We obtain the best fit to the experimental data by setting $F_C = 1.6$ kVcm^{-1} at B=0 T and the low-field mobility $\mu = e\tau/m^* = (0.20 \pm 0.05)$ m^{2}V^{-1}s^{-1}. This value of μ agrees with that obtained from independent Hall measurements on our modulation-doped $GaAs_{1-x}N_x$ quantum wells with x=0.1% ($\mu = 0.20$ m^{2}V^{-1}s^{-1} at T=4.2 K) [51] and with that reported by other groups on similar structures [55, 68]. This estimate of mobility is also in agreement with the estimate presented in Chapter 4 (Section 4.1.1).

The measured $I(V)$ curves indicate that the magnetic field modifies the voltage position and amplitude of the current oscillations in the NDC region (Fig. 5.8). These effects and the overall form of the $I(V)$ curves can be explained by considering two contributions to the electronic conduction: the first is due to the "background" free-electron density n_0 in the $GaAs_{1-x}N_x$ layer at $V = 0$ V; the second contribution is the mobile space charge arising from the additional electrons, density n_s, injected into the $GaAs_{1-x}N_x$ from the negatively biased n^+ GaAs-emitter layer. In a similar manner to the earlier fit of $I(V)$ curves at $B = 0$ T (Section 4.1.1), we calculate the current density by solving the equation for the drift current

$$J = (n_0 + n_s)e\bar{v}_x \tag{5.10}$$

and Poisson's equation

$$\partial F/\partial x = en_s/\varepsilon, \tag{5.11}$$

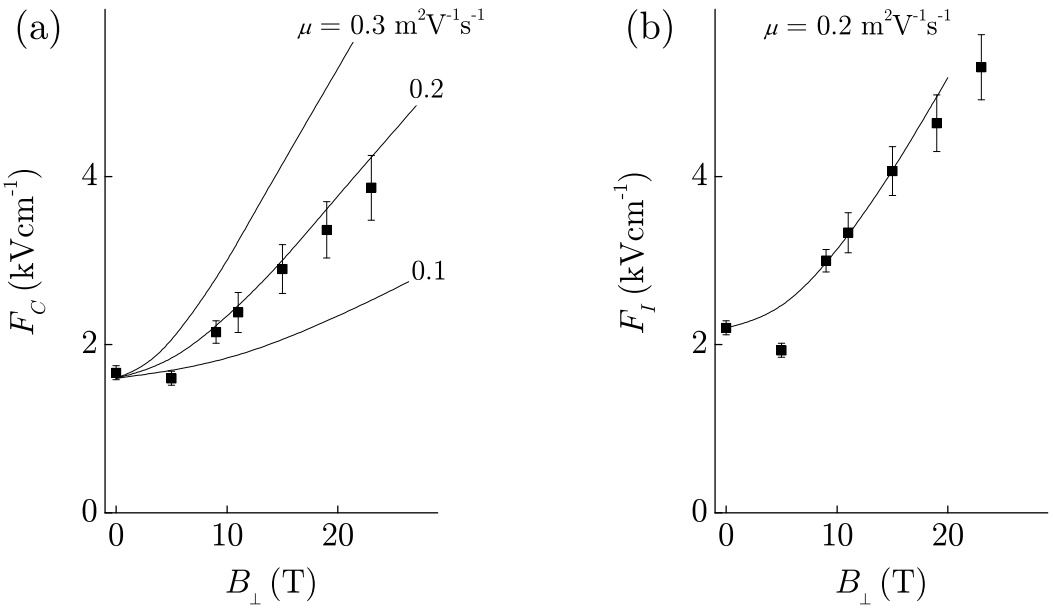

FIGURE 5.11: (a) B-dependence of the measured (full squares) and calculated (lines) positions of the critical electric field F_C for NDC, T=4.2 K. (b) B-dependence of the measured (full squares) and calculated (line) positions of the threshold electric field F_I for current instability, T=4.2 K. The continuous lines in parts (a) and (b) correspond to the calculated values of F_C and F_I for (a) μ=0.1, 0.2 and 0.3 m^{2}V^{-1}s^{-1} and (b) μ=0.2 m^{2}V^{-1}s^{-1}.

where ε is the dielectric permittivity of the lattice (see Appendix A). Figure 5.9(b) shows the calculated dependence of the normalised current density J/J_0 on V/V_C for different values of $\omega_C\tau$. Here, $J_0 = n_0 e v_0$ and $V_C = F_C L$ is the threshold voltage for NDV at B=0 T. The best fit to the measured $I(V)$ curve at B=0 T is obtained by setting F_C = 1.6 kVcm^{-1} at B=0 T, $\mu = e\tau/m^*$ = 0.20 m^{2}V^{-1}s^{-1}, and n_0 = 2×10^{21} m^{-3}. Using these parameters and the criterion for domains formation[3], we find that a space charge instability occurs for electric fields larger than a threshold

[3]For a semiconductor with NDV, the criterion for domain formation can be expressed as $L/(\bar{v}_x\tau_d) \geq 2.09$ [80]. Here, $\tau_d = \varepsilon/(en_0|\mu_d|)$ is the dielectric relaxation time, $\mu_d = d\bar{v}_x/dF$ is the differential mobility, ε is the dielectric permittivity, and n_0 is the "background" free-electron density. Using the functional form of $\bar{v}_x(\omega_F\tau)$ at various $B_\perp$, we estimate that a space charge instability occurs for $n_0/\tilde{n} \geq 2.09R(a)/R'(a)$, where $\tilde{n} = \varepsilon F_C/eL$ is the characteristic space charge density at the critical field F_C and B=0 T, $a = \omega_F\tau$, and $R(a) = \bar{v}_x/v_0$.

value F_I which depends on $\omega_C\tau$, and that it is suppressed for $\omega_C\tau > 4$ (i.e., $B_\perp > 20$ T). As shown in Fig. 5.11(b), the calculated value of F_I shifts to higher values in agreement with the measured onset of current instability in the $I(V)$ curves. This effect can be explained qualitatively as follows. With increasing $B_\perp$, the critical field $F_C(B)$ for NDC shifts to higher values. This increases the contribution of space charge to the current in the NDC region, thus increasing the electric field required to establish the instability in the current. Therefore, an applied magnetic field provides an effective way of suppressing current instabilities associated to NDC in $GaAs_{1-x}N_x$.

Chapter 6

High-frequency electron dynamics in $GaAs_{1-x}N_x$

In this chapter we describe the *ac* electron dynamics in $GaAs_{1-x}N_x$ by measuring harmonic generation of *ac* current and the change in the *dc* conductivity in the presence of an external THz electromagnetic radiation. We demonstrate that in the bias region of NDC, the electrical current can be modulated by an *ac* field of frequency 0.4 THz. This opens up interesting prospects of exploiting the NDC in $GaAs_{1-x}N_x$ in THz electronics.

6.1 The "THz gap"

The region of the electromagnetic spectrum between 0.3 and 10 THz is often referred to as the "THz gap" (see Fig. 6.1) as the THz frequencies fall between frequencies commonly covered by conventional electronic and optical sources of electromagnetic radiation. Historically, little study of the interactions between

radiation and matter at these frequencies has been undertaken because of the difficulty in generating and detecting THz radiation. The need to fill this technology gap with appropriate devices has stimulated research on fast electron dynamics in a wide variety of material systems. Recent studies include Bloch oscillations in artificial superlattices [81, 82], phonon-assisted inter-miniband transitions in quantum cascade lasers [83], current instabilities in nanoscale transistors [84] and ballistic devices [85], and fast carrier dynamics in graphite [86] and carbon-nanotubes [87]. In the next section we show that dilute nitride $GaAs_{1-x}N_x$ is a potential candidate for developing a new types of sources and detectors of THz radiation.

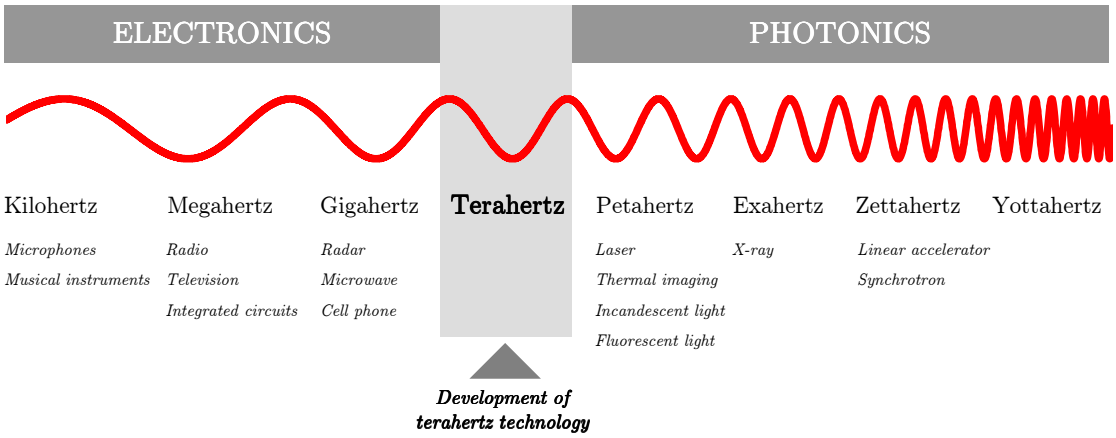

FIGURE 6.1: The electromagnetic spectrum with the terahertz gap highlighted.

6.2 $GaAs_{1-x}N_x$ as detector of high-frequency radiation

In Chapter 5 (see Sec. 5.2) it was demonstrated that the magnetophonon modulation of the critical electric field for NDC in $GaAs_{1-x}N_x$ provides a means of probing the timescales of the processes responsible for NDC. The estimated times,

less than a picosecond, imply a high-frequency response of the current in the THz range. To experimentally probe this fast dynamics, we use a high-frequency detection experiment in which we measure the change in the *dc* conductivity in the presence of an external THz radiation.

In this experiment we use a n^+-n-n^+ $GaAs_{1-x}N_x$ diode (sample VN456) and the experimental setup is shown in Fig. 2.6. An external *dc* bias is applied to the diode and the sample is irradiated with THz electromagnetic radiation from a BWO (frequency, f, up to 0.7 THz). Whilst sweeping the *dc* bias, the THz-induced *dc* current is measured using a phase sensitive lock-in technique. A chopping modulation technique is also used to separate the THz-induced *dc* current from the *dc*-bias component.

Figure 6.2 shows the *dc* $I(V)$ characteristic (left scale) and THz-induced *dc* current, ΔI_{THz}, (right scale) for sample VN456 at T=50 K when excited with THz electromagnetic radiation of frequency f=0.1 THz. We note two main effects. First, the THz-induced *dc* current is largest at biases corresponding to a more pronounced region of non-linerity in the $I(V)$; Second, the sign of ΔI_{THz} is negative.

The photo-induced current is strongly affected by temperature. Figure 6.3(a) shows the bias dependence of the average *dc* current ΔI_{THz} in the T-range 20 - 70 K. For T <40 K and small applied *dc* bias voltages (V <0.4 V), ΔI_{THz} is weak and positive while increasing T above 40 K leads to the change in the sign and amplitude of ΔI_{THz}. In Fig. 6.3(a) we also plot the bias dependence of the second derivative of the *dc* current d^2I/dV^2. The $\Delta I_{THz}(V)$ curve resembles the bias dependence of d^2I/dV^2 for T >40 K (Fig. 6.3(b)), thus suggesting that at these temperatures the diode behaves like a classical rectifier, i.e., the current in the diode follows instantaneously the time-dependent high-frequency radiation

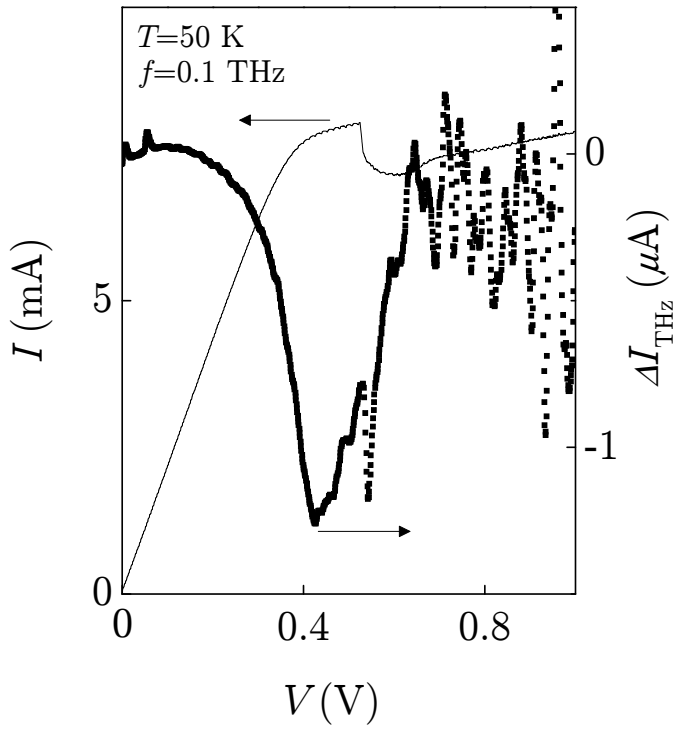

FIGURE 6.2: $I(V)$ characteristic (left scale) and THz-induced *dc* current, ΔI_{THz}, (right scale) for sample VN456 at T=50 K.

according to the form of the *dc* $I(V)$ curve [88]. The correspondence between d^2I/dV^2 and ΔI_{THz} is observed for T up to 80 K and over a wide range of frequencies up to a maximum value of 0.4 THz, above which the photoconductivity decreases, making impossible reliable low-noise measurements of the photocurrent signal. The high-frequency operation of our diodes is limited by the RC time, $\tau_{RC} = RC = 2 \times 10^{-12}$ s, where R=40 Ω is the diode low-bias resistance, $C = \varepsilon_r \varepsilon_0 A/L = 6 \times 10^{-14}$ F is the capacitance, ε_r=13 is the relative static permittivity, ε_0 is the permittivity of free space, L is the thickness of the $GaAs_{1-x}N_x$ layer and A is the area of the diode.

The rectification effect indicates that for T >40 K the mechanism giving rise to NDC is a fast ($\sim 10^{-12}$ s) process. This fast response time is consistent with recent calculations of the *ac* electron dynamics in $GaAs_{1-x}N_x$ predicting that the

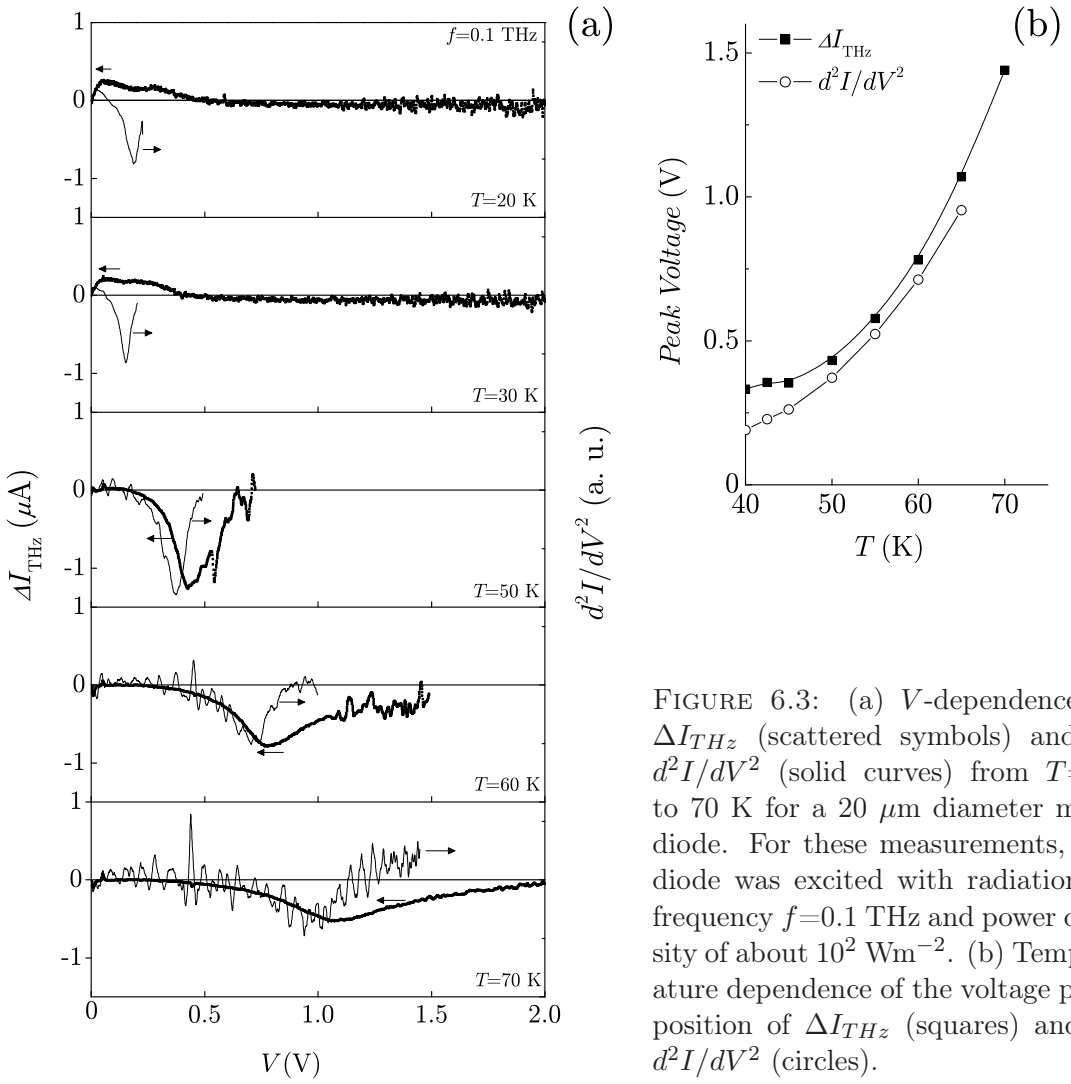

FIGURE 6.3: (a) V-dependence of ΔI_{THz} (scattered symbols) and of d^2I/dV^2 (solid curves) from T=20 to 70 K for a 20 μm diameter mesa diode. For these measurements, the diode was excited with radiation of frequency f=0.1 THz and power density of about 10^2 Wm^{-2}. (b) Temperature dependence of the voltage peak position of ΔI_{THz} (squares) and of d^2I/dV^2 (circles).

maximum response frequency f_{max} associated with the NDC is governed by the time of ballistic acceleration of electrons to the N-level and that this lies in the terahertz frequency range [7].

The small and positive value of ΔI_{THz} at T <40 K agrees with our previous analysis in Section 4.1.5 revealing that at low temperature (4-40 K), the high-electric-field dynamics in $GaAs_{1-x}N_x$ is slow. Above a critical electric field of 2 kVcm^{-1} very slow (< 1 Hz) frequency current oscillations are observed due to a field-enhanced trapping of electrons at localised states (see Fig. 4.4(b)). The positive sign of ΔI_{THz} at T <40 K suggests that the current is enhanced through

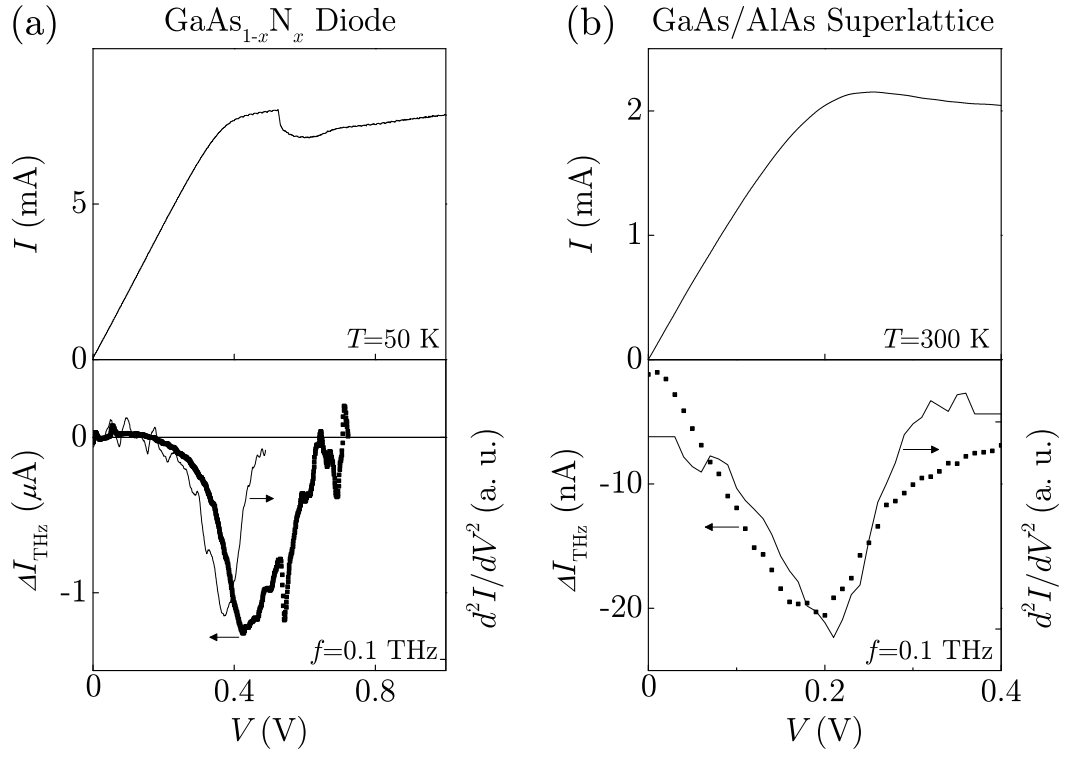

FIGURE 6.4: Top: $I(V)$ characteristics for (a) a $GaAs_{1-x}N_x$ diode (sample VN456, T=50 K) and (b) a GaAs/AlAs superlattice (T=300 K). Bottom: Bias dependence of the THz-induced *dc* current, ΔI_{THz}, for (a) a $GaAs_{1-x}N_x$ diode and (b) a GaAs/AlAs SL [89]. The right hand scale in parts (a) and (b) show the second derivatives of the *dc* current, I.

ionisation of these electron traps by the terahertz radiation. At higher temperatures ($T > 40$ K), however, electrons frozen onto these localised states are released by thermal excitation into the CB thus leading to a fast dynamics.

In order to reduce the time constant of the diode, thus improving the high-frequency operation, we studied low-capacitance planar diodes based on n-doped $GaAs_{1-x}N_x$ epilayers (samples B). However, the $I(V)$ characteristic of these devices were not stable at low temperatures and did not allow us to test the THz response as done for conventional diodes. Figure 6.5 shows two photographs of the surface of low-capacitance planar diode, taken before and after cooling. The

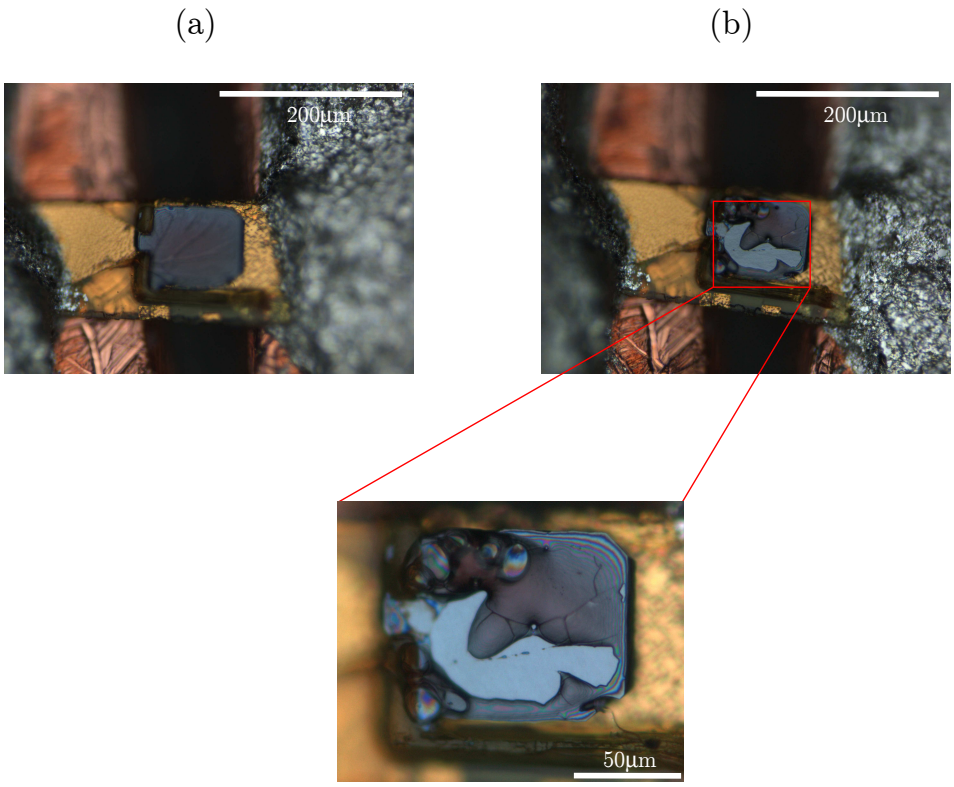

FIGURE 6.5: Photographs of the surface of low-capacitance planar diode before (a) and after (b) cooling down the sample to T=4.2K. The smooth and flat semiconductor surface of the device develops several cracks after cooling, see magnified picture of the wafer.

cracks developed on the sample surface after several cycles of cooling indicate a possible processing problem and can be attributed to the thinness (∼8 μm) of these devices. Further experiments on improved devices are required to clarify what is the maximum frequency that can be detected by using $GaAs_{1-x}N_x$.

The high-frequency detection experiment was performed in number of diodes with non-linear $I(V)$ characteristics. Figure 6.4 shows a comparison between the results of high-frequency detection experiments in two different systems exhibiting non-linear $I(V)$ curves, i.e. a $GaAs_{1-x}N_x$ diode (sample VN456) and a GaAs/AlAs superlattice (SL) [89]. Although, the THz-induced response in both systems obeys the same classical rectification theory [88] (note the close resemblance between ΔI_{THz} and d^2I/dV^2 in Fig. 6.4), the origin of the photo-induced

current is different. The SL THz-frequency response was discussed in a number of works [90, 91, 92] and associated with Bloch oscillations and dynamical localisation of electrons [93]. In the case of dilute nitride $GaAs_{1-x}N_x$, it arises from the interaction of the conduction electrons with resonant N-levels in the CB.

6.3 $GaAs_{1-x}N_x$ as frequency multiplier

To confirm the results from the high-frequency detection studies, we carried out complementary experiments in which we used the non-linear characteristics of our diode for frequency multiplication and mixing using superheterodyne detection methods (see Section 2.3.1).

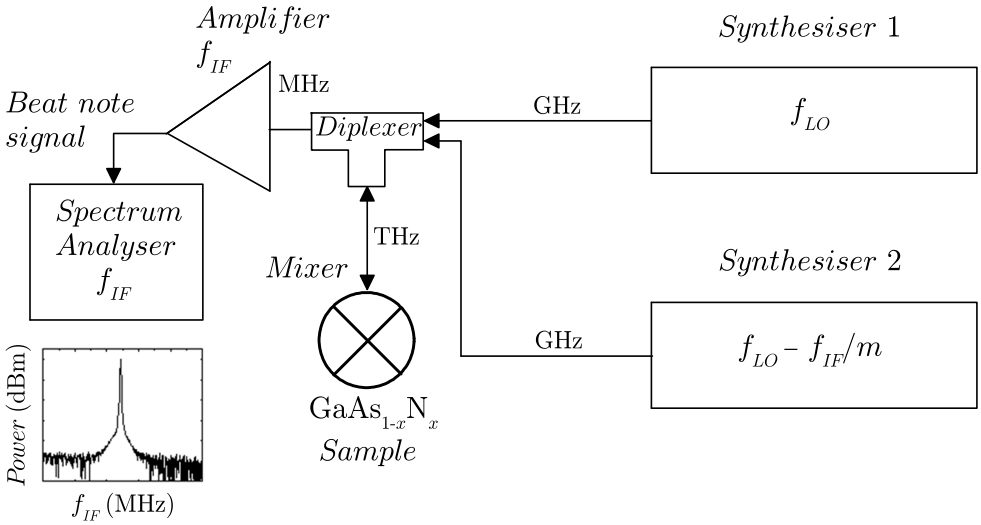

FIGURE 6.6: Schematic of the heterodyne method in which a $GaAs_{1-x}N_x$ diode is used as a frequency multiplier.

Figure 6.6 shows the block diagram of the experimental setup for frequency multiplication. In the experiment, the diode (VN456), kept at T=77 K, was driven

by two *ac* signals from two identical high-frequency generators (synthesisers) with well-defined frequencies in the 1 - 20 GHz range. The frequencies of the two signals were set to f_{LO} and $f_{LO} - f_{IF}/m$, respectively (f_{LO}=7 GHz, f_{IF}=100 MHz, m being a positive integer and represents the harmonic number). The beating between these two signals led to harmonic generation of *ac* current. If the spectrum analyser, set at the central frequency f_{IF}, detects a signal, it is an indication of the sample's ability to generate m^{th} harmonic of *ac* signal with frequency f_{LO}.

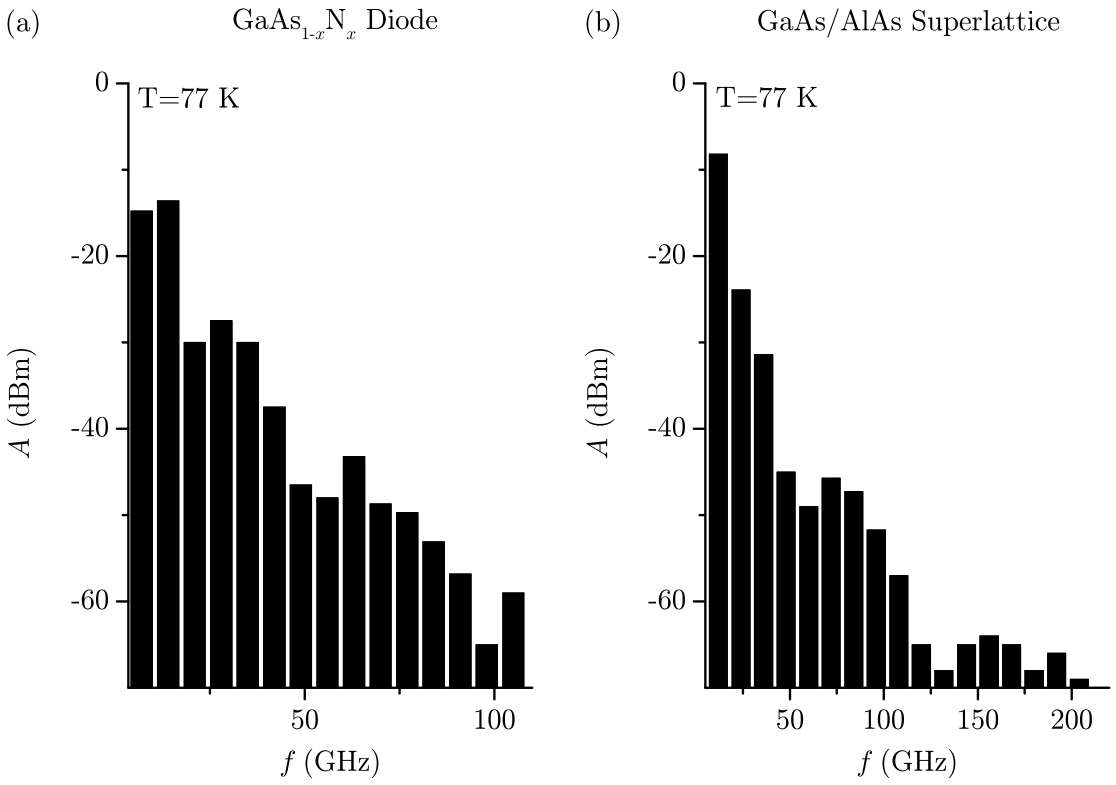

FIGURE 6.7: Frequency dependence of the amplitude, A, of the beat note signal for a $GaAs_{1-x}N_x$ diode (a) and for a GaAs/AlAs SL (b) at T=77 K.

The experimental results are plotted in Fig. 6.7. For comparison purposes, we plot the results for the $GaAs_{1-x}N_x$ diode (part (a)) and for a GaAs/AlAs SL (part (b)). Using this heterodyne method, we were able to observe harmonic

generation of *ac* current with frequency up to 100 GHz ($m = 15$, $f_{LO} = 7GHz$) for the $GaAs_{1-x}N_x$ diode and up to 150 ($m = 15$, $f_{LO} = 12GHz$) GHz for the GaAs/AlAs SL. The ability of frequency multiplication suggests a fast electron dynamics in both systems.

6.4 $GaAs_{1-x}N_x$ and THz electronics

The fast non-linear dynamics revealed by our experiments in $GaAs_{1-x}N_x$ arises from carrier trapping into the N-localised states (hot electrons) followed by fast energy relaxation by phonons thus leading to free electrons (cold electrons). Therefore in order to observe this effect, two processes are necessary: carrier localisation at high electric fields and efficient phonon scattering. These two requirements impose a limitation on the temperature required to observe this unusual type of fast non-linear dynamics. An increasing T tends to decrease the number of localised states due to thermal ionisation, but it increases the probability of inelastic scattering. Our experiments suggest an optimal temperature range of 50-60 K.

The ability of conduction electrons in $GaAs_{1-x}N_x$ to respond almost instantaneously to the high-frequency electromagnetic field suggests possible device applications in THz electronics. Despite some technological limitations, such as the relatively low temperatures of operation, the fast electron dynamics in $GaAs_{1-x}N_x$ could lead to exciting developments in the field of THz electronics. On the one hand, $GaAs_{1-x}N_x$ and other dilute nitride alloys could lead to a novel type of THz detection (see Section 6.2). On the other hand, they could provide media for signal amplification and novel solid-state emitters in the THz/sub-THz frequency range. Further experiments utilising diodes optimised for THz operation will be needed to assess the use of dilute nitrides in THz electronics.

Chapter 7

Conclusion and future directions

The aim of this thesis was to study the non-linear electron dynamics in the dilute nitride $GaAs_{1-x}N_x$ alloy system. The study of the effect of high magnetic fields on the electrical conductivity of devices based on $GaAs_{1-x}N_x$ has provided useful information about the remarkable electron dynamics of these novel materials. Our studies revealed a new type of negative differential velocity (NDV) effect, which arises when electrons are accelerated by a large electric field ($>$ 1kV/cm) in the highly non-parabolic energy dispersion of $GaAs_{1-x}N_x$. We have modeled the measured NDV effect using a semiclassical description of the electron dynamics and the energy-wavevector dispersion relation for the conduction electrons given by the two-level band anticrossing (BAC) model. The good agreement between our data and the theoretical calculations justified the use of a two-level BAC model when describing the electronic properties of dilute nitrides at low x ($\sim$0.1 %).

To assess the feasibility of using $GaAs_{1-x}N_x$ in electronic devices, we investigated the magneto-transport properties of a series of n-doped $GaAs_{1-x}N_x$ epilayers with x up to 1 %. Transport measurements on Hall bars revealed a

strong dependence of the electron mobility, μ, on the N-concentration. As the mobility depends on elastic and inelastic scattering processes, these measurements provided a means of assessing the disorder induced by N in the host GaAs crystal. We have established that in the ultra-dilute alloy regime, $x \sim 0.1$ %, the N-related defects play a minor role in the electronic conduction. The measured value of μ in this regime is $\mu \sim 0.2\ m^2\mathrm{V}^{-1}\mathrm{s}^{-1}$ and is relatively insensitive to temperature. In the presence of large quantising magnetic fields we have achieved values of $\mu B \gg 1$, which were sufficient to observe clear Landau Level (LL) quantisation and a strong magnetophonon resonance (MPR) effect. The MPR data revealed a significant N-induced enhancement of the electron effective mass and of Si-binding energy in $GaAs_{1-x}N_x$.

In the configuration in which the electric and magnetic field are parallel, we have observed a remarkable modulation of the onset for negative differential conductance (NDC) versus magnetic field. This provided us with a novel means of probing the scattering rates and the time-scales of the processes governing the NDC in $GaAs_{1-x}N_x$. The magneto-transport experiments revealed that the acceleration of electrons towards the energy of the N-level is a fast process, less than a picosecond, of relevance for THz applications. In order to probe directly the time-scales involved in the electron dynamics, we have performed a series of high-frequency experiments in which we used $GaAs_{1-x}N_x$ either as detector of THz radiation or as a frequency multiplier. The results clearly revealed the ability of the conduction electrons in $GaAs_{1-x}N_x$ to follow instantaneously the externally applied THz electromagnetic field. This opens up prospects for the development of novel detectors/emitters of THz radiation of relevance for a wide range of applications.

The results presented in this thesis represent the first steps towards implementation of the NDC effect in $GaAs_{1-x}N_x$ in real devices. Some technological limitations, such as the low operating temperature (T ~40 K), weak coupling to the external THz radiation and relatively low cut-off frequency (~0.1 THz) could be overcome by implementing $GaAs_{1-x}N_x$ in low-barrier Schottky diodes design or small planar diodes as done for conventional high-frequency devices [43, 94]. This could increase the coupling efficiency of the device to the external high-frequency electromagnetic field and improve the dissipation of heat at room temperature.

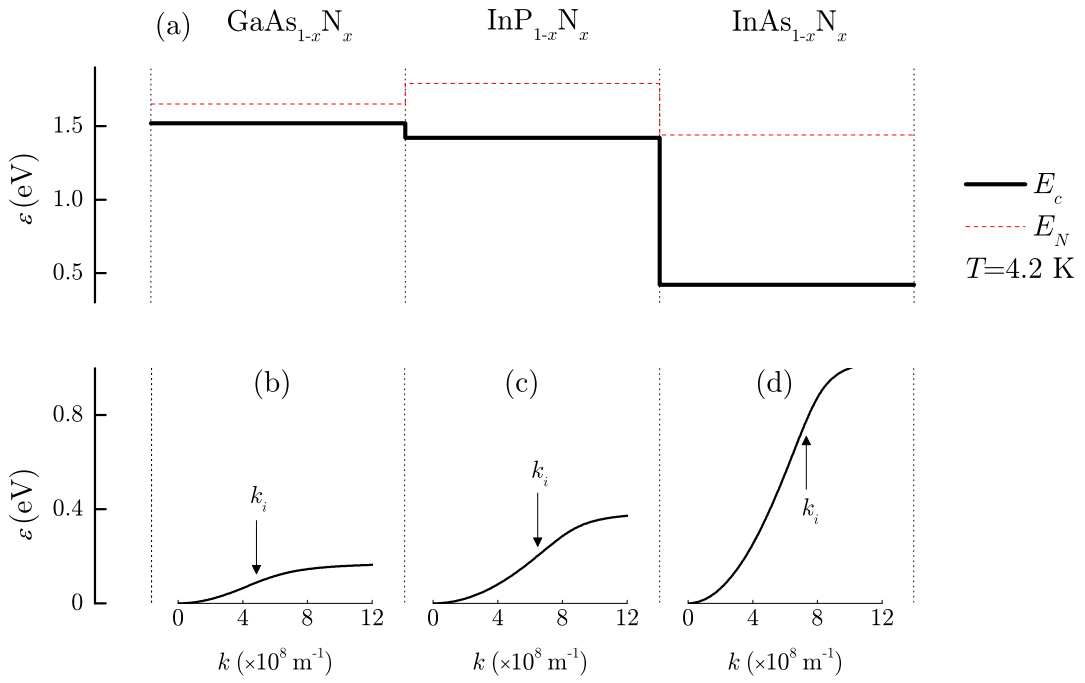

FIGURE 7.1: (a) N-level position (E_N) and energy of the CBE (E_c) for $GaAs_{1-x}N_x$, $InP_{1-x}N_x$ and $InAs_{1-x}N_x$, taken from Ref.[32] for x=0.1 %. Values are relative to the top of the VB. (b-d) $\varepsilon(k)$ curves of the $\mathbf{\Gamma}$-CB for the three dilute nitride alloys according to a two-level BAC model with x=0.1 %. The arrow indicates the inflection point, k_i, of $\varepsilon(k)$.

Other III-N-V systems, such as $InP_{1-x}N_x$ and $InAs_{1-x}N_x$, could also be exploited to observe the NDC effect. In these compounds, the nature of the resonant localisation of electrons due to the N is still unexplored territory. However, it is

clear that the different energy position of the N-level relative to the conduction band edge (CBE) will offer new degrees of freedom in the design of the energy dispersion and corresponding electron peak velocities. Figure 7.1(a) depicts the N-level position relative to the CBE for three dilute nitride alloys - $GaAs_{1-x}N_x$, $InP_{1-x}N_x$ and $InAs_{1-x}N_x$. The values of E_c and E_N are taken from Ref.[32] for x=0.1 % and are measured relative to the top of the VB. Figure 7.1(b-d) shows the corresponding energy dispersion $\varepsilon(k)$ curves of the **Γ**-CB for the three dilute nitride alloys according to a two-level BAC model with x=0.1 %. For emphasis of particular interest is the very high electron peak velocity that showed occur in $InAs_{1-x}N_x$.

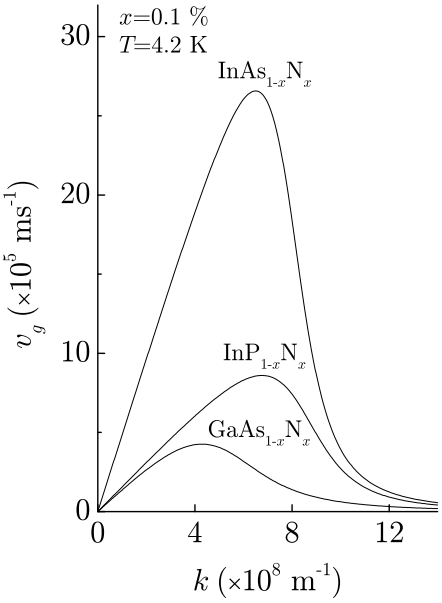

FIGURE 7.2: k-dependence of the group velocity, v_g, for dilute nitrides with x=0.1 %.

Because of the very high curvature (i.e. small effective mass) of the **Γ**-CB in InAs, the anticrossing effect is expected to occur at high electron energies, but relatively low values of k-vector. Therefore, it should be possible to achieve peak velocities in $InAs_{1-x}N_x$ of $\sim 3\times10^6$ ms^{-1} (Fig. 7.2), an order of magnitude higher than those in $GaAs_{1-x}N_x$, but with similar easily achievable values of the applied

electric field. In conclusion, these are exciting prospects for future studies of the electronic properties of dilute nitrides and their exploitation in novel electronic devices.

Appendix A

Space-Charge-Limited Currents

To model the $I(V)$ curve taking into account space charge effects, first we consider the continuity equation[1]:

$$J = (n_0 + n_s)ev_d, \tag{A.1}$$

where n_0 is the background free-electron concentration and n_s is the concentration of injected carriers. At low fields, $n_0 \gg n_s$ and J can be written as

$$J \approx n_0 ev_d = n_0 e \frac{\mu F}{1 + (F/F_C)^2}, \tag{A.2}$$

where we have used the functional form of $v_d(F)$ derived from a semiclassical model (see Section 1.5.2). At higher fields, however, the charge is non-uniformly distributed across the sample and $n_s \gg n_0$. The current is now dominated by the injected carriers from the cathode, i.e. $J \approx n_s e v_d$. To determine n_s, we use the Poisson's equation

[1]The simplified Space-Charge-Limited Currents model neglects the diffusion contribution to the current. For a discussion of this approximation see Ref.[95].

$$\frac{\partial F(z)}{\partial z} = \frac{en_s}{\varepsilon}, \tag{A.3}$$

where z is the direction of the current flow and ε is the permittivity of GaAs. Using Eq.A.3, we express the current density as:

$$J \approx n_s e v_d = \varepsilon \frac{\partial F(z)}{\partial z} \frac{\mu F(z)}{1 + [F(z)/F_C]^2}. \tag{A.4}$$

By integrating both sides of A.4 we obtain

$$J = \frac{\varepsilon \mu {F_C}^2}{2z} \ln \left\{ 1 + \left[\frac{F(z)}{F_C} \right]^2 \right\}. \tag{A.5}$$

Using Eq.A.5, we can express F as

$$F(z) = F_C \sqrt{\mathrm{e}^{\alpha z} - 1}, \tag{A.6}$$

where

$$\alpha = 2J/\varepsilon \mu {F_C}^2 \tag{A.7}$$

is a constant. We integrate the field across the length L of the device. This allows us to obtain the voltage drop, V, across the sample

$$V = \int_0^L F(z)\, dz = F_C \int_0^L \sqrt{\mathrm{e}^{\alpha z} - 1}\, dz. \tag{A.8}$$

By exchanging the variables, $e^{\alpha z} - 1 = y^2$, the right-hand side integral in A.8 takes the form,

$$\int_0^L \sqrt{e^{\alpha z} - 1}\, dz = \int_0^{\sqrt{e^{\alpha L}-1}} \frac{2y^2}{\alpha(y^2+1)}\, dy, \tag{A.9}$$

which can be solved analytically. Finally using Eqs.A.8 and A.9, we obtain

$$V = \frac{2F_C}{\alpha}\left[\sqrt{e^{\alpha L} - 1} - \arctan\left(\sqrt{e^{\alpha L} - 1}\right)\right]. \tag{A.10}$$

The expression A.10 describes the V-dependence of J in the limit $n_s \gg n_0$.

Appendix B

Electron transport in crossed electric and magnetic *dc* fields

In the presence of electric (F) and magnetic (B) fields, the equation of motion for electrons is given by

$$\hbar\dot{\mathbf{k}} = \mathbf{f}, \tag{B.1}$$

where

$$\mathbf{f} = q[\mathbf{F} + (\mathbf{v} \times \mathbf{B})] \tag{B.2}$$

is the Lorentz force and $\mathbf{k}$ is the wavevector.

Let us assume that the magnetic field is applied along the y-axis perpendicular to the electric field, which is along the x-axis. For a semiconductor with parabolic and isotropic energy dispersion, $\varepsilon(k) = \hbar^2k^2/2m^*$, and Eq.B.2 can be written as

$$m^*\dot{\mathbf{v}} = q[\mathbf{F} + (\mathbf{v} \times \mathbf{B})], \tag{B.3}$$

where m^* is the isotropic electron effective mass given by the relation $m^* = \hbar^2(\partial^2\varepsilon/\partial k^2)^{-1}$. With initial conditions $\mathbf{r}(0) = 0$ and $\mathbf{v}(0) = 0$, the solution of Eq.B.3 gives the time evolution of the electron trajectories along x and z, i.e.

$$x(t) = \frac{F}{\omega_C B}(1 - \cos\omega_C t), \tag{B.4}$$

$$z(t) = \frac{F}{\omega_C B}(\omega_C t - \sin\omega_C t), \tag{B.5}$$

where $\omega_C = eB/m^*$ is the cyclotron frequency. The time-dependence of v_x and v_z is then given by

$$v_x(t) = \frac{F}{B}\sin\omega_C t, \tag{B.6}$$

$$v_z(t) = \frac{F}{B}(1 - \cos\omega_C t). \tag{B.7}$$

The trajectory in the x direction is simple harmonic motion. In the z direction, the electron motion contains both simple harmonic and translational components with drift occurring along z. The electron trajectory in the (x, z) plane is a cycloid. In the phase space, both velocities are harmonic functions of time.

For the case of non-parabolic energy dispersion, Eq.B.2 can only be solved numerically. In the case of $GaAs_{1-x}N_x$, the calculated electron trajectories are shown in Fig. 5.10.

To take into account the scattering in the system, we use a classical kinetic formula [96, 97] and express $v_d(F)$ as follows:

$$v_d(F) = \frac{1}{\tau}\int_0^\infty v_x(t)\mathrm{e}^{-t/\tau}dt, \tag{B.8}$$

where τ is the velocity relaxation time.

Bibliography

[1] P. J. Mohr and B. N. Taylor. CODATA recommended values of the fundamental physical constants: 1998. *J. Phys. Chem. Ref. Data*, 28(6), 1999.

[2] Special issue of. *Semicond. Sci. Technol.*, 17:741–906, 2002.

[3] J. W. Ager and W. Walukiewicz. *Semicond. Sci. Technol.*, 17:741–745, 2002.

[4] J. Wu, W. Shan, and W. Walukiewicz. *Semicond. Sci. Technol.*, 17:860–869, 2002.

[5] S. R. Bank, H. B. Yuen, H. Bae, M. A. Wistey, and J. S. Harris. *Appl. Phys. Lett.*, 88:221115, 2006.

[6] D. J. Friedman and S. R. Kurtz. *Prog. Photovoltaics*, 10(5):331–344, 2002.

[7] A. Ignatov, A. Patanè, O. Makarovsky, and L. Eaves. *Appl. Phys. Lett.*, 88 (032107):3, 2006.

[8] P. J. Klar. *Prog. Solid State Chem.*, 31(4):301–349, 2003.

[9] M. Henini. *Dilute Nitride Semiconductors.* Elsevier, London, 2004.

[10] C. Kittel. *Introduction to Solid State Physics.* John Wiley & Sons, Inc, 8^{th} edition, 2005.

[11] J. R. Hook and H. E. Hall. *Solid State Physics*. John Wiley & Sons, Inc, 2^{nd} edition, 2003.

[12] S. Gasiorowicz. *Quantum Physics*. John Wiley & Sons, Inc, 2^{nd} edition, 1996.

[13] I. Vurgaftman, J. R. Meyer, and L. R. Ram-Mohan. *J. Appl. Phys.*, 89(11): 5815–5875, 2001.

[14] J. S. Blakemore. *Appl. Phys. Lett.*, 53(10):R123–R181, 1982.

[15] P. Kratzer, C. G. Morgan, E. Penev, A. L. Rosa, A. Schindlmayr, L. G. Wang, and T. Zywietz. *FHI98MD Computer code for density-functional theory calculations for poly-atomic systems*. 1999. User's Manual.

[16] J. B. Gunn. Microwave oscillations of current in III-V semiconductors. *Solid State Commun.*, 1:88–91, 1963.

[17] J. B. Gunn. Microwave oscillations of current in III-V semiconductors. *IBM J. Res. Dev.*, 8:141–159, 1964.

[18] B. K. Ridley and T. B. Watkins. The possibility of negative resistance in semiconductors. *Proc. Phys. Soc.*, 78:293–304, 1961.

[19] C. Hilsum. Transferred electron amplifiers and oscillators. *Proc. IRE*, 50: 185–189, 1962.

[20] W. Shan, W. Walukiewicz, J. W. Ager III, E. E. Haller, J. F. Geisz, D. J. Friedman, J. M. Olson, and S. R. Kurtz. *Phys. Rev. Lett.*, 82(6):1221–1224, 1999.

[21] A. Lindsey and E. P. O'Reilly. *Solid State Commun.*, 112:443, 1999.

[22] P. R. C. Kent and A. Zunger. *Phys. Rev. B*, 64:115208, 2001.

[23] Y. Zhang, B. Fluegel, M. C. Hanna, J. F. Geisz, L. W. Wang, and A. Mascarenhas. *Phys. Status Solidi B-Basic Research*, 240(2):396–403, 2003.

[24] L. W. Wang. *Phys. Rev. Lett.*, 88(25), 2002.

[25] Y. Zhang, A. Mascarenhas, H. P. Xin, and C. W. Tu. *Phys. Rev. B*, 61(11): 7479–7482, 2000.

[26] A. Lindsay and E. P. O'Reilly. *Phys. Rev. Lett.*, 93(196402):4, 2004.

[27] F. Masia, G. Pettinari, A. Polimeni, M. Felici, A. Miriametro, M. Capizzi, A. Lindsay, S. B. Healy, E. P. O'Reilly, A. Cristofoli, G. Bais, M. Piccin, S. Rubini, F. Martelli, A. Franciosi, P. J. Klar, K. Volz, and W. Stolz. *Phys. Rev. B*, 73(073201):4, 2006.

[28] A. Patanè, J. Endicott, J. Ibáñez, P. N. Brunkov, L. Eaves, S. B. Healy, A. Lindsay, E. P. O'Reilly, and M. Hopkinson. *Phys. Rev. B*, 71(195307):8, 2005.

[29] R. Kudrawiec, G. Sek, J. Misiewicz, L. H. Li, and J. C. Harmand. *Solid State Commun.*, 2004.

[30] R. K. Hayden, D. K. Maude, L. Eaves, E. C. Valadares, M. Henini, F. W. Sheard, O. H. Hughes, J. C. Portal, and L. Cury. *Phys. Rev. Lett.*, 66(13): 1749–1752, 1991.

[31] J. Endicott, A. Patanè, J. Ibáñez, L. Eaves, M. Bissiri, M. Hopkinson, R. Airey, and G. Hill. *Phys. Rev. Lett.*, 91(12):126802, 2003.

[32] I. Vurgaftman and J. R. Meyer. *J. Appl. Phys.*, 94(6):3675–3696, 2003.

[33] I. Suemune, K. Uesugi, and W. Walukiewicz. *Appl. Phys. Lett.*, 77(19):3021–3023, 2000.

[34] R. Chtourou, F. Bousbih, S. Ben Bouzid, F. F. Charfi, J. C. Harmand, G. Ungaro, and L. Largeau. *Appl. Phys. Lett.*, 80(12):2075–2077, 2002.

[35] J. L. Merz, A. M. Mintairov, T. Kosel, and K. Sun. *IEE Proc.-Optoelectronics*, 151(5):346–351, 2004.

[36] X. Liu, M. E. Pistol, and L. Samuelson. *Phys. Rev. B*, 42(12):7504–7512, 1990.

[37] X. Liu, M. E. Pistol, and L. Samuelson. *Appl. Phys. Lett.*, 56(15):1451 –1453, 1990.

[38] Y. Zhang, A. Mascarenhas, J. F. Geisz, H. P. Xin, and C. W. Tu. *Phys. Rev. B*, 63(8):085205, 2001.

[39] P. R. C. Kent and A. Zunger. *Phys. Rev. Lett.*, 86(12), 2000.

[40] A. Patanè, A. Ignatov, D. Fowler, O. Makarovsky, and L. Eaves. *Phys. Rev. B*, 72(033312):4, 2005.

[41] P. Y. Yu and M. Cardona. *Fundamentals of Semiconductors*. Springer, Berlin, 2001. p. 230.

[42] Yu. R. Blyashko and L. N. Dusheva. Low-barrier GaAs diodes for high-frequency and mm-wave technics. *Proc. Acad. Eng. Sciences*, 7:49–55, 2004.

[43] F. Maiwald, F. Lewen, B. Vowinkel, W. Jabs, D. G. Pavel'ev, M. Winnewisser, and G. Winnewisser. *IEEE Microwave and Guided Wave Lett.*, 9(5):198–200, 1999.

[44] E. H. Armstrong. *Proc. I. R. E.*, 5:145–168, 1917.

[45] I. A. Glover, S. R. Pennock, and P. R. Shepherd. *Microwave devices, circuits and subsystems for communications engineering.* John Wiley & Sons, Ltd, 2005. For a review on Mixers see ch. 5, p. 311.

[46] M. Yu. Tretyakov and Yu. K. Kalynov. *Instrum. Exp. Tech.*, 49(5):661–668, 2006.

[47] S. H. Gold and G. S. Nusinovich. *Rev. Sci. Instrum.*, 68(11):3945–3974, 1997.

[48] Y. Carmel, J. Ivers, R. E. Kribel, and J. Nation. *Phys. Rev. Lett.*, 33(21): 1278–1282, 1974.

[49] J. P. Leite Neto and J. J. Barroso. *Braz. J. Phys.*, 34(4b), 2004.

[50] K. M. Yu, W. Walukiewicz, J. Wu, D. E. Mars, D. R. Chamberlin, M. A. Scarpulla, O. D. Dubon, and J. F. Geisz. *Nat. Mater.*, 1(185), 2002.

[51] D. Fowler, O. Makarovsky, A. Patanè, L. Eaves, L. Geelhaar, and H. Riechert. *Phys. Rev. B*, 69(153305):4, 2004.

[52] C. Skierbiszewski, P. Perlin, P. Wisniewski, T. Suski, W. Walukiewicz, W. Shan, J. W. Ager, E. E. Haller, J. F. Geisz, D. J. Friedman, J. M. Olson, and S. R. Kurtz. *Phys. Status Solidi B*, 216:135, 1999.

[53] R. Mouillet, L. A. de Vaulchier, E. Deleporte, Y. Guldner, L. Travers, and J.-C. Harmand. *Solid State Commun.*, 126:333, 2003.

[54] S. Fahy and E. P. O'Reilly. *Appl. Phys. Lett.*, 83(18):3731 –3733, 2003.

[55] S. Fahy, A. Lindsay, H. Ouerdane, and E. P. O'Reilly. *Phys. Rev. B*, 74 (035203):13, 2006.

[56] A. Patanè, G. Allison, L. Eaves, N. V. Kozlova, Q. D. Zhuang, A. Krier, M. Hopkinson, and G. Hill. *Appl. Phys. Lett.*, 93(25):252106, 2008.

[57] G. Allison, N. Mori, A. Patanè, J. Endicott, L. Eaves, D. K. Maude, and M. Hopkinson. *Phys. Rev. Lett.*, 96(236802):4, 2006.

[58] A. Higashisaka. *Jpn. J. Appl. Phys.*, 9:583, 1970.

[59] D. Patanè, A. Sherwood, L. Eaves, T. M. Fromhold, M. Henini, P. C. Main, and G. Hill. *Appl. Phys. Lett.*, 81:661, 2002.

[60] A. Neumann. *J. Appl. Phys.*, 90:1, 2001.

[61] F. Piazza, P. C. M. Christianen, and J. C. Mann. *Phys. Rev. B*, 55:15591, 1997.

[62] A. G. de Oliveira, G. M. Riberio, H. A. Albuquerque, M. V. B. Moreira, W. N. Rodrigues, J. C. Gonzàlez, and R. M. Rubinger. *Phys. Rev. B*, 74:035204, 2006.

[63] J. R. Barker, M. Mudares, B. R. Snell, P. S. S. Guimaraes, D. C. Taylor, L. Eaves, and G. Hill. *Appl. Phys. Lett.*, 47(4):387–389, 1985.

[64] C. Hamaguchi. *Basic Semiconductor Physics*. Springer Berlin, 2001. For a review on magnetophonon resonance see p. 285.

[65] L. Eaves, P. S. S. Guimaraes, J. C. Portal, T. P. Pearsall, and G. Hill. *Phys. Rev. Lett.*, 53(6):608–611, 1984.

[66] J. R. Barker. *J. Phys. C*, 5:1657, 1972.

[67] R. A. Stradling and R. A. Wood. *J. Phys. C*, 1:1711, 1968.

[68] M. P. Vaughan and B. K. Ridley. *Phys. Rev. B*, 75:195205, 2007.

[69] M. Reason, Y. Jin, H. A. McKay, N. Mangan, D. Mao, R. S. Goldman, X. Bai, and C. Kurdak. *J. Appl. Phys.*, 102:103710, 2007.

[70] B. I. Shklovskii and A. L. Efros. *Electronic Properties of Doped Semiconductors*, volume 45 of *Springer Series in Solid-State Sciences*. Springer-Verlag, Berlin, 1984. p. 155.

[71] T. O. Poehler. *Phys. Rev. B*, 4:1223, 1971.

[72] J. L. Robert, A. Raymond, L. Konczewicz, C. Bousquet, W. Zawadzki, F. Alexandre, I. M. Masson, J. P. Andre, and P. M. Frijlink. *Phys. Rev. B*, 33:5935, 1986.

[73] B. Jouault, A. Raymond, and W. Zawadzki. *Phys. Rev. B*, 65:245210, 2002.

[74] J. Wu, W. Walukiewicz, and E. E. Haller. *J. Appl. Phys.*, 89:789, 2001.

[75] D. Cabib, E. Fabri, and G. Fiorio. *Solid State Commun.*, 9:1517, 1971.

[76] T. Ando. *J. Phys. Soc. Jpn.*, 38(4):989–997, 1975.

[77] M. Betz, G. Goger, A. Leitenstorfer, K. Ortner, C. R. Becker, G. Bohm, and A. Laubereau. *Phys. Rev. B*, 60(16):R11265–R11268, 1999.

[78] A. Sibile, J. F. Palmier, A. Celeste, J. C. Portal, and F. Mollot. *Europhys. Lett.*, 13(279), 1990.

[79] E. H. Cannon, F. V. Kusmartsev, K. N. Alekseev, and D. K. Campbell. *Phys. Rev. Lett.*, 85(1302), 2000.

[80] M. Shur. *GaAs devices and circuits*. Plenum Press, New York, 1987.

[81] P. G. Savvidis, B. Kolasa, G. Lee, and S. J. Allen. *Phys. Rev. Lett.*, 92 (196802):4, 2004.

[82] N. Sekine and K. Hirakawa. *Phys. Rev. Lett.*, 94(057408):4, 2005.

[83] R. Köhler, A. Tredicucci, F. Beltram, H. E. Beere, E. H. Linfield, A. G. Davies, D. A. Ritchie, R. C. Iotti, and F. Rossi. *Nature*, 417:156–159, 2002.

[84] J. Lusakowski, W. Knap, N. Dyakonova, L. Varani, J. Mateos, T. Gonzalez, Y. Roelens, S. Bollaert, A. Cappy, and K. Karpierz. *J. Appl. Phys.*, 97 (064307):4, 2005.

[85] R. R. Bashirov, Z. S. Gribnikov, N. Z. Vagidov, and V. V. Mitin. *Appl. Phys. Lett.*, 77(23):3785–3787, 2000.

[86] T. Kampfrath, L. Perfetti, F. Schapper, C. Frischkorn, and M. Wolf. *Phys. Rev. Lett.*, 95(187403):4, 2005.

[87] D. Y. Lu, Y. Li, U. Ravaioli, and K. Schulten. *Phys. Rev. Lett.*, 95(246801): 4, 2005.

[88] J. R. Tucker and M. J. Feldman. *Rev. Mod. Phys.*, 57:1055, 1985.

[89] A. Patanè, N. Mori, D. Fowler, L. Eaves, M. Henini, D. K. Maude, C. Hamaguchi, and R. Airey. *Phys. Rev. Lett.*, 93(14):146801, 2004.

[90] A. A. Ignatov and A. P. Jauho. *J. Appl. Phys.*, 85(7):3643–3654, 1999.

[91] S. Winnerl, E. Schomburg, J. Grenzer, H. J. Regl, A. A. Ignatov, A. D. Semenov, K. F. Renk, D. G. Pavel'ev, Y. Koschurinov, B. Melzer, V. Ustinov, S. Ivanov, S. Schaposchnikov, and P. S. Kop'ev. *Phys. Rev. B*, 56(16):10303–10307, 1997.

[92] E. Schomburg, A. A. Ignatov, J. Grenzer, K. F. Renk, D. G. Pavel'ev, Yu. Koschurinov, B. Ja. Melzer, S. Ivanov, S. Schaposchnikov, and P. S. Kop'ev. *Appl. Phys. Lett.*, 68(8):1096, 1996.

[93] A. A. Ignatov, E. Schomburg, K. F. Renk, W. Schatz, J. F. Palmier, and F. Mollot. *Ann. Phys.*, 506(3):137–144, 1994.

[94] Yu. R. Blyashko and L. N. Dusheva. Schottky-barrier diode manufacture. *Patent No RU2197767-C1*, 2003.

[95] M. A. Lampert. *Phys. Rev.*, 103(6):1648, 1956.

[96] L. Esaki and R. Tsu. *IBM J. Res. Dev.*, 14:61, 1970.

[97] T. M. Fromhold, A. Patanè, S. Bujkiewicz, P. B. Wilkinson, D. Fowler, D. Sherwood, S. P. Stapleton, A. A. Krokhin, L. Eaves, M. Henini, N. S. Sankeshwar, and F. W. Sheard. *Nature*, 428:726, 2004.